University of Messina
Department of Mathematics and Computer Sciences,
Physics and Earth Science

PhD in Physics
Cycle XXXVII
SSD PHYS/01

Secondary beams at Jefferson Laboratory

Thesis by:
Antonino Fulci

Supervisor:
Prof. G. Mandaglio
Co-Supervisor:
Prof. M. Battaglieri
PhD Coordinator:
Prof. V. Crupi

Academic Year 2023/24

Abstract

This thesis explores the possibility of producing secondary beams at the Thomas Jefferson National Accelerator Facility (TJNAF). Their possible applications in future experiments are studied using advanced Monte Carlo simulations with state-of-the-art software. In Jefferson Lab's Hall-A, the interaction of the high-current $\mathcal{O}(100)$ µA, medium-energy $\mathcal{O}(11)$ GeV electron beam produced by the Continuous Electron Beams Accelerator Facility (CEBAF) with the Beam-Dump (BD) generates a substantial shower of standard model particles. This interaction creates a high-intensity secondary muon and neutrino beam and hypothetical Light Dark Matter (LDM) particles. Additionally, with the proposed Compact Photon Source (CPS), Hall-D could offer the possibility of producing an intense muon beam alongside a photon beam.

Acknowledgment

I want to express my deepest gratitude to those who have supported me throughout my academic journey.

First and foremost, I am profoundly grateful to my university tutor, Giuseppe Mandaglio, for his guidance throughout my bachelor's and master's degrees and for accepting me as a PhD student.

I extend my heartfelt thanks to my co-tutor, Marco Battaglieri, whose mentorship and direction have been crucial during my master's and PhD studies. His constant encouragement and wisdom have greatly influenced my academic and personal growth.

Special thanks go to Mariangela Bondì and Alessandro Pilloni for their invaluable assistance with administrative tasks, travel arrangements, and valuable suggestions during my PhD. Thanks also to Marco Spreafico and Stefano Grazzi for their support during my PhD, which significantly contributed to the completion of my research. I also want to thank Andrea Bersani for his studies on realistic magnets to be used in the CPS muon secondary beam missing momentum experiment.

I am profoundly grateful to Luca Tagliapietra and Lorenzo Zana for their assistance with FLUKA Monte Carlo simulations. I also thank the radiation group for allowing me to use their Hall-A FLUKA geometry, without which my thesis would not have been possible. I thank Pavel for letting me use his FLUKA CPS geometry and assisting in designing a possible muon missing momentum experiment. I also thank Pierfrancesco Butti for his help in developing the muon tracking system for the CPS muon secondary beam.

I am deeply thankful to Maurizio Ungaro and Raffaella de Vita for their guidance in using GEMC and their willingness to help me solve several simulation problems. They also helped me during my stay in the United States of America. I thank Patrick Achenbach for his support and availability, which greatly facilitated my research during my stay at Jefferson Lab.

I also thank Cristiano Fanelli for hosting me at William and Mary and allowing me to work on cutting-edge projects and James Giroux for his support during my stay there.

I would also like to thank the INFN Genova Group for their resources and technical support and the JLab IT team for their computational resources.

Table of Contents

List of Figures

List of Tables

List of Acronyms

BD	Beam-Dump 1–3, 5, 9, 11, 34–38, 40, 41, 43, 47, 49–55, 57, 58, 60, 61, 65–70, 73–77, 91
BDX	Beam Dump eXperiment 2, 11, 36–38, 47, 48, 55–57, 91, 92
BSM	Beyond Standard Model 2, 11
CEνNS	Coherent Elastic Neutrino-Nucleus Scattering 2, 10, 11, 15–17, 65, 68, 77–79, 92
CEBAF	Continuous Electron Beams Accelerator Facility 1, 3, 9, 11, 31, 33, 38, 42, 47, 58, 65, 91, 92
CERN	Conseil européen pour la Recherche nucléaire 11
CPS	Compact Photon Source 1, 3, 10, 11, 24, 29, 34, 43–45, 81–84, 86, 89, 92
DAR	decay-at-rest 11, 15, 16, 66, 67
DIF	decay-in-flight 11, 15, 66
EGSnrc	Electron Gamma Shower (National Research Council of Canada) 11, 22
EOT	Electrons On Target 11, 40, 41, 44, 51, 53, 57, 58, 60–62, 68, 73
FEL	Free-Electron Laser 11
Flair	FLUKA Advanced Interface 11, 24
FLUKA	FLUktuierende KAskade 1, 11, 23
FNAL	Fermi National Accelerator Labo- ratory 11, 68
GEANT4	GEometry ANd Tracking 4 1, 11, 23, 36
GlueX	Gluonic Excitation 11, 42
JAEA	Japan Atomic Energy Agency 11, 22
JLab	Jefferson Laboratory 1, 2, 11
KEK	Kō Energī Kasokuki Kenkyū Kikō 11, 22
LDM	Light Dark Matter 2, 3, 6, 9, 11, 17, 18, 36–38, 40, 41, 47, 57, 91
LERF	Low Energy Recirculator Facility 11
linac	Linear Accelerator 11, 31
LTBE	Linear Boltzmann Transport Equation 11, 20
MNCP	Monte Carlo N-Particle eXtended 11, 22
NNSI	Neutrino Non-Standard Interaction 11
PHITS	Particle and Heavy Ion Transport code System 11, 22
ppp	proton per pulse 9, 11
RIST	Information Science and Technology 11, 22
SBS	Super BigBite Spectrometer 11, 35
SLAC	Stanford Linear Accelerator Center 11, 14, 22
SM	Standard Model 5–7, 10, 11, 15, 17, 18, 38
SNS	Spallation Neutron Source 11, 15–17
TJNAF	Thomas Jefferson National Accelerator Facility 1, 3, 11, 31

Introduction

Motivation

This thesis aims to investigate and establish methods for utilizing the secondary beams produced by the high-intensity primary electron beam available at the Thomas Jefferson National Accelerator Facility (TJNAF) using the state-of-the-art Monte Carlo software FLUKA and GEANT4. Additionally, it seeks to demonstrate the significant advantages of these secondary beams, including their cost-effectiveness and the potential to conduct experiments in parallel to the primary electron beam's experimental programs.

The TJNAF, also referred to as Jefferson Laboratory (JLab), is a US Department of Energy National Laboratory in Newport News, Virginia. The design of the electron accelerator housed at JLab, also known as Continuous Electron Beams Accelerator Facility (CEBAF), offers a high-intensity continuous beam directed onto four targets found in the experimental halls, called Hall-A,-B, -C and -D.

Usually, high-intensity proton beams are used to generate secondary beams of particles such as neutrinos and muons. As it will be shown in this thesis, the high-current ($\sim$100 µA), medium-energy (1 GeV–10 GeV), continuous-wave electron beams present at JLab can also be used to generate secondary beams. Considering the possible beam energy upgrade, the studies in this thesis were repeated for a 22 GeV CEBAF beam.

At Jefferson Lab, it is possible to obtain secondary beams in two cases: using the beam-dump of Hall-A and the Compact Photon Source (CPS) being built for Hall-D, both with similar processes. In the first case, it will be shown that the main source of usable secondary beams consists of neutrinos and muons, and the second, it consists mainly of muons.

In the first case, the primary electron beam, after hitting the target, is dumped into an aluminum cylinder, also referred to as Beam-Dump (BD). If the primary beam's initial energy is higher than the pion production threshold, hadronic interaction and electromagnetic processes contribute to producing a sizable number of secondary particles that may re-interact or escape from the BD. To minimize the escaping radiation, the BD is surrounded by heavy shielding (e.g., a thick concrete vault). Nevertheless, a significant flux of neutrons, muons, and neutrinos propagate through the shielding, making intense secondary beams that may provide an opportunistic extension of investigations performed with the primary electromagnetic probe. According to recent theoretical studies, the interaction of an intense electron beam with the beam dump could also be a source of a LDM particle beam. LDM particles that are viable candidates to explain gravitational anomalies, extending the current set of elementary particles and interactions Beyond Standard Model (BSM).

In the second case, the electron beam is deflected by a magnet inside a radiator to produce photons. This interaction also produces muons through the same processes described in the first case.

The high intensity of the JLab electron beam allows for the probing of very rare processes. While this enables certain experiments, it also makes simulating these rare events computationally challenging using Monte Carlo codes. This thesis will also discuss these challenges and propose innovative solutions.

Outline of the thesis

In the first instance, the thesis will present the theory behind the production of secondary beams. The "classical approach" of using a proton beam will be discussed, highlighting its significance, applications, and differences from the "non-classical" approach of using electron beams. The theory on neutrino and Light Dark Matter (LDM) beams will be discussed briefly.

Chapter 2 will explore the simulation methods and tools used in particle physics. An overview of Monte Carlo methods for particle transport will be presented alongside the main software commonly used. The chapter will cover FLUKA in greater detail, discussing its main functionalities, biasing techniques, and user routines involved in the studies presented later in this thesis.

Chapter 3 will provide an overview of the Jefferson Lab (JLab) secondary beams. It will cover the secondary beams at JLab, focusing on the experimental Halls A and D detailing Hall-A's Beam-Dump (BD), the Beam Dump eXperiment (BDX), and the simulation frameworks used.

Chapter 4 will discuss the secondary muon and LDM beams at JLab's Hall-A. It will cover the production of secondary muon beams using 11 and 22 GeV electron beams, including the BDX passive shielding design. The secondary LDM beam and the discovery potential of the sBDX-MINI experiment will also be discussed.

Chapter 5 will focus on the secondary neutrino beam at JLab's Hall-A. It will discuss the production of secondary neutrino beams using 11 GeV and 22 GeV electron beams. The chapter will also cover the Coherent Elastic Neutrino-Nucleus Scattering (CEνNS) experiment at JLab, including beam-related neutron background estimation techniques and results, cosmic rays-related background, and physics sensitivity.

Finally, chapter 6 will explore the secondary muon beam at the KLF-CPS facility in JLab's Hall-D and discuss the feasibility of a possible missing momentum experiment.

Chapter 1

Physics with secondary beams

Secondary beams of particles such as pions, kaons, neutrinos, and muons are typically produced by colliding an intense primary beam, usually a proton one, with a target material, Figure 1.1. This thesis will instead explore the possibility of using an intense electron beam of $\mathcal{O}(11)$ GeV impinging on a Beam-Dump (BD) to produce the same kind of secondary particles. Using an electron beam instead of a proton one to produce secondary beams could offer new and different ways to probe the fundamental properties of matter and search for physics beyond the Standard Model (SM).

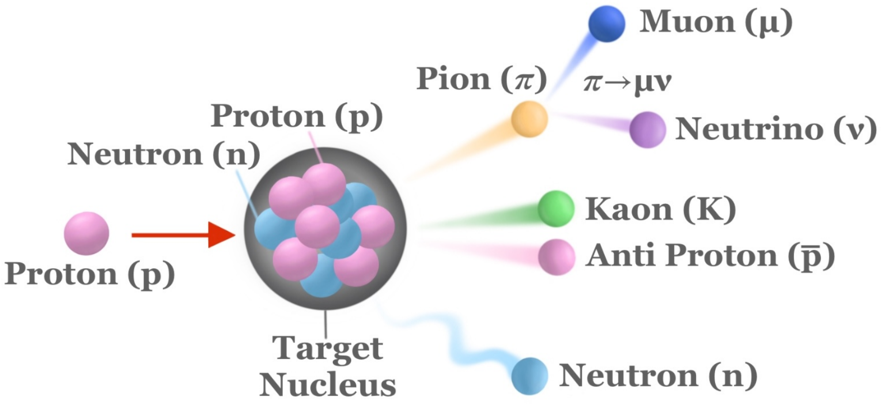

Figure 1.1: Summary schematic of a proton striking a target nucleus producing secondary pions, kaons, muons, neutrinos, antiprotons, and neutrons.

In particle physics, pion and kaon beams are mainly used to probe for strong nuclear force. Pion beams have a wide range of uses; they can be used to study in-medium modifications of strange hadrons in pion-nucleus reactions [1]; conduct charmed baryon spectroscopy [2]; produce hyperons to investigate non-perturbative aspects of the strong interaction [3]; explore baryon-meson coupling and time-like electromagnetic transition form factors [4]. Similar arguments hold for kaon beams that can be used to perform hyperon spectroscopy [5] and to study rare decays like $K_L \to \pi^0 \nu \bar{\nu}$ for new physics beyond SM that breaks the CP symmetry [6].

Muon and neutrino beams will be discussed in detail in sections section 1.1 and section 1.2. Briefly, muon beams, due to their unique properties, have found extensive applications in areas such as muon tomography [7] and material probing [8]. Muon beams are also planned for future particle accelerators and neutrino factories [9].

Neutrino beams, on the other hand, offer a unique window into the weak nuclear force and tests for the fundamental properties of neutrinos themselves [10]. Moreover, they are needed for studying phenomena such as neutrino oscillations and CP violation, which could provide insights into the matter-antimatter asymmetry observed in the universe [11, 12].

Finally, in section 1.3, the possibility of a Light Dark Matter (LDM) beam will be discussed. The LDM existence would bring theoretical predictions in agreement with observations [13, 14] such as reconciling the persistent $\sim 4\sigma$ discrepancy in the anomalous magnetic moment of the muon [15, 16].

1.1 Muon beams

Generally, the easiest method to investigate an object is by observing it or, in scientific terms, by analyzing the interaction between photons and the object in question. The level of detail that can be seen is inversely proportional to the energy of the photons used. A logical progression of this method is to explore the inner structure of atoms, nuclei, and nucleons by scattering leptons off them. Usually, electrons are used as a probe because they are easy to create and accelerate to the desired energy. However, these benefits diminish at higher energy as the electrons radiate a substantial portion of their energy when deflected in a magnetic field. Muons provide an alternative source of leptons to use as a probe.

The muon is an elementary particle similar to the electron but with a larger mass, approximately 105.66 MeV/c^2, almost 207 times that of an electron. Because of this, muons travel through matter at slower speeds than electrons. As a result, they penetrate much deeper into matter because they lose energy due to the radiation at a significantly slower rate. The result is that their effective radiation length is a factor m_μ^2/m_e^2 longer compared to electrons. Because of this, when using muons as a probe, it is possible to use thicker targets that can give muon experiments a further advantage in luminosity. Moreover, this property of the muon also implies that corrections for higher-order QED effects, such as two-photon exchange, are correspondingly reduced [17].

Muon beams hold significant interest in physics due to their unique properties, suggesting their potential use in high-energy physics research, industrial applications, and medical fields. For instance, muon beams can be used in muonic X-rays and muon radiography [18]. Moreover, compact muon accelerators are sought after for medical and material detection applications [19, 20].

High-intensity muon beams have applications in many research fields spanning from fundamental particle physics [21] to materials science [22] or inspection and imaging [23]. In particular, using high-intensity GeV-energy muon beams could lead to the discovery of new light particles not predicted by the SM.

Most of the current [24–29] and planned [30–32] facilities produce muons as secondary particles by decay of pions/kaons created by the interaction of an intense proton beam, typically of several MW power, with a heavy material target. However, muon beams can be produced using a high-intensity multi-GeV electron beam hitting a thick target.

1.1.1 Muon production from a primary proton beam

Muon beams are usually created in proton accelerators through several steps. Initially, a high-power proton beam in the multi-GeV energy range is directed toward a fixed target. This interaction produces a secondary beam of charged pions, kaons, and a small fraction of muons. Charged pions and neutral kaons decay over several meters until the beam composition is approximately 5% muons. These are schematically shown in Figure 1.2.

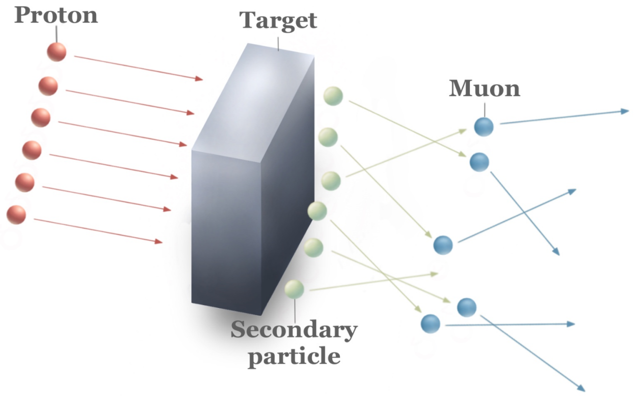

Figure 1.2: Schematic drawing of a proton beam impinging on a target produces secondary particles that decay into muons.

In this case, most muons came from the decay of charged pions, whose primary decay mode is a leptonic decay, into a muon and a muonic neutrino, governed by the weak interaction:

$$\pi^{\pm} \rightarrow \mu^{\pm}\nu_{\mu}(\bar{\nu}_{\mu})$$

A consequence of this decay is that the muons are fully polarized in the center-of-mass system because the pion has a zero spin and the muon neutrino possesses a specific helicity ($h = -1$ for $\bar{\nu}_\mu$ and $h = +1$ for ν_μ). A Feynman diagram of this process is shown in Figure 1.3.

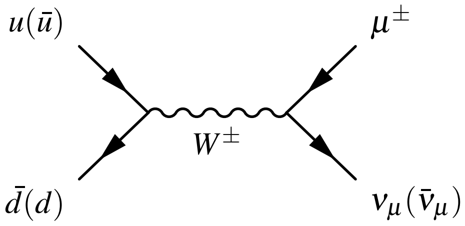

Figure 1.3: Feynman diagram of charged pion weak decay into muons.

Another considerably significant source of muons comes from the weak decay of charged kaons. Even in this case, the muons are fully polarized in the center of mass system. A Feynman diagram of this process is shown in Figure 1.4.

$$K^\pm \to \mu^\pm \nu_\mu(\bar{\nu}_\mu)$$

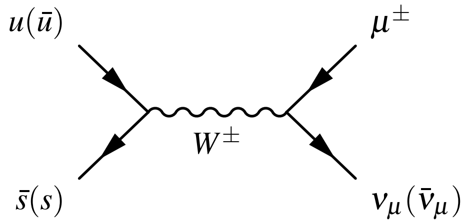

Figure 1.4: Feynman diagrams of charged kaon decay into muons.

After the decay of pions and kaons, several meters of material with a relatively low atomic number are used to absorb the background particles. The choice of this material is usually made so that the muons do not suffer much from the effect of multiple scattering. Subsequently, the muons are collected by components of the electromagnetic beamline, and then the beam is delivered to the experimental area.

It's important to note that the capture of the muon must occur within a timescale compatible with the muon's lifetime at rest, which is approximately 2.2 microseconds. Moreover, without re-acceleration, the energy and intensity of the muon beam are limited by the energy and intensity of the initial proton beam and the efficiency with which the muons are collected.

In a standard hadron beam, basic mechanical collimators can easily adjust the beam's shape-to-phase space ratio. However, for muon beams, magnetic deflection is also necessary for the undesired muons. This is because merely introducing material only increases the scattering and does not halt the muons. If magnetic collimation is not provided, the muon beam at the experiment is distinguished by a halo-to-beam ratio of approximately 1:1. The term "halo" is typically used to describe those muons that pass through the apparatus at a distance greater than 2-3 cm from the beam axis, but still within its sensitive area of about 4×4 m^2.

The CERN M2 beam line

One of the most potent secondary muon beams produced from a proton beam is found at the CERN M2 beam line [33]. This beamline has three main operation modes with different intensities expressed in proton per pulse (ppp): a high-intensity muon beam $\mathcal{O}(10^8)[ppp/4.8s]$ up to 200 GeV (higher momenta are possible up to 280 GeV, but the flux drops very rapidly with beam momentum), a high-intensity secondary hadron beam $\mathcal{O}(1-4\times 10^8)[ppp/4.8s]$ for momenta up to 280 GeV with radiation protection constraints, low-intensity (and low-quality) $\mathcal{O}(10^4)[ppp/4.8s]$ electron mainly used for calibration purposes.

These beams are produced following the principles described in the previous section: a high-intensity, high-energy proton beam strikes a target; then the pions and kaons produced are left to decay over a distance of approximately 600 m, creating a tertiary muon beam; then an absorber is placed to block secondary particles except for muons; a set of magnetic collimators (commonly called "scrapers") and magnetized iron blocks are used to protect the experiment against unwanted halo particles outside the main beam.

The possible experiments using the M2 beamline include MUonE, NA64μ, and COMPASS++/AMBER. MUonE aims to measure the hadronic contribution to the vacuum polarization in the context of the $(g_\mu - 2)$ anomaly [34]. NA64μ is a muon beam program that searches for LDM [35]. Lastly, COMPASS++/AMBER proposes to measure the proton charge radius with muon-proton elastic scattering, the proton-induced antiproton production cross sections for dark matter searches, and Drell-Yan and J/ψ production [36, 37].

The Muon Campus at FermiLab and the M3 Experiment

The Muon Campus at Fermilab [38, 39] can support cutting-edge intensity frontier experiments using muon beams. Following the conclusion of the collider program in 2011, the anti-proton source from the Tevatron era was transformed into the present-day Muon Campus.

The muon production at the FermiLab Muon Campus begins with short batches of 8 GeV protons, an RF system splits each batch into four smaller bunches, each containing 10^{12} protons. These bunches are sent individually to a target station, which collects 3.1 GeV/c positive secondary particles. Pions and their daughter muons are transported through a 280-meter channel to the antiproton debuncher ring. After several revolutions, they are directed into a final beam line that leads to the muon storage ring used in the Muon g-2 Experiment [40]. This system can deliver 3.2×10^7 muons per second.

The M^3 experiment is a proposed fixed-target, missing-momentum muon-beam experiment at Fermilab [41]. It aims to utilize a 15 GeV muon beam with a thick target (approximately 50 radiation lengths) and a downstream detector to veto SM backgrounds to search for dark matter. The detector design is illustrated in Figure 1.5.

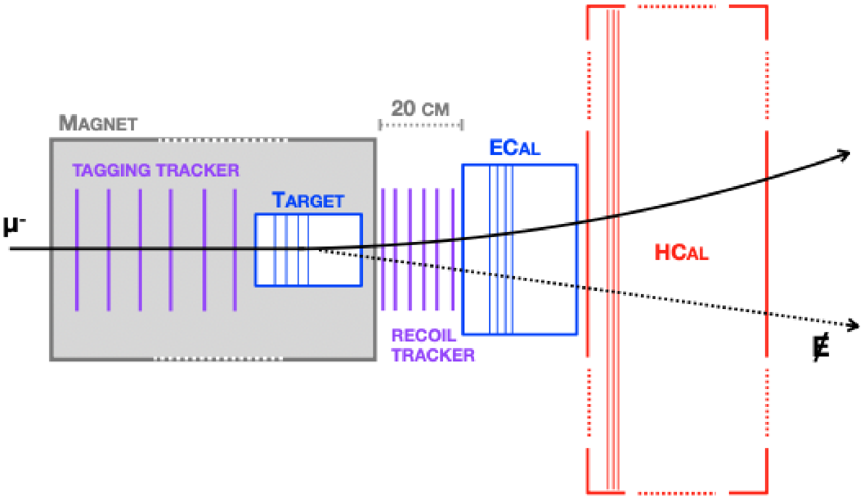

Figure 1.5: The incoming muon beam traverses a tagging tracker within the magnetic field region before reaching the target. Outgoing muons are detected by a recoil tracker, with the magnet's fringe field enabling momentum measurement. Electromagnetic and hadronic calorimeters are used to veto photons and hadrons produced during hard interactions in the target, which could otherwise cause significant muon energy loss.

The experiment will use the missing momentum technique to investigate the production of new, invisibly decaying muon-philic particles through dark bremsstrahlung in processes described by the reaction $\mu + \mathrm{N} \rightarrow \mu + \mathrm{N} + S$, showed in Figure 1.6. This involves an incident muon beam interacting with a fixed nuclear target. The particles of interest (S or V) are emitted from the muon as either initial- or final-state radiation during its interaction with the nucleus. These particles are assumed to promptly decay into dark matter or neutrinos, resulting in missing energy and momentum. Additional theoretical background on the model used is given in section 1.3.

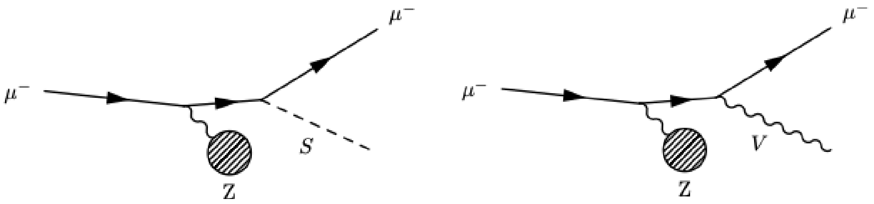

Figure 1.6: Dark bremsstrahlung signal process for simplified models with invisibly decaying scalar (left) and vector (right) forces that couple predominantly to muons. In both cases, a relativistic muon beam is incident on a fixed target and scatters coherently off a nucleus to produce the new particle as initial- or final-state radiation.

To implement this technique, it is crucial to identify and measure the momentum of individual muons. The experimental signature is characterized by an outgoing muon that emerges from the target with a significant loss of momentum compared to the incident muon, without any additional visible energy being deposited in the target material or in the downstream electromagnetic or hadronic calorimeters (ECAL/HCAL).

The experiment will proceed in two distinct phases. Phase 1, targeting 10^{10} muons, aims to explore the remaining parameter space where light invisibly-decaying particles could address the $(g-2)_\mu$ anomaly. Phase 2, with approximately $\sim 10^{13}$ muons, will investigate a significant portion of the predictive parameter space where sub-GeV dark matter achieves freeze-out through muon-philic forces, including gauged $U(1)_{L_\mu - L_\tau}$.

1.1.2 Muon production from a primary electron beam

Muon beams can also be created when an electron beam hits a thick target that spans several radiation lengths. In this scenario, muons are formed through two distinct processes. The first process involves the decay of photoproduced pions (or kaons) in muons. In the second process, that happens only if the electron energy is high enough, muons are directly photoproduced. In both processes, an electron radiates in the field of a nucleus. Then, the secondary particles are photo-produced at another nucleus in the target by the bremsstrahlung. The direct electroproduction reaction $e^-N \rightarrow e^-N\mu^-\mu^+$ produces instead minimal amount of muons [42]. These processes are shown in Figure 1.7.

Because electrons emit energetic photons when they convert to form $\mu^+\mu^-$ pairs, the muons produced have a high momentum. As a result, muons do not scatter significantly after they are created. Also, because muon photoproduction can occur at any point on the target, the yield from an electron beam is approximately 15 times greater than that from pion/kaon, which requires several meters to decay. Radiated muons strongly peak in the forward direction, with energy comparable to the primary beam energy. Instead,

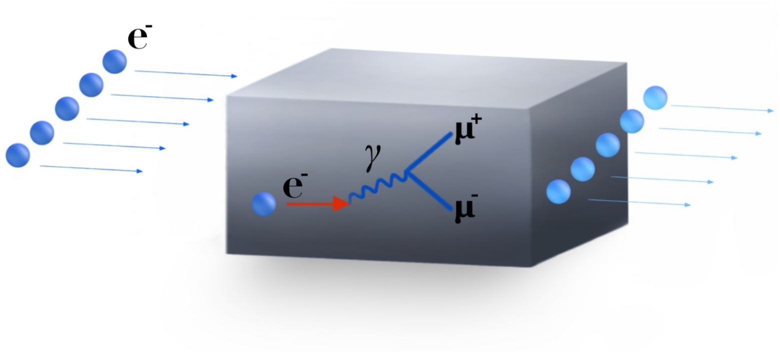

Figure 1.7: Schematic drawing of an electron beam impinging on a target producing secondary muons from electron-radiated photons.

muons produced via decay in flight of photo-produced pions and kaons show a lower energy spectrum.

Following the mathematical description given in [43], the pair production of muons can be described by the Bethe-Heitler mechanism, Figure 1.8.

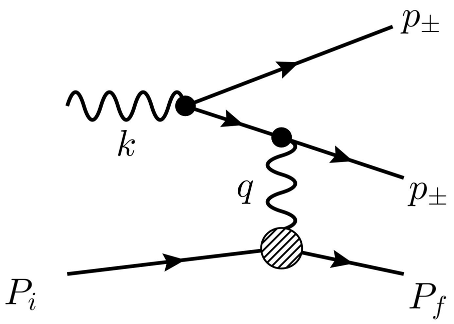

Figure 1.8: Feynman diagram for the photoproduction of a lepton pair.

The cross-section for $\gamma + Z \to l^+ l^-$ from the mechanism shown in Figure 1.8 can be written as:

$$\mathrm{d}\sigma = e^6 \frac{m_i}{4(k \cdot p_i)} \frac{\mathrm{d}^3 p}{E} \frac{\mathrm{d}^3 p_+}{E_+} \frac{1}{(2\pi)^5} \frac{1}{q^4} \left(L^{\mu\gamma} W_{\mu\nu}\right) \tag{1.1}$$

Where:

- k is the four-momentum of the incident photon and also the energy of the photon in the laboratory system
- p is the four-momentum of l^- in the laboratory system
- E is the energy of l^- in the laboratory system

- p_+ is the four-momentum of l^+ and E_+ is its energy
- m is the mass of l^+ or l^-
- p_i and m_i are the four-momentum and the mass, respectively, of the initial target system, and p_f and m_f are corresponding quantities for the final state of the target
- $q \equiv k - p - p_+ = p_f - p_i$ is the four-momentum transfer to the target system
- $W_{\mu\nu}$ is a tensor that defines the structure functions of the electron scattering
- $L^{\mu\gamma}$ is a tensor that defines the photon polarization

Equation 1.1 provides an exact representation up to the order of α^3 for pair production. However, its complexity can be overwhelming for many practical uses. Given that electrons and muons are frequently encountered in laboratory settings, it is more desirable to have formulas that can be used to calculate the required quantities quickly. First, it is possible to neglect the production due to virtual photons, as this is negligible in targets with a thickness greater than 1/25 of a radiation length (see [43]). Then the total number of events per incident electron on a target of T radiation lengths caused by the real photon can be demonstrated to be (see [43]):

$$Y = \frac{NX_0}{A}\int_{k_{\text{min}}}^{E_0} \sigma(k) \left\{ \frac{(1-e^{fT})}{f} - \frac{9}{7}\left(1-\exp[-\frac{7}{9}T]\right) \right\} \Big/ \left(\frac{7}{9}-f\right) \frac{\mathrm{d}k}{k} \tag{1.2}$$

where $\sigma(k)$ represent some photoproduction cross section and:

$$f = -\frac{4}{3}\ln(1-k/E_0)$$

Where E_0 is the energy of the incident electron. In the limits $T \to 0$ and $T \to \infty$, respectively:

$$Y \xrightarrow[T\to 0]{} \frac{NX_0}{A}\frac{T^2}{2}\int_{k_{\text{min}}}^{E_0} \sigma(k)\frac{\mathrm{d}k}{k} \tag{1.3}$$

and

$$Y \xrightarrow[T\to \infty]{} \frac{NX_0}{A}\int_{k_{\text{min}}}^{E_0} \sigma(k)\frac{9}{7f}\frac{\mathrm{d}k}{k} \tag{1.4}$$

The yield of secondary particles by an electron is proportional to T^2 when T is small and becomes independent of T as T becomes infinity.

The SLAC muon beam

A muon for high energy muon scattering studies utilizing the concepts explained in the previous section has been constructed at Stanford University, commonly known as Stanford Linear Accelerator Center (SLAC) [42]. Here, an electron beam hits a water-cooled copper target, producing secondary particles like pions and kaons. Pions travel through a 5.5-meter-long beryllium pion filter behind the target that is able to reduce the ratio π/μ to 3×10^{-6}.

Before striking the filter, muons have a spatial distribution in the transverse plane to the beam-axis similar to that of the incident electron beam, in the order of 5 x 5 mm^2. However, multiple coulomb scattering of muons in the pion filter causes them to appear to originate from a source with a diameter of about 2.5 cm near the filter's entrance. The calculated beam yield, using a 100 kW of 17 GeV electrons, is $1.0 \times 10^5 \mu/$ sec at 10 GeV/c in a momentum band of $\pm\%$. With its experimental setup, the SLAC muon beam is contained for 90% within an area of 5 cm × 10 cm, and 99% within an area of 10 cm × 10 cm.

Because of the great intensity of the beam, the SLAC production target is built to dissipate vast amounts of power. A schematic of the target is shown in Figure 1.9. The target has a thickness of 11.6 radiation lengths. It is able to absorb around 70% of the power in the electron beam and to disperse the cascade such that its diameter as it leaves the target is approximately 3 cm. The beam strength per unit area is then reduced to a size that can be handled by the beryllium filter that follows.

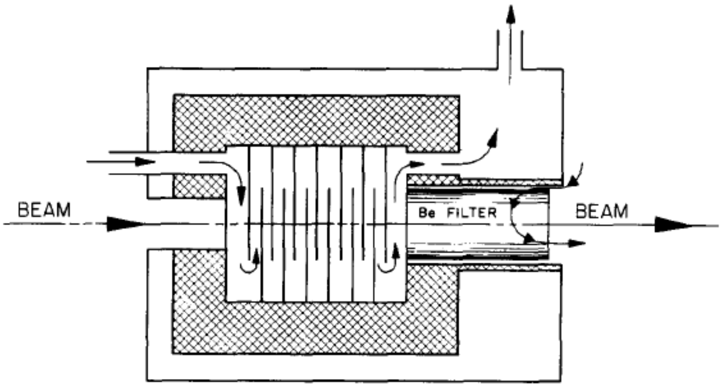

Figure 1.9: Schematic diagram of the water-cooled muon production target at SLAC.

1.2 Neutrino beams

The neutrino is a particle that was postulated by Wolfgang Pauli in 1930 to explain how beta decay could conserve energy, momentum, and angular momentum [44]. Pauli hypothesized that an undetected particle was emitted from the nucleus together with the electron in the process. The first direct detection of the neutrino came in 1956 with the Cowan–Reines neutrino experiment [45].

Neutrinos are neutral fermions that interact only through weak interaction and gravity. It has a non-null mass and comes in three flavors associated with the correspondingly charged lepton: ν_e, ν_μ, ν_τ. Neutrinos are created by various radioactive decays, such as beta decay of atomic nuclei or hadrons, natural nuclear reactions such as those that take place in the core of a star, artificial nuclear reactions in nuclear reactors, etc.

Fission reactors and proton accelerators are currently the primary sources of producing neutrino beams [46, 47]. The reactors produce electron-type antineutrinos from fission fragment beta decay and are widely used in low energy (~MeV) experiments. In accelerators, high-energy protons (or electrons) hit a target to generate short-lived hadrons (mainly $\pi^\pm$ and $K^\pm$) that successively either decay-in-flight (DIF) or decay-at-rest (DAR) into neutrinos. The neutrino production using a primary electron beam follows similar principles. Pions and kaons are produced, and then they either DIF or DAR.

DAR neutrinos show an isotropic spatial distribution with an energy spectrum depending on the decay:

- $\pi^+ \to \mu^+ + \nu_\mu$, $\mathrm{E}_\nu \sim 29.8$ MeV, almost monochromatic;
- $\mu^+ \to \bar{\nu}_\mu + \nu_e + e^+$, E_ν in the range 0 - 52.8 MeV;
- $K^+ \to \mu^+ + \nu_\mu$, $\mathrm{E}_\nu \sim 236$ MeV, almost monochromatic.

In Figure 1.10, a scheme summarizing the processes of neutrino production from an electron beam hitting a thick aluminum target is shown.
These DAR neutrinos are suitable for studying Coherent Elastic Neutrino-Nucleus Scattering (CEνNS). This process, predicted a long time ago, has been only recently observed [48] and is a leading candidate to study non-standard (BSM) neutrino interactions [49].

Other phenomena that can be studied using neutrino beams include neutrino oscillations, i.e., the process in which a neutrino changes its initial lepton number as it propagates in space; test of SM's like Weinberg angle θ_W; physics beyond the SM, like investigation of neutrinoless double beta decay, that would prove that neutrinos are Majorana particles.

1.2.1 Oak Ridge neutrino beam

The Spallation Neutron Source (SNS), located at Oak Ridge National Laboratory in Tennessee, USA, is the world's most intense pulsed neutron source. It serves both scientific research and industrial development. SNS currently runs at 1 GeV proton energy and 1.4 MW beam power, and after the next round of upgrades (2024), it will operate at 1.3 GeV proton energy and 2 MW beam power.

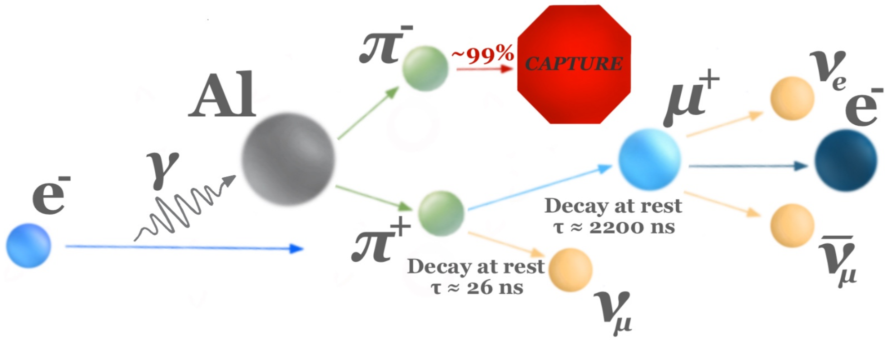

Figure 1.10: Schematic diagram of neutrino production from an electron beam hitting an aluminum target.

In addition to the neutron production, SNS is also capable of generating an intense, high-quality source of neutrinos from pion DAR [50]. These neutrinos are valuable for studying neutrino properties, neutrino-nucleus interactions, and nuclear properties.

Neutrino production from pions begins with the acceleration of protons to high energies, ranging from hundreds of MeV to the GeV scale. These high-energy protons are then directed to collide with a target, producing a large number of secondary hadrons. Protons with momentum exceeding approximately 300 MeV generate significant pions, which decay to produce neutrinos. The dominant neutrino production pion DAR is from the weak-interaction decay, $\pi^+ \to \nu_\mu + \mu^+$, followed by the decay at rest of the muon, $\mu^+ \to e^+ + \nu_e + \bar{\nu}_\mu$.

The neutrino beam experiments run in the so-called "Neutrino Alley" in the facility's basement. This area has about 70 meters of water-equivalent line-of-sight shielding to the SNS target and about 10 meters of water-equivalent overburden, sufficient to eliminate the hadronic component of cosmic rays.

The SNS neutrino source enabled the measurement of the CEνNS process.

CEνNS experiment at Oak Ridge

Coherent Elastic Neutrino-Nucleus Scattering (CEνNS) is a weak neutral-current (NC) process in which a low-energy neutrino elastically scatters from a target nucleus. [51]. The coherence condition, in which the neutrino scatters off all nucleons of the nucleus in phase with each other, is satisfied when the neutrino energy is in the tens of MeV range, and its momentum transfer to the recoiling nucleus is small (sub-keV to tens-of-keV range). This process provides a sensitive test of SM and beyond-SM processes.

The COHERENT collaboration was able to measure the CEνNS process in a liquid argon detector at the Oak Ridge National Laboratory SNS. The experiment used a 1 GeV proton beam to produce many pions that subsequently decay into neutrinos that travel for approximately 28 m, ending in the CENNS-10 detector [52] carefully designed for this experiment. The experiment opted for different techniques to deal with the background noise. Electron recoils were suppressed by two orders using pulse-shape discrimination, while neutrons and photons were shielded using a lead shield built around the target.

In total, the experiment collected data from $\sim 14 \times 10^{22}$ proton-on-target using the CENNS-10 detector and was able to measure the CEνNS process on argon through two independent analyses. Moreover, this measurement verified the expected neutron-number dependence of the cross-section and improved constraints on non-standard neutrino interactions. The full details of the experiment can be found in [50].

1.3 Light Dark Matter Beam

Despite several years of research, the particle nature of dark matter remains one of the most significant quests in fundamental science (for a review see [53]). Huge efforts have been spent in the last years into its identification, focusing on the search for Weakly Interacting Massive Particle candidates (WIMPs) with masses in the range 1 GeV–10 TeV. The lack of experimental evidences has motivated the interest toward sub-GeV LDM where direct detection has a limited sensitivity [54–57].

To achieve the correct abundance inferred from astrophysical constraints, the interaction between LDM and SM states has to be mediated by a new, light force carrier neutral under the SM gauge group. The LDM existence would also bring theoretical predictions in agreement with observations [13, 14] such as reconciling the persistent $\sim 4\sigma$ discrepancy in the anomalous magnetic moment of the muon [15, 16].

The theoretical options for including new interactions and particles in the SM are limited. A minimal list includes the renormalizable vector portals mediated by a dark vector boson, scalar portals mediated by a new scalar mixing with the Higgs boson, and neutrino portal operators mediated by a heavy neutral lepton. Vector and scalar portal are mainly motivated for Dark Matter with mass in the MeV-GeV range.

A significant experimental activity has been performed to verify or falsify the different hypotheses. Data collected in previous experiments, optimized for different physics scopes, were re-analyzed within the above-mentioned theoretical frameworks, which provided exclusion limits in the parameter space of the theories. New experiments, specifically designed to investigate the different options, already collected data or are expected to run in the near future. A comprehensive discussion about the possible LDM theoretical scenarios, the current experimental efforts, and a survey on the future proposals to detect LDM can be found in [58] for a comprehensive discussion about the possible LDM theoretical scenarios, the current experimental efforts, and a survey on the future proposals to detect LDM.

The discrepancy between the measured value of the muon's anomalous magnetic moment $\alpha_\mu \equiv \frac{1}{2}(g-2)_\mu$ and its SM prediction remain unexplained and amounts to [59]:

$$\Delta\alpha_\mu \equiv \alpha_\mu - \alpha_\mu(\text{SM}) = (28.8 \pm 8.0) \times 10^{-10} \tag{1.5}$$

This "anomaly" has strongly motivated light hidden particle searches, opening a window to new physics beyond the SM. The work presented in this thesis will focus on the minimal model that could explain the $(g-2)_\mu$ anomaly. A detailed theoretical model description is reported in [60, 61] and references therein.

In this model, the primary process responsible for the emission of the scalar S is a muon impinging on a fixed target in the so-called "radiative" production μ + N→μ + N + S. The incident muon interacts with a target nucleus, N, by exchanging a photon, γ, and radiates the S. The Feynman diagrams of this process are reported in Figure 1.6.

The energy distribution of the emitted scalar follows from the differential cross section integrated over all the emission angles [61]. In the case of a light scalar ($m_S \ll m_\mu$), the scalar to muon energy ratio $x = E_S/E_\mu$ distribution is concentrated in the low-x region, with a maximum value at $x_{\max} \simeq 1.4 m_S/m_\mu$. For a heavy scalar, the outgoing S takes a more significant portion of the muon energy, and the corresponding x distribution is peaked close to $x_{\text{peak}} \simeq 1 - m_S/E_\mu$.

Under the simplified dark scalar model used in this discussion ([61]), for the mass range $m_S < 2m_\mu$, the S particles propagate straight until decaying into two photons with a decay width, $\Gamma_{\gamma\gamma}$, which depends on the μ-S coupling constant, g_μ, and the ratio of muon to S masses, m_μ/m_S [60]:

$$\Gamma_{\gamma\gamma} = \frac{\alpha^2 m_S^3}{128\pi^3} \left| \frac{g_\mu}{m_\mu} \frac{4m_\mu^2}{m_S^2} \left[1 + \left(1 - \frac{4m_\mu^2}{m_S^2}\right) \arcsin^2 \left(\frac{4m_\mu^2}{m_S^2}\right)^{-1/2} \right] \right|^2 \tag{1.6}$$

A detector placed behind the production point of the scalar S measures the photons. However, a sizable amount of shielding material must be placed between the production point and the detector to exclude all other particles produced by the primary beam.
Different experimental techniques can be used to search for muon-coupling light dark scalars. Among them, medium-energy electron beam dump experiments, providing an intense source of secondary muons, cover a broad area in the g_μ vs. m_S parameter space, as shown in [61].

Chapter 2

Simulation Methods and Tools

This chapter is meant to introduce Monte Carlo methods used in particle physics, briefly overviewing the capabilities of commonly used software. This chapter then dwells in a more in-depth look at FLUKA in section 2.3, the primary software used for the studies presented in chapter 4, chapter 5, chapter 5, and section 6.1. Here, FLUKA will be described in greater detail, and the different biasing techniques used to increase statistics of rare events are explained in subsection 2.3.3. Finally, in subsection 2.3.4, this chapter details the problems correlated with performing simulations of high luminosity energy beams and how these can be solved with more sophisticated methods and techniques.

2.1 Monte Carlo methods for particle transport

The Monte Carlo method is a statistical approach that allows the simulation of mathematical or physical experiments on a computer. The underlying concept is to use randomness to solve problems that might be deterministic in principle. In mathematics, it can be used to calculate functions and integrals, while in physics and engineering, it can model complex problems that consist of random processes, each with a known or assumed probability density function. Like any statistical process, the Monte Carlo method necessitates the repetition of many trials to reduce aleatoric (stochastic) uncertainty, which arises from the inherent randomness in the sampling process. This type of uncertainty decreases as more trials are conducted, leading to more stable and reliable estimates. A more detailed mathematical description can be found in [62].

Usually, the first reference to the Monte Carlo method is that of Georges-Louis Leclerc, Comte de Buffon, who proposed a Monte Carlo-like method to evaluate the probability of tossing a needle onto a ruled sheet [63]. However, the actual development of the Monte Carlo method can be traced back to WWII, during the Manhattan Project. At that time, there was significant urgency in understanding nuclear fission. At around the same time, the first computer, ENIAC, was being built to perform calculations that were usually done by hand. Quickly, John von Neumann became interested in using ENIAC to test thermonuclear reactions. This opened the way for Stanislaw Ulam to use the computer for statistical sampling, the base on which Monte Carlo techniques are built. It quickly became clear that this method was more flexible and efficient for solving complex problems than differential equations despite requiring significant computational power. Over the years, this technique has been refined and expanded, and among its numerous applications, it is used to simulate the propagation of radiation through matter.

Radiative transfer (also called radiation transport) is the physical phenomenon of energy transfer in the form of electromagnetic radiation. This process is fundamental to understanding how radiation, and more generally particles, propagate through different media. This problem involves modeling the behavior and interactions of particles as they move through and interact with matter. These interactions can include complex processes such as scattering, absorption, and emission. The ultimate goal of solving this problem is to measure or estimate various quantities, such as the energy-angle particle spectra, the deposited energy in a detector or region, the material damage, the biological effects of a given source, and the resulting radioactive inventories. This information is crucial for nuclear reactor physics, medical physics, astrophysics, and radiation protection applications.

An accurate description of the transport of radiation through matter is given by the Linear Boltzmann Transport Equation (LTBE) (Equation 2.1) [64], this equation determines the radiation field at another position $\mathbf{r}$ at a later time t by looking at the particle balance in a small volume V (with surface S).

$$\begin{aligned}\int_V \mathrm{d}\mathbf{r}\frac{\partial n_i(\mathbf{r},E,\Omega,t)}{\partial t} =& -\oint \mathrm{d}A\mathbf{j}(\mathbf{r},E,\Omega,t)\cdot\hat{\mathbf{a}} \\ & -N\int_V \mathrm{d}r n_i(\mathbf{r},E,\Omega,t)v(E)\sigma(E) \\ & +N\int_V \mathrm{d}r\int \mathrm{d}E'\int \mathrm{d}\Omega n_i(\mathbf{r},E',\Omega' t)v(E')\frac{\mathrm{d}\sigma}{\mathrm{d}\Omega''\mathrm{d}W''} \\ & +N\int_V \mathrm{d}r\int \mathrm{d}E'\sum_j n_j(\mathbf{r},E',\Omega' t)v(E')\frac{\mathrm{d}\sigma_{\mathrm{sec},i}}{\mathrm{d}\Omega''\mathrm{d}W''} \\ & +\int_V \mathrm{d}\mathbf{r}Q_{\mathrm{source}}(\mathbf{r},E,\Omega,t)\end{aligned} \tag{2.1}$$

Where i, E, Ω are, respectively, the number of particle species, the energy, and the direction of that particular species. Ω'' represent the direction such that the scattering angle Ω' bring it to Ω.

The end goal should be to solve this equation using an arbitrary source density $n_0(\mathbf{r},E,\Omega,t)$ in an arbitrary geometry and using realistic interaction cross sections. However, it is practically impossible to solve this equation analytically, except for a few simple cases. So, other techniques must be used, the most practical, general, and efficient one, that can be used to treat arbitrary radiation fields and geometries, is the Monte Carlo one.

However, it's crucial to acknowledge the assumptions and constraints inherent in this approach. Specifically, this method presumes that materials are static, homogeneous, and isotropic. Additionally, it treats radiation transport as a Markovian process, meaning the future state of a particle is determined solely by its current state, independent of its past. It also assumes that the material's properties remain unaffected by previous interactions. Finally, particles are considered to follow specific trajectories and interact with individual atoms, electrons, or nuclei.

2.1.1 Uncertainties using Monte Carlo methods in particle physics

Like any other scientific technique, Monte Carlo methods are not devoid of uncertainties, and understanding them is crucial for interpreting the results accurately. Monte Carlo simulations are typically subject to two categories of errors: statistical and systematic.

The first type depends on the number of primaries simulated, with more particles simulated associated with a smaller error on the measurement and tending to a Gaussian centered around the true expectation value, with a standard deviation that goes like $1/\sqrt{(N)}$. This is the consequence of the Central Limit Theorem, which states that the sum of a large number of independent random variables has a distribution that is approximately Gaussian.

Systematic uncertainties constitute the second category of uncertainties inherent in Monte Carlo simulations. These uncertainties originate from different factors. For instance, inaccuracies in the used physics models and transport algorithms can contribute to systematic errors, as can discrepancies in cross-section data. They also can arise due to incomplete knowledge of materials, such as the amount of water in the soil or concrete modeled into the geometry or additional materials like cables and supports. Other factors can include excessive simplification of the geometry, bugs, and mistakes in the code.

2.2 Monte Carlo software in particle physics

There are many Monte Carlo software programs used in particle physics to simulate the passage of particles through matter. This section presents a brief overview of the main packages in line with the thesis' scope. The following section gives a more detailed description of FLUKA, the main codes used to perform simulation in this thesis.

2.2.1 MNCP

The Monte Carlo N-Particle eXtended (MNCP) [65, 66] software, developed by Los Alamos National Laboratory, is a Monte Carlo radiation transport code that can simulate a wide range of particle species across multiple energy regions in arbitrary geometries. It is used in various fields, such as radiation protection, dosimetry, radiation shielding, radiography, medical physics, nuclear criticality safety, detector design and analysis, etc.

Standard features that make MCNP versatile and easy to use include a powerful general source, criticality source, and surface source; geometry and output tally plotters; a rich collection of variance reduction techniques; a flexible tally structure; and an extensive collection of cross-section data.

MCNP contains numerous flexible tallies: surface current and flux, volume flux (track length), point or ring detectors, particle heating, fission heating, pulse height tally for energy or charge deposition, mesh tallies, and radiography tallies.

2.2.2 PHITS

Particle and Heavy Ion Transport code System (PHITS) [67–69] is a code developed under collaboration between JAEA, RIST, KEK and several other institutes. It can deal with the transport of all particles over wide energy ranges, using several nuclear reaction models and nuclear data libraries. PHITS is written in Fortran language and is originally derived from the NMTC/JAM and HETC-CYRIC codes. However, no knowledge of Fortran is required to use the software as simulation can be specified by preparing an input file written in free-format ASCII text.

The geometrical configuration of the PHITS simulation must be set with either general or combinatorial geometry. The first format adopted in PHITS is very similar to that used in MCNP, and thus, geometries written in the MCNP format can be easily converted into the PHITS-readable format. The interactive solid modeler SimpleGeo can also be used for generating PHITS-readable geometries. Various quantities, such as heat deposition, track length, and production yields, can be deduced from the PHITS simulation using implemented “tally” estimator functions.

2.2.3 EGSnrc

Electron Gamma Shower (National Research Council of Canada) (EGSnrc) [70] is a software toolkit designed to carry out Monte Carlo simulations to transport ionizing radiation through matter. It can simulate photons, electrons, and positrons with kinetic energies ranging from 1 keV to 10 GeV in uniform materials. It was first introduced in 2000 as a comprehensive revision of the Electron Gamma Shower software package, which was initially created at the Stanford Linear Accelerator Center (SLAC) in the 1970s.

The most significant features of EGSnrc include critical improvements in the transport of charged particles, enhanced low-energy cross sections, and the inclusion of the egs++ class library for modeling complex geometries and particle sources. EGSnrc is open source and distributed on GitHub.

2.2.4 GEANT4

GEometry ANd Tracking 4 (GEANT4) is an object-orientated C++ toolkit created by CERN to simulate particles as they interact with different fields and matter. It is a versatile and powerful Monte Carlo-based toolkit that users can customize to meet their needs. It offers many features, including tracking, geometry, physics models, and hits. The physics processes it covers are extensive and comprise electromagnetic, hadronic, and optical processes, as well as a broad set of long-lived particles, materials, and elements. It operates over a vast energy spectrum, in some cases from less than 250 eV to the TeV energy range in others.

GEANT4 is the product of a global collaboration between physicists and software engineers. It has been developed using object-oriented technology and is implemented in the C++ programming language. GEANT4 has found applications in diverse fields such as particle physics, nuclear physics, accelerator design, space engineering, and medical physics.

2.3 FLUKA

FLUKA is a Monte Carlo software designed for the interaction and transportation of hadrons, leptons, and photons in matter and electro-magnetic fields [71–73]. It was created when J. Ranft was working at CERN on hadron cascades under the guide of H. Geibel and L. Hoffmann, and wrote the first high-energy Monte Carlo transport codes. Nowadays, it can operate within a wide energy range, from keV to cosmic ray energies down to thermal energies for neutrons. FLUKA is more efficient and reliable than other Monte Carlo codes, thanks to a careful choice of the algorithms adopted and frequent recourse to look-up tables.

It is designed to incorporate the most comprehensive and accurate physics models, using an approach where each step has a solid physics background. Its reliability is ensured by comparing it with particle production data at a single interaction level. Final predictions are made with minimal free parameters, which remain constant across all energy and target/projectile combinations. The outcomes of complex problems and scaling laws and properties naturally emerge from the underlying physical models. Furthermore, the microscopic approach makes it possible to maintain correlations within interactions and among the components of the particle shower. This approach enables the possibility of making predictions even when no experimental data is available. The code also includes powerful biasing techniques to reduce computational time when necessary significantly.

FLUKA has a wide range of applications, from accelerator and shielding design for radiation protection to particle physics, dosimetry, detector simulation, and hadrontherapy. It can handle even very complex geometries using an improved version of the Combinatorial Geometry package. For most applications, no programming is required from the user. The FLUKA internal code is based on Fortran and utilizes different input files and input cards to work. However, several user interface routines (in Fortran) are available for users who need particular functionalities. For a better user experience, a graphic user interface, called Flair, can be used, which is discussed in more detail in the next section.

Within the scope of this thesis, FLUKA was used to simulate the interaction of the Jefferson Lab's electron beam with the Hall-A's beam dump and to propagate the resulting secondary particles throughout the geometry. Finally, it was also used to simulate, propagate, and perform a conceptual tracking study of the muons generated by the interaction of Jefferson Lab's electron beam and Hall-D's CPS.

2.3.1 FLAIR

Flair [74] is a graphical interface written in python3 [75] to facilitate FLUKA use. It acts as an intermediate layer between the user and the input file, enabling the creation of a complete pipeline—from input creation and simulation to data visualization. One of the main elements of Flair is the geometry editor, Figure 2.1, which provides an intuitive way to build geometries with 3D and multi-angle views, simplifying error debugging.

Another key feature of Flair is the input file editor, which allows easy addition of information to input cards without worrying about formatting errors, Figure 2.2. Possible errors are identified and highlighted, making debugging straightforward. Flair also enables compiling executables and launching simulations directly, with real-time simulation status monitoring. After a successful run, post-processing can be done within Flair, including merging scoring output files and plotting results using GNUPlot [76].

2.3.2 How FLUKA works

FLUKA interprets user input from a "standard input" ASCII file, which is required to supply a basic set of instructions to initiate the simulation. The input is composed of a varying number of "commands" (also referred to as "options"), each of which comprises one or more "lines" (historically known as "cards"), an example of a FLUKA card setting the options for a primary beam is shown in Code 2.3.

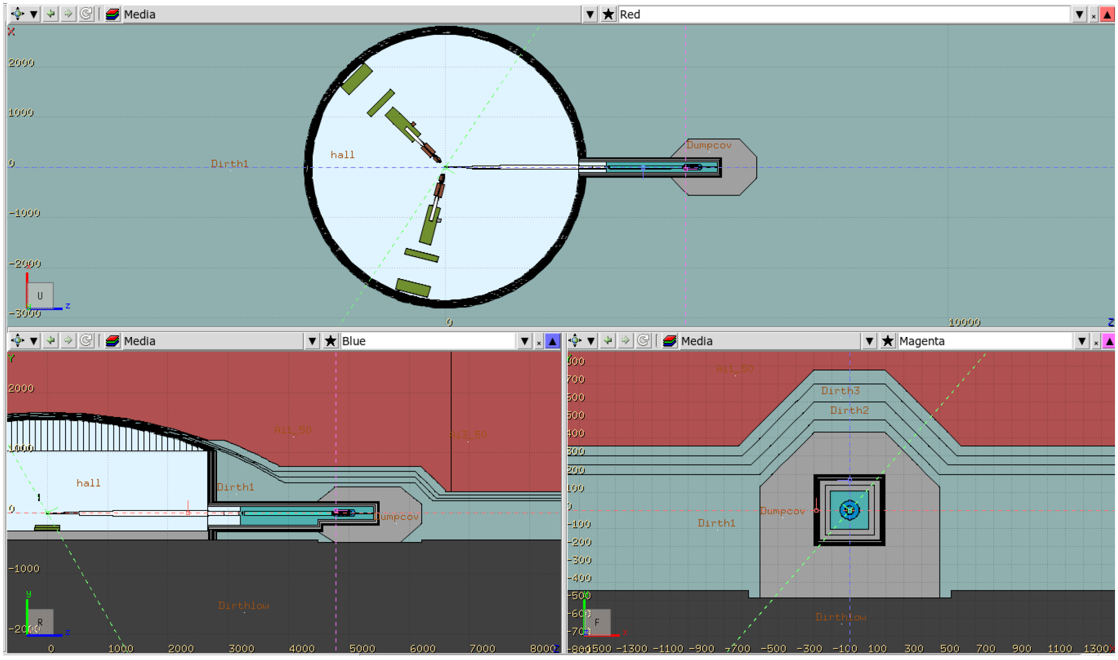

Figure 2.1: Flair's graphical interface showing the geometry of JLab's Hall-A and its beam dump.

FLUKA input card

```
*...+....1....+....2....+....3....+....4....+....5....+....6....+....7...+....
BEAM            11.0      -1.0     0.136       0.5       0.5          ELECTRON
```

Code 2.3: Example of a FLUKA card setting an 11 GeV (momentum) electron beam with a Gaussian spread of 1 GeV (sigma) distributed evenly on a 5×5 mm^2 surface with a divergence of 0.136 mrad.

Each simulation must contain a particle source, such as a beam, with at least its energy specified in terms of momentum or kinetic energy. Furthermore, the beam's position must indicate the source's origin and direction. Following, the geometry and its material descriptions must be included. Finally, the total number of particle sources to be simulated must be specified. These fundamental components are required to run a Monte Carlo simulation with FLUKA [77].

The user's primary and often biggest task is incorporating the required geometry into FLUKA. The types of bodies that can be integrated into FLUKA range from infinite planes, rectangular parallelepipeds, spheres, and cylinders to cones. Boolean geometry is typically favored over CAD geometry due to its better precision. These bodies subsequently create zones embedded in regions with the appropriate assigned material, which can be either pure or compound. It is crucial to remember that each point in the geometry must be allocated to a single region to avoid errors. If a magnetic field

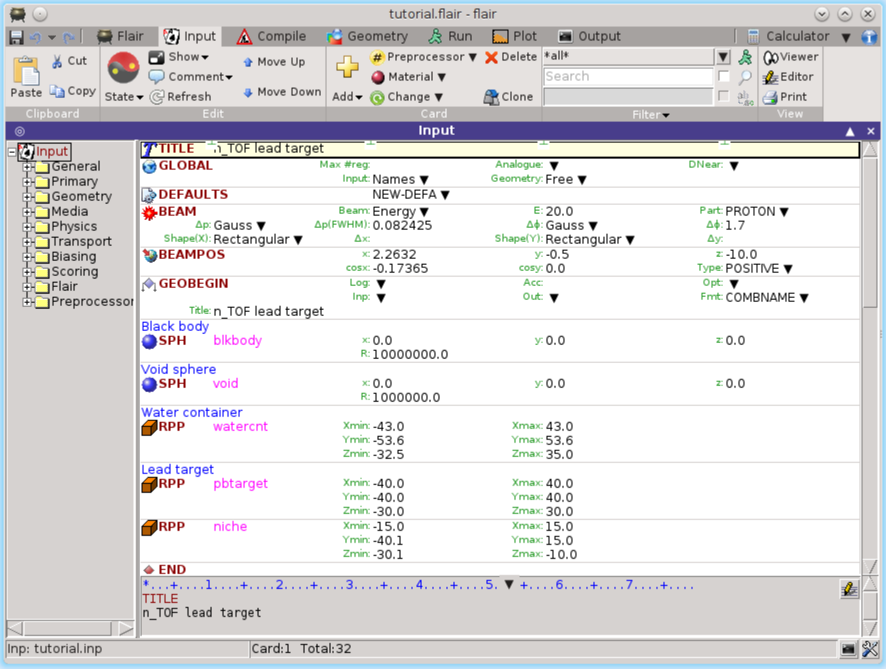

TITLE n_TOF lead target

GLOBAL Max #reg: Analogue: DNear: Input: Names Geometry: Free

DEFAULTS NEW-DEFA

BEAM Beam: Energy E: 20.0 Part: PROTON
Δp: Gauss Δp(FWHM): 0.082425 Δϕ: Gauss Δϕ: 1.7
Shape(X): Rectangular Δx: Shape(Y): Rectangular Δy:

BEAMPOS x: 2.2632 y: -0.5 z: -10.0
cosx: -0.17365 cosy: 0.0 Type: POSITIVE

GEOBEGIN Log: Acc: Opt:
Inp: Out: Fmt: COMBNAME
Title: n_TOF lead target

Black body
SPH blkbody x: 0.0 y: 0.0 z: 0.0
R: 10000000.0

Void sphere
SPH void x: 0.0 y: 0.0 z: 0.0
R: 1000000.0

Water container
RPP watercnt Xmin: -43.0 Xmax: 43.0
Ymin: -53.6 Ymax: 53.6
Zmin: -32.5 Zmax: 35.0

Lead target
RPP pbtarget Xmin: -40.0 Xmax: 40.0
Ymin: -40.0 Ymax: 40.0
Zmin: -30.0 Zmax: 30.0

RPP niche Xmin: -15.0 Xmax: 15.0
Ymin: -40.1 Ymax: 15.0
Zmin: -30.1 Zmax: -10.0

END

```
*...+....1....+....2....+....3....+....4....+....5. ▼ +....6....+....7....+....
TITLE
n_TOF lead target
```

Inp: tutorial.inp Card:1 Total:32

Figure 2.2: Screenshot of Flair's input panel displaying FLUKA cards.

exists, it should also be incorporated into the geometry to represent the actual conditions accurately.

When conducting a FLUKA simulation, the user essentially "scores" or records specific quantities of interest, such as particle fluences, current, track length, energy spectra, energy deposition, etc. This scoring process is similar to taking measurements in a real-life experiment. Like an experimenter uses instruments to measure physical quantities, FLUKA tracks these quantities during the simulation using scorers. These specific input cards instruct the Monte Carlo code on what and where to record the quantities of interest. Among the several options, scoring can be executed region-by-region or within an independent Cartesian or cylindrical mesh. Alternatively, it can also be performed through custom user routines written in FORTRAN, which was primarily done in the work presented in this thesis.

2.3.3 Biasing

Although FLUKA can reproduce faithfully actual particle histories, in many cases, such as those encountered in shielding design, only a tiny fraction of all the histories contribute to the desired response in the regions of interest. This can happen, for instance, behind thick shielding or when the task is to study rare events that naturally lead to a scarcity of the secondaries to be studied. In these cases, the user's concern is not to simulate precisely what occurs in reality but to estimate the desired response in the most efficient way. This can be obtained by replacing the actual physical problem with a mathematically equivalent one.

In such cases, it becomes necessary to introduce what is called "bias" into the simulation, that is to say, a form of alteration to the simulation parameters to improve variance or computational time. Biasing, which comes in several forms, is a potent tool. However, users must exercise caution to avoid inducing non-physical changes in the results. FLUKA offers many forms of biasing, the main two techniques used in almost all the simulations presented in this thesis are *region importance biasing* and *interaction length biasing*.

Region-importance biasing is often considered the simplest form of biasing available. In this thesis, it was used to increase the number of secondary particles moving through heavy materials to achieve faster convergence. In FLUKA, the user can assign different "importance" values to the regions of the geometry. If a particle crosses a boundary between regions with varying values of importance – for example, from region 1 with importance i_1 to region 2 with importance i_2 – then, based on the relative importance of the two adjacent regions $R = i_2/i_1$ an algorithm is used to clone or kill the particle.

If the particle moves towards a region with higher importance, so $R > 1$, then $n = R$ particle replicas are created, each with a weight $w = 1/R < 1$. In this case, the algorithm used is called "Surface Splitting". Vice-versa, if the particle is moving toward a region with a lower importance, so $R < 1$, then it has a survival probability $P_s = R$. If the particle survives, then it will have a weight $w = 1/R > 1$. In this case, the algorithm used is called "Russian Roulette". A scheme summarizing how this bias method is presented in Figure 2.4.

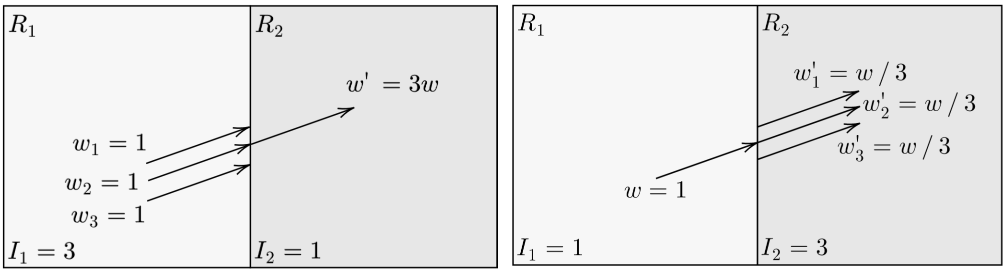

Figure 2.4: Schematic representation of region importance biasing.

Although this biasing method is easy to use and understand, it has some drawbacks. If applied in regions with low-density materials (such as vacuum or air), it can lead to worse results because, in these cases, correlations between particles may be important, and it must be made sure that their further histories are differentiated enough to "forget" their correlation. Additionally, it might require the user to rebuild the geometry if not adequately planned in advance. Finally, the user must be sure to apply this type of biasing at the right step to avoid unwanted effects and distortions on the quantities to be estimated.

The second type of biasing method mentioned falls under the broader category of "Mean Free Path Biasing" techniques. These methods enable the user to multiply the inelastic nuclear interaction length of hadrons, as well as the nuclear interaction length of photons and muons, by a factor λ, so the particles affected will have a weight $w = 1/\lambda$. This type of bias can be used to enhance the production of high-energy muons, as their production cross-sections are very small and thus require much more computational time.

Another form of biasing technique was called "Leading Particle Biasing". It is available only for electrons, positrons, and photons, and it is used to avoid the geometrical increase with the energy of the number of particles in an electromagnetic shower. This type of biasing takes advantage of the fact that in electromagnetic interactions, two particles are present in the final state (at least in the approximation made by most MC codes). Then, it will make only one of the two particles survive with a probability proportional to its energy. Then, its weight is adjusted to conserve the quantity $Q = \text{weight} \times \text{probability}$. Practically, what happens is that the most energetic of the two particles is kept with a higher probability as it is the one that is more efficient in propagating the shower. Leading particle biasing effectively reduces the CPU time needed for the simulation but increases the variance by introducing weight fluctuations.

In this thesis, another variance reduction technique not included in FLUKA was used to efficiently transport low-energy neutrons over long distances. This technique was implemented manually to achieve accurate results at a specific point of the geometry within a reasonable amount of time. This technique works by sampling particles at a chosen boundary between two regions and halting their transportation once they cross this boundary. The key characteristics of these sampled particles are then used to create a multi-dimensional distribution. Events are then sampled from this distribution, injected into FLUKA through a specific user routine, and propagated through the geometry. This same technique can be applied at subsequent boundaries to propagate the particles further. A variant of this technique was also performed using specific machine-learning algorithms.

2.3.4 User routines

Flair is an excellent resource for swiftly constructing, debugging, and running simulations. However, it does have certain limitations when it comes to executing more complex tasks. To address this, FLUKA provides a wide variety of routines that interact with many aspects of the FLUKA code. Written in Fortran, these routines can be tailored to meet the user's requirements. This thesis systematically utilizes these user routines to accomplish specific tasks. In this section, the main routines used, along with their respective purposes, will be presented.

In all the simulations performed for this thesis, FLUKA user routines were utilized in conjunction with the ROOT framework [78]. This process was accomplished by invoking custom functions from an external C++ library within the original FLUKA user routine. Although this method could appear convoluted, it offers a significant advantage over saving the same pieces of information in an ASCII file. The ROOT file occupies considerably less disk space due to its inherent compression and allows for post-simulation analysis using the ROOT framework without any additional steps. Moreover, this method permits the exploitation of ROOT's `TChain` [79] class to merge the results of many runs in a single interface that can interact with thousands of files simultaneously.

The routines `usrini.f` [80] was used to initialize the ROOT file where the simulation's information was saved, while the routine `usrout.f` [81] were employed to save in a `TTree` [82] called `RunSummary` general information about the current simulation (such as the total number of particles simulated, the average time needed to simulate a primary, etc.).

The `mgdraw.f` user routine [83] was used to dump particles as soon as they crossed the boundary separating two chosen regions. These particles and their properties (such as identity, energy, crossing point, angle, etc.) were saved in a `TTree` called `Events`. The same routine dumped similar information when a particle deposited energy inside a selected region, storing them in a `TTree` called `DepEvents`. Lastly, a dump of the source particles (as a mean to cross-check the `source.f` routine) were saved in `TTree` called `SourceEvents`.

The routine `source-newgen.f` [84] was utilized to generate a custom source of primary particles. This routine allows for the customization of all aspects of a beam, offering pre-configured functions for immediate use, such as sampling from a distribution or reading from a phase-space file. This routine, combined with the variance reduction techniques described in subsection 2.3.3, was employed for obtaining results where only biasing was insufficient.

The `magfld.f` [85] user routine was used to assign custom magnetic fields to certain portions of the geometries. With this routine, it is possible to define more complex magnetic fields than the pre-defined ones and was employed to describe the magnetic field of the radiator in the simulation of the CPS described in section 6.1.

Lastly, the routine `usimbs.f` [86] was employed to compensate for the neutron attenuation in concrete, dirt, and lead while still maintaining a reasonable simulation time. A detailed description of its use and implementation is given in section 5.2.1.

Chapter 3

JLab's Secondary Beams

This chapter will introduce the Jefferson Lab, highlighting its main features, the ongoing experimental program, and the planned upgrade to 22 GeV. Later sections will delve into the specifics of Hall-A and Hall-D, detailed respectively in section 3.2 and section 3.3. Finally, subsection 3.2.3 and subsection 3.3.2 will explain the FLUKA geometries and specifics of the settings utilized.

3.1 Thomas Jefferson National Accelerator Facility

The Thomas Jefferson National Accelerator Facility (TJNAF) [87] is a world-leading research institute dedicated to exploring the nature of matter, providing insight into the details of the particles and forces inside the nuclei that build the visible universe. It was established in 1984 in Newport News, Virginia, and is currently operated by Jefferson Science Associates, for the Department of Energy's Office of Science. An aerial photograph of the laboratory is shown in Figure 3.1.

The laboratory's main research facility is the CEBAF accelerator, shown schematically in Figure 3.2. It integrates two linear accelerators, which are built on the principles of superconducting radio-frequency technology. An electron gun generates spin-polarized electrons, which are first preaccelerated near the injector and then accelerated in the north Linear Accelerator (linac). Then, they are deflected in a 180° arc and introduced into the south linac. This last step can be repeated multiple times to reach the required delivery energies for Halls A, B, and C, with a maximum output of 12 GeV for Hall-D. At present, the accelerator is capable of simultaneously delivering beams of up to 200 μA to three end stations with 75 percent polarization and a geometric emittance less than 10^{-9} mrad with a relative momentum spread of a few 10^{-5}.

Since its establishment, CEBAF has received numerous upgrades and enhancements. In the current era of 12-GeV experiments, a suite of new and advanced experimental detectors is available. These include the Super Bigbite Spectrometer (SBS) housed

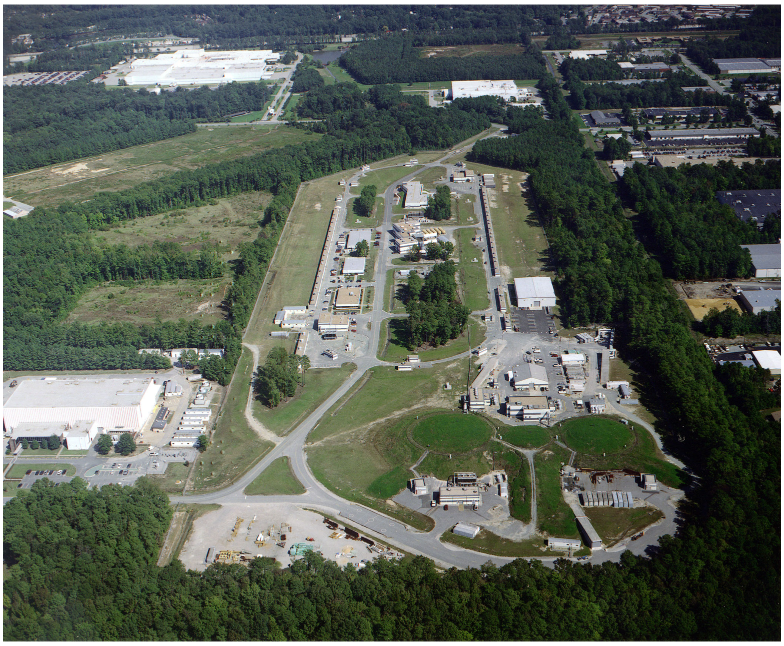

Figure 3.1: Aerial view of the Jefferson Lab, the three main experimental halls can be seen in the lower part of the picture near the bottom road.

in Hall-A, the CEBAF Large Acceptance Spectrometer (CLAS-12) detector complex in Hall-B, and the Super High Momentum Spectrometer (SHMS) located in Hall-C. Additionally, the newly completed Hall-D is home to the GlueX spectrometer and a polarised photon beam, further expanding the facility's capabilities.

Future additions to the experimental equipment include the Solenoidal Large Intensity Device (SoLID) for measurements of Semi-Inclusive Deep Inelastic Scattering (SIDIS), Parity-Violating Deep Inelastic Scattering (PVDIS), and precision measurement of J/ψ production; new large angle tagging detectors (TDIS in Hall-A and ALERT in Hall-B); the neutral particle spectrometer (NPS) for a slate of approved experiments in Hall-C; the compact photon source (CPS) and an intense K_L beamline that would serve new experiments in the GlueX spectrometer in Hall-D. The 12 GeV scientific program overview can be found in [88].

Furthermore, a study to increase the maximum beam energy to 22 GeV is currently underway [89]. Using the fixed-field alternating-gradient technique, it will be possible to increase the number of passes through the accelerating cavities by reusing the same recirculating arcs. The possibility of enhancing CEBAF to higher energies paves the way for a diverse and unique experimental nuclear physics program, prolonging the facility's lifespan well into the 2030s and beyond.

JLab at 22 GeV will conduct world-class science using high-precision, high-luminosity experiments to better understand the properties of quantum chromodynamics (QCD) in

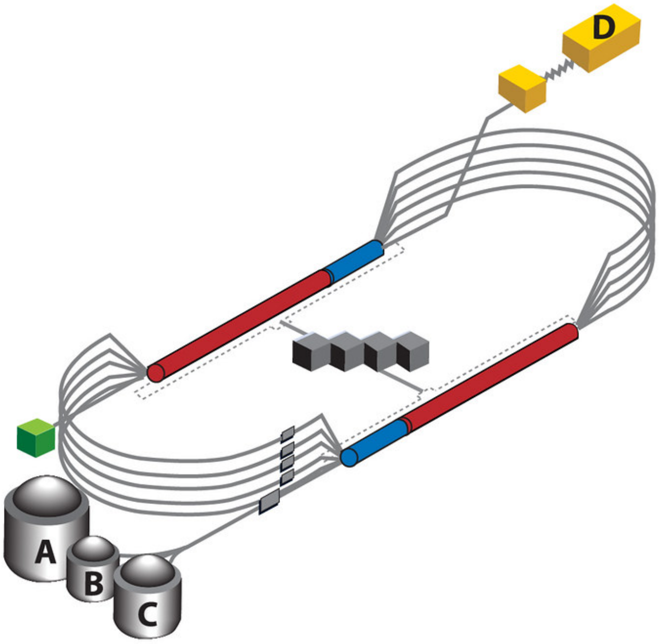

Figure 3.2: Diagram showing CEBAF in its 12 GeV configuration. The four experimental Halls A, B, C, and the newly added D can be seen marked with their respective letters. The left green cube represents the injector, while the center gray ones represent the helium refrigerators. The top red and blue cylinder represents the north linac, while the bottom represents the south linac.

the valence regime. It will also allow researchers to investigate the transition to a region of sea dominance by accessing hadrons with larger masses and different structures.

In hadron spectroscopy, a unique production environment of exotic states will be examined, yielding cross-section results that supplement those from high-energy facilities. This could be crucial in deciphering the nature of certain pentaquark and tetraquark candidates, specifically those containing charm and anti-charm quarks.

Moreover, it will permit the exploration of the gluonic structure of the proton through precise measurements of the photo and electroproduction cross-section near the threshold of J/Ψ, χ_c, and $\psi(2S)$ charmonium states. In particular, precision measurements of the radiative decay width of π^0 off an electron will be performed for the first time. This will enable sub-percent precision on $\Gamma(\pi^0 \to \gamma\gamma)$, essential to reconcile the discrepancy between current experimental results and high-order QCD predictions.

The forthcoming 22 GeV upgrade will also extend the phase space for studying the momentum space tomography of nucleons and nuclei via the transverse momentumdependent (TMDs) parton distribution functions. This upgrade will also be crucial for conducting experiments on elastic and hard-exclusive processes, offering critical insights for precision studies of partonic structures. The 22 GeV scientific program overview can be found in [90].

3.1.1 Secondary beams at JLab

In addition to the extensive range of experiments currently in progress for the 12 GeV program and those proposed for the 22 GeV program, new opportunities can be found using secondary particle beams. Intense secondary beams are produced by the interaction of the CEBAF electron beam with the BDs of the four respective Halls. Among these, Hall-A and Hall-C stand out as the most suitable candidates.

Both Halls are equipped with high-precision magnetic spectrometers, which small acceptance requires high current (1–150 μA) on target to reach the typical luminosity of 10^{39} cm^{-2}s^{-1}. The current BD configuration limits the maximum power to <1 MW corresponding to 90 μA current at 11 GeV beam energy or higher current at lower energy. High-current experiments with long durations are planned for Hall-A in the next decade, while the number of running days per year for Hall-C will be more sparse. While Hall-B and Hall-D host two large-acceptance spectrometers (CLAS12 and GlueX) based on a toroidal (CLAS12) and solenoidal (GlueX) magnetic field. The almost 4π acceptance limits the current to hundreds of nA in Hall-B and to a few μA in Hall-D's radiator (to generate a Bremsstrahlung real-photon beam). Dumps installed in these two halls are limited to a power of $\sim$100 kW, reducing the intensity of the incoming primary beam to values unsuitable for generating intense secondary beams.

For these reasons, the high-current operations make Hall-A BD the ideal source of secondary beams at Jefferson Lab. The studies conducted on this topic will be explored in chapter 4, chapter 5 and chapter 5.

Another opportunity of a secondary beam can be found within the currently planned Compact Photon Source (CPS) in Hall-D's Tagger Hall. Built to generate an intense secondary beam of K_L, this new facility will also produce an intense beam of muons. This possibility will be detailed in section 6.1.

3.2 The Hall-A

Hall-A is the largest of Jefferson Lab's experimental halls, and it is used primarily for experiments that study the structure of nuclei, protons, and neutrons. It is equipped with two identical high-resolution spectrometers that provide a high momentum resolution and multiple pieces of equipment for particle identification like Cherenkov counters, scintillators, and lead-glass calorimeters [91]. A schematic representation of Hall-A is shown in Figure 3.3.

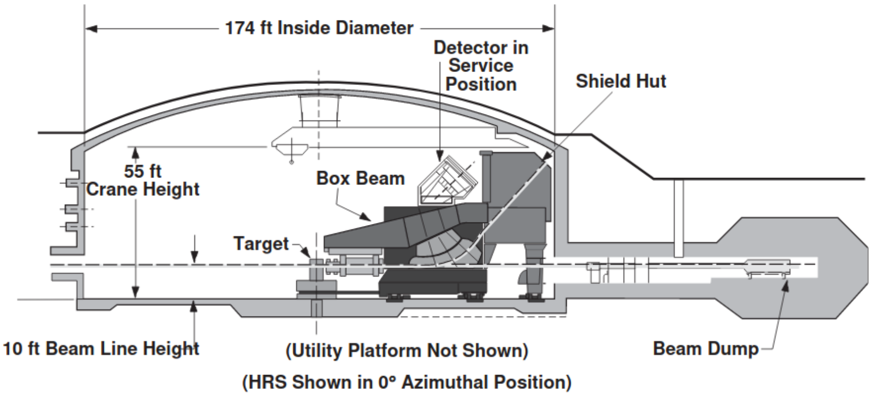

Figure 3.3: Schematic side view of Hall-A's layout. The electron beam enters the Hall through a narrow beam pipe on the left and hits the target at the center of the Hall. The reaction products are analyzed using the detectors on the right part of the Hall. The BD is depicted on the far right.

JLab's electron beam enters the Hall through a narrow beam-pipe channel made of stainless steel aimed towards the target (from the left to right of Figure 3.3). The equipment along the beam line consists of different components required to transmit the electron beam onto the target and into the dump while simultaneously measuring the appropriate beam characteristics. Typically, the target is housed within a huge sealed canister, and when the beam collides with it, the particles that escape are focused and separated by large magnets. Finally, the electron beam ends in the BD.

Nowadays, Hall A has transitioned into a long-term experimental hall supporting significant projects like the Super BigBite Spectrometer (SBS), the MOLLER experiment, and SoLID, each designed for advanced particle physics research. The hall retains its original High Resolution Spectrometer (HRS), built in the 1990s, offering momentum measurements between 0.3 and 4 GeV/c. To accommodate high-precision parity-violation studies, the beamline—now upgraded with advanced monitors and polarimeters—supports operations up to 11 GeV.

SBS, with its dual single-bend spectrometers and large calorimeters, allows detailed investigations of nucleon form factors and other scattering phenomena. MOLLER, by observing the parity-violating asymmetry in electron scattering, provides insights into the weak charge of the electron and the electroweak mixing angle. The versatile SoLID apparatus enables high-luminosity studies and can be reconfigured for either deep inelastic scattering or meson production, expanding Hall A's capabilities for contemporary nuclear and particle physics research.

3.2.1 The Hall-A beam dump

The Hall-A BD consists of approximately 80 aluminum disks, each with a diameter of roughly 40 cm. The disk thickness progressively increases from 1 cm to 2 cm, spanning a cumulative length of about 200 cm. Downstream of the disks, there is an aluminum cylinder measuring 50 cm in diameter and approximately 100 cm in length. A schematic 3D view of the Hall-A BD is shown in Figure 3.4. Disks and cylinders are thermalized using a water-cooling circuit to ensure optimal temperature control. To enhance the radiation shielding capabilities, the BD is surrounded by ∼8 m of concrete in the longitudinal direction (where the high-energy secondary particles are produced) and about ∼3 m of concrete in the transverse direction. Furthermore, the entire setup is covered by ∼4 m of overburden made of dirt.

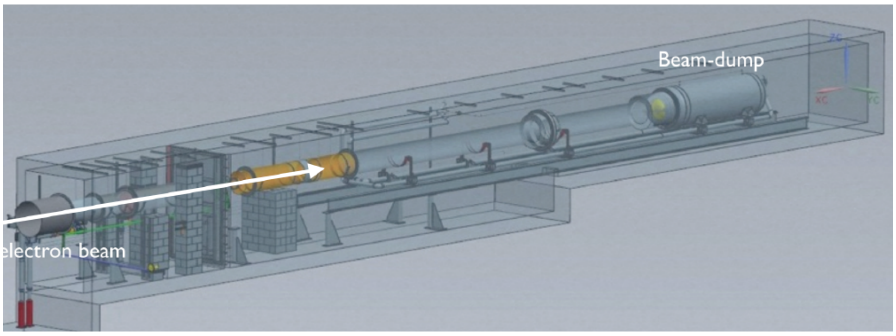

Figure 3.4: CAD model of the Hall-A BD enclosure in the concrete tunnel. The electron beam entering the BD enclosure is represented with a white line on the left.

3.2.2 The Beam-Dump eXperiment

The research conducted for this thesis is an extension of the beam-on background studies performed for the BDX experiment. The Beam Dump eXperiment (BDX) is a proposed Jefferson Lab experiment aimed at producing and detecting Light Dark Matter (LDM) particles predicted by vector-mediated LDM theoretical models [92]. BDX uses CEBAF high-intensity (65 µA) 11 GeV electron beam impinging on the JLab's Hall-A BD. The interaction between the electrons and the atoms of the dump leads to the production of Dark Matter, χ, which travels almost unaltered through the length of the dump to the BDX detector. The scattering is detected by capturing the high-intensity electromagnetic shower generated by the collision with a device known as a "BDX detector" [93], a GEANT4 drawing of the proposed BDX can be seen in Figure 3.5.

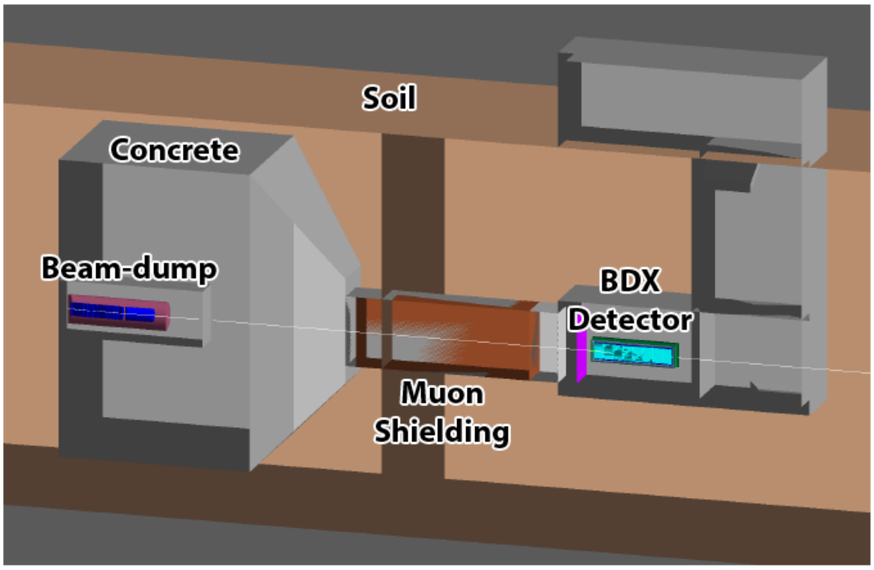

Figure 3.5: The figure illustrates the BDX setup in GEANT4. On the left, the concrete enclosure of the BD is shown in gray. The aluminum cylinder of the BD is depicted in brown, with the recirculating water represented in blue. The proposed new Hall for BDX is shown in gray on the right with the BDX detector shown in light-blue. The brown area between the hall and the BD enclosure represents the passive muon iron shielding. The white line represent the dark matter produced in the BD.

The detector will be housed in a new underground building $\sim$ 20 m downstream of the experimental Hall-beam A's dump, which will function as a general-purpose facility for any future BD investigations. The BDX detector, shown schematically in Figure 3.6, is composed of two major components: an electromagnetic calorimeter (ECal) constructed of a matrix of inorganic scintillating crystals, which detects signals, and a veto detector, to reject charged particles background. The veto detector is made up of two layers of plastic scintillators called the Inner and Outer Veto. A 5 cm thick sheet of lead is put between the ECal and the vetoes to protect it from the low energy products of the electromagnetic showers leaving the ECal.

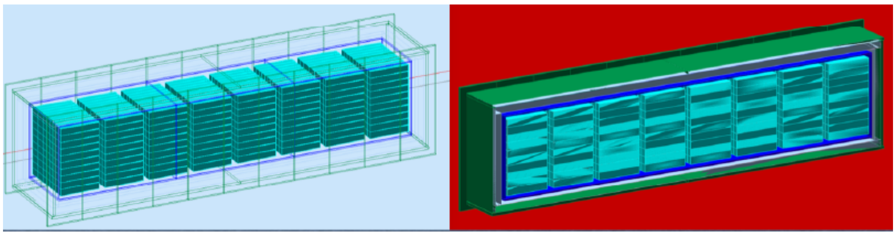

Figure 3.6: GEANT4 implementation of the BDX detector. On the right, the Outer Veto is shown in green, the Inner Veto in blue, the lead in gray, and the crystals in cyan.

A small fraction of LDM particles may scatter off electrons in the detector, giving rise to an electromagnetic shower of order ~ 100 MeV. The expected low signal rate makes the background rejection a critical issue for BDX. To range out all SM particles (except neutrinos), further passive shielding needs to be located behind the BD. One of the results of this work was defining the best shielding configuration. BDX will be able, with 280 days run.

3.2.3 The Hall-A Simulation Framework

FLUKA and GEANT4 were the software used to study and characterize the interaction between the CEBAF electron beam and the BD. FLUKA was used to perform Monte Carlo simulation for muons and neutrinos, while GEANT4 was used for simulations regarding LDM. The Hall-A BD geometry and materials were implemented in FLUKA according to the prescriptions of JLab Radiation Control Group [94] and generously provided for the studies performed in this thesis. The BD, the beam transport line, the surrounding concrete vault, and the BDX vault are shown (to scale) in Figure 3.7.

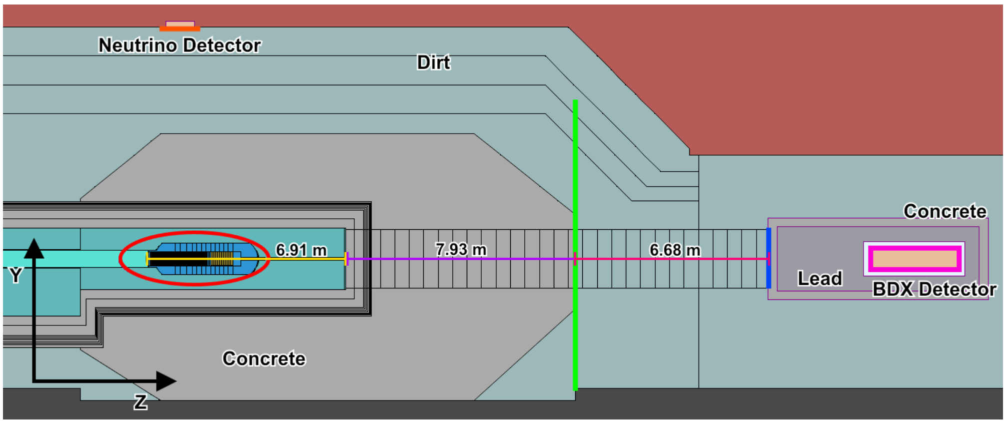

Figure 3.7: To-scale side cross-section of the Hall-A BD geometry with the two flux-detectors used in the simulations to evaluate the flux of secondary particles. Perpendicular to the BD, in orange, is shown the flux detector corresponding to the location of a hypothetical neutrino detector. The aluminum disks of the BD inner core are shown in yellow. Downstream of the BD, immediately after the concrete vault, a green sampling surface of 12×9.8 m^2 is placed to sample all the particles that exit from the vault in the forward direction.

All the simulations presented in this thesis utilized the `PRECISIO` [95] settings as a base. Then, several more cards were included to enable/disable and tune physical processes of interest. The following list presents all the additional options used:

- Enabled the simulation of muon nuclear interactions and production of secondary hadrons
- Enabled the bremsstrahlung by high-energy muons, charged hadrons, and light ions (up to alpha's)

- Enabled photonuclear interactions at all energies
- Enabled muon pair coherent, incoherent quasi-elastic, incoherent inelastic, and deep inelastic production
- Enabled electro-nuclear interactions at all energies
- Enabled the phase-space-like decays for pions, kaons, and muons
- Enabled the use of the evaporation model for nuclei
- Enabled the coalescence mechanism
- Enabled the splitting of ions into nucleons.

The following cut and transport options were used:

- Enabled the transport of neutrinos of all species
- Activated the point-wise transport of neutrons
- Set energy thresholds for electrons, positrons, and photons production to 100 MeV
- Set energy transport cut-off for electrons, positrons, and photons to 100 MeV
- Set energy transport cut-off for muons, pions, kaons, and protons to 99 MeV (to activate their decay at rest [96])

Also, a tuned set of biasing techniques (described in subsection 2.3.3), weights, and routines were included to speed up the computational time of the simulations:

- The cross-section for the process $\gamma \rightarrow \mu^+\mu^-$, responsible for the production of high-energy muons in the dump, was artificially enhanced from 10^5 to 10^6, depending on the simulation
- The cross-section for photon-induced hadronic reactions was artificially enhanced by 10^2
- Set "leading particle bias" electromagnetic processes
- Importance-sampling by splitting was also implemented
- `USIMBS` user routine implementation to compensate for low-energy neutron attenuation in concrete, soil, and lead
- `USIMBS` user routine implementation for directional biasing of low-energy neutrons

For reference, in Table 3.1, the composition (raw number of atoms or mass fraction) and density of a few key geometry materials are shown.

Material	**Composition**	**Density (g/cm^3)**
Concrete	$O_{40}C_{23}Si_{12}Ca_{12}H_{10}Mg_2$	2.34
Dirt	$(H_2O)_{17.5\%}(SiO_2)_{82.5\%}$	2.0023
Lead		11.35

Table 3.1: Composition, in raw atom number (for Concrete) and mass fraction (for Dirt), and density for materials surrounding the BD and for the shielding of the BDX vault.

LDM flux was computed using GEANT4 via the GEMC interface [97]. The Hall-A BD geometry implemented in GEMC is shown in Figure 3.8.

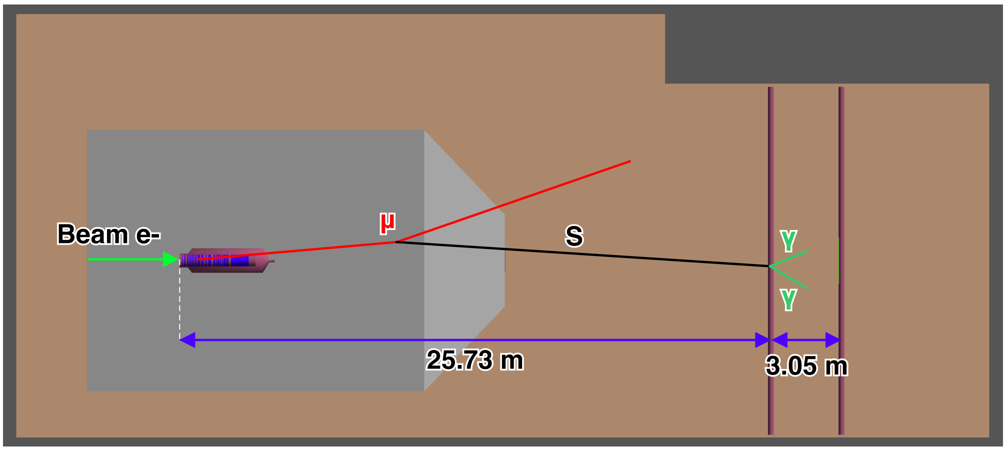

Figure 3.8: Hall-A BD and surrounding dirt implemented in GEMC. The BD vessel, shown in purple, contains Al foils, which are shown in blue. The concrete vault is shown in gray, while the dirt is in brown. Two existing 10" pipes installed ∼26 m and ∼29 m downstream of the dump [98] are shown in purple. A scheme of Dark Scalar production and decay is also presented.

The simulation procedure is divided into several steps. It starts by sampling muon features obtained with FLUKA simulations. The multidimensional distribution, which includes three-momentum, production vertex, statistical weights, and total yield per Electrons On Target (EOT), was converted in the LUND format [99] (particle ID, vertex, and momentum) and fed to GEMC.

The interaction of muon with nuclei that produces a new hypothetical dark matter scalar particle S was added to the GEMC process list. The process has been implemented according to the prescription described in [61], with a more precise production cross-section and subsequent propagation and decay [60]. The new class, `G4Scalar`, containing a `G4ParticleDefinition` instance to include the new *S* particle, was implemented in GEMC libraries.

The class initialization requires two parameters: the mass of the scalar and the coupling to the standard model (SM). This allows one to dynamically set the particle properties at the beginning of the simulation. The LDM particle is then set to be unstable, with lifetime evaluated analytically following [60]. A single decay channel ($S \to \gamma\gamma$) was implemented using the standard GEANT4 `G4PhaseSpaceDecayChannel` routine.

Chapter 4 will present the findings on the secondary muon and LDM beam, while chapter 5 will present the results on the secondary neutrino beam. Finally, chapter 5 will discuss the studies conducted for the beam-related neutron background. The simulations were performed considering an 11 GeV electron beam, as this is the nominal maximum energy allowed in the BD. In addition, a study was carried out considering a 22 GeV beam in anticipation of the future CEBAF upgrade. The majority of the results will be presented as the ratio of *particles* to EOT. This method simplifies extrapolation when considering a certain beam-on time. Specifically, a beam-on time of one year corresponds approximately to 10^{22} EOT.

3.3 The Hall-D

The Hall-D complex is the most recent addition to the four experimental halls at Jefferson Lab. The complex is a rather large group of facilities that starts at the north end of the CEBAF, it is shown in yellow in Figure 3.2. The beamline, shown schematically in Figure 3.9, includes a dedicated Tagger Hall, an associated collimator cave, and the Experimental Hall-D itself. Hall-D is designed for experiments with a photon beam, and its primary motivation is the Gluonic Excitation (GlueX) experiment [100], built to search for and map out the spectrum of exotic hybrid mesons using a 9-GeV linearly-polarized photon beam incident on a proton target.

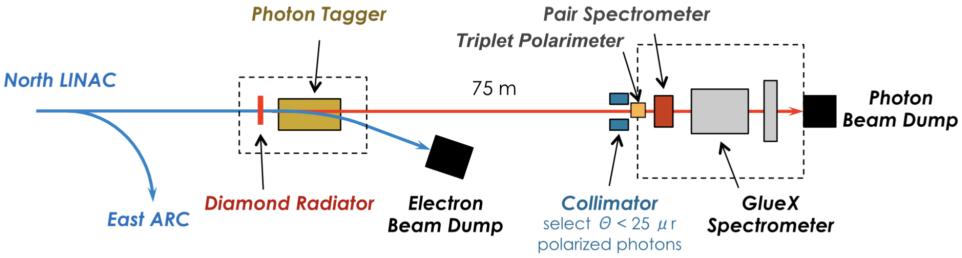

Figure 3.9: Schematic representation of the Hall-D complex, illustrating the Tagger Hall, Hall-D, and other significant beamline apparatus.

First, the electron beam is extracted from CEBAF at 5.5 passes (up to 12 GeV) and directed to the Tagger Hall. Here, it traverses a diamond radiator, approximately 0.02–0.05 mm, and is deflected by a dipole magnet toward a beam dump. Electrons that have emitted between 25% and 96% of their initial energy are redirected by the magnet to tagger scintillator detectors, achieving an energy resolution of about 0.1% for the beam photons. The radiator is oriented to facilitate coherent radiation, with a peak energy at approximately 75% of the beam energy. Positioned 75 meters downstream of the radiator, a 3.4 or 5.0 mm collimator enhances the fraction of coherently produced photons in the photon beam. This collimated beam is then analyzed by the Pair Spectrometer, comprising a thin converter, dipole magnet, and scintillating hodoscopes. Additionally, a Triplet Polarimeter measures the linear polarization of the beam. Ultimately, the beam is directed toward the GlueX spectrometer.

The GlueX experiment utilizes a 30 cm liquid hydrogen target, with liquid helium and solid targets employed for other experimental setups. Charged particle trajectories are tracked through the Central and Forward Drift Chambers, while photon detection is handled by the Barrel (BCAL) and Forward Calorimeters. Timing measurements, essential for event selection and particle identification, are provided by the Start Counter surrounding the target, along with the time-of-flight counter and BCAL. At the end of 2019, the spectrometer was upgraded with a DIRC Cherenkov detector for the GlueX-II phase of the experiment. The front-end electronics pipeline manages both event selection (trigger) and Data Acquisition (DAQ). Experiment luminosity is constrained by the accidental rate in the tagger counters and DAQ performance. The GlueX experiment operates with a relatively open trigger based on calorimeter signals, achieving high efficiency for most photoproduction processes at photon beam energies above 4 GeV.

3.3.1 The Hall-D's K_L Facility and the Compact Photon Source

Recently, a design concept for a compact, high-intensity, multi-GeV photon source capable of producing 10^{12} equivalent photons per second is being studied for Hall-D [101]. This new Compact Photon Source (CPS) aims to offer access to physics processes characterized by extremely low scattering probabilities, such as hard exclusive reactions on the nucleon. The addition of a CPS to this Hall opens the door to the production of secondary beams of other particles, such as a K_L beam [102] and a μ beam. The latter is explored in section 6.1.

For the operation of the K_L facility, the electron beam has been proposed to have a power of up to 60 kW, running at an energy of 12 GeV with a 64 ns beam bunch spacing. Preliminary calculations indicate that the standard CPS setup can accommodate the power deposition. The size of the photon beam generated by the CPS is dominated by multiple scattering in the radiator and is estimated to be 2 cm after traveling 80 m. This is well within the size of the 15 cm diameter beam pipe and the 6 cm diameter Be K_L target. Furthermore, if the CPS radiator is retracted, the current Hall-D photon beam can be used without moving the CPS or any other modification from the beamline.

Traditional techniques for producing high-energy photon beams involve striking a radiator with an electron beam, resulting in a mix of photons and electrons. However, this method, while producing a large flux of photons, has drawbacks such as unknown photon beam energy and potential for large radiation background dose. An alternative technique involves using a radiator, a deflection magnet, and a BD for the undeflected electrons. This method produces a pure photon beam, but the photon flux is less than might be possible due to the need to keep detector rates manageable.

The proposed CPS concept, shown in Figure 3.10, addresses the shortcomings of the other two techniques by combining all elements necessary for the production of an intense photon beam into a single shielded facility. The CPS design features a magnet, a central copper absorber, and materials to shield the induced radiation dose. This approach significantly reduces radiation leakage and offers several advantages over traditional methods, including an intense and narrow pure photon beam and much lower radiation levels.

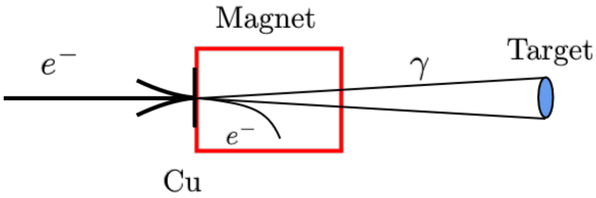

Figure 3.10: Different schemes to produce high-energy photon beams.

3.3.2 The Hall-D Simulation Framework

The secondary muon beam produced by the interaction of the CEBAF electron beam and the CPS was studied using FLUKA. Moreover, a conceptual tracking of the muons was conducted using the `python` programming language to assess the possibility of performing a muon missing momentum similar to the M^3 experiment proposed at FermiLab [41] briefly discussed in section 1.1.1.

The geometry and materials of the CPS were initially implemented into FLUKA by the CPS collaboration group, who kindly provided them for the research conducted in this thesis. Moreover, several modifications were introduced to adapt the geometry to the specific requirements of the tracking study.

Specifically, the CPS was repositioned 1 meter backward to incorporate a magnetic dipole into the geometry, designed to deflect muons away from the primary photon beam-line. Subsequently, a shielding composed of lead and borated concrete was introduced before the tracking area to reduce the background neutrons and photons. Following this, two magnetic dipoles and a target were added. Their positions were determined based on the specifications for a 2 T, 50 cm long dipole. These two dipoles are designed to measure the momentum of the muon both before and after it interacts with the target, which is situated between the two. Lastly, two volumes representing an electromagnetic and a hadronic calorimeter were incorporated. The modified geometry is shown (to scale) in Figure 3.11 with each element highlighted. Table 3.2 describes all the new components incorporated into the geometry.

The simulations for the CPS were conducted based on the `PRECISIO` settings. They included the same extra options detailed in subsection 3.2.3, with the exception of those related to neutrinos. These simulations were carried out using a 12 GeV electron beam striking the CPS radiator. For the same reason described in subsection 3.2.3, the results will be displayed as the ratio of *particles* per EOT.

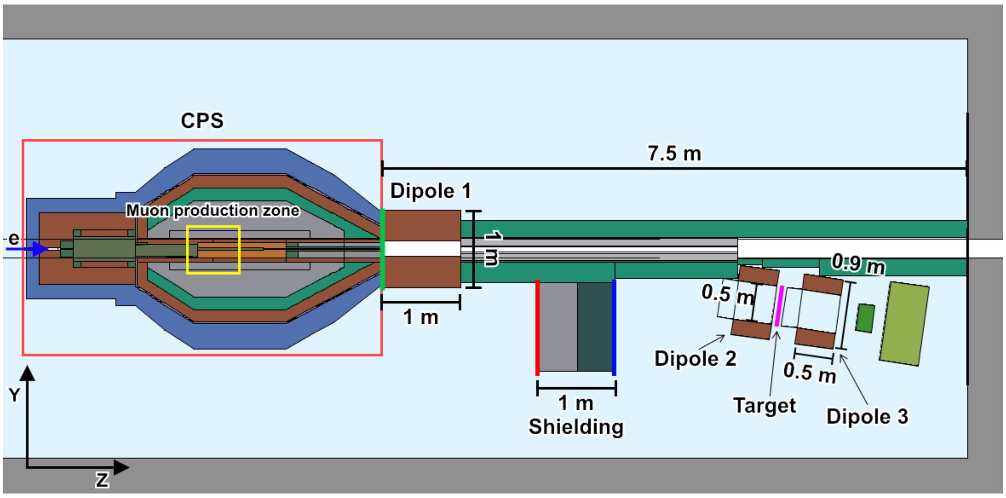

Figure 3.11: The figure shows a to-scale side cross-section of the CPS geometry. On the left, the red box outlines the entirety of the CPS. Inside this, a yellow box highlights the area where most muons are produced either by photoproduction or hadron decays processes. At the exit of the CPS, a 1 m^2 sampling surface is placed to sample all particles escaping from the CPS. Following this, a 2 Tesla, 1-meter-long dipole is positioned to bend the muons under the beamline. Right after the dipole, the green area represents the passive shielding around the beamline. On the right, beneath the beamline, several components constitute the setup for a missing momentum experiment. These components include a 50 cm long wall of concrete and a 50 cm wall of lead to shield the setup from secondaries coming from the CPS, two dipoles to track the muons, a target to scatter the muons, and both a hadronic and an electromagnetic calorimeter.

Element		**Material**	**Dimension** (x, y, z) **[cm]**	**Magnetic field** (B_x, B_y, B_z) **[T]**
Dipole 1	Yoke	Iron	$92, 100, 100$	$0, 0, 0$
	Bore	Vacuum	$10, 20, 100$	$2, 0, 0$
Dipole 2	Yoke	Iron	$80, 90, 50$	$0, 0, 0$
	Bore	Vacuum	$20, 50, 50$	$-2, 0, 0$
Dipole 3	Yoke	Iron	$80, 90, 50$	$0, 0, 0$
	Bore	Vacuum	$20, 50, 50$	$2, 0, 0$
Shielding	1st half	Lead	$100, 114, 50$	$0, 0, 0$
	2nd half	Concrete	$100, 114, 50$	$0, 0, 0$

Table 3.2: Summary of all the CPS elements needed for performing a missing momentum experiment.

Chapter 4

JLab's Hall-A Secondary Muon & LDM Beam

This chapter investigates the possibility of generating an intense muon beam from the CEBAF electron beam impinging on the Hall-A BD. Detailed results of Montecarlo simulation of muons produced by the interaction of CEBAF 11 GeV e^--beam with Hall-A BD are shown in subsection 4.1.1. While in subsection 4.1.2, results of Montecarlo simulations using a 22 GeV electron beam for the coming CEBAF upgrade will be presented. Moreover, in section 4.1.1, a study for a new passive shielding design for the BDX's detector is presented. Finally, in section 4.2, the possibility of producing a LDM beam from 11 and 22 GeV muons is discussed.

4.1 Secondary Muon Beam

High-intensity multi-GeV electron beam hitting a thick target is likewise a copious source of muons, as shown in section 1.1.2. In brief, muons are produced via three classes of processes:

- photo-production of π's and K's, which subsequently decay into muons;
- direct $\mu^+\mu^-$ pair production;
- direct electro-production reaction $e^- + N \rightarrow e^- + N + \mu^+\mu^-$, however, the muon yield from this process is practically negligible, as showed in [42].

Radiated muons are strongly peaked in the forward direction with energy comparable to the primary beam energy. Instead, muons produced via decay in flight of photo-produced π's and K's show a lower energy spectrum.

To achieve better statistics and faster convergence of the results, the following biasing techniques (described in detail in subsection 2.3.3) and cuts were employed:

- Mean free path biasing of the photon interaction length of photons with nuclei, to enhance by 10^6 the production of high-energy muons in the dump and by 10^2 the photon-induced hadronic reactions.
- "Leading particle bias" to speed up the computational time of lower energy electron-magnetic cascades.
- Importance-sampling by splitting using regions of increasing importance from the dump to the detector.
- Particle transport threshold fixed to 100 MeV for all particles except neutrinos.
- Particle transport threshold fixed to 10 MeV for neutrinos.

Moreover, the simulation made use of custom FLUKA user routines to achieve the dumping of the results directly into ROOT files. This was possible by linking the C++ ROOT libraries to the FLUKA executable and calling *ad hoc* functions with the user routines. Muons were sampled across several surfaces through the geometry using the `mgdraw.f` user routine and all of their proprieties (like position, momentum, direction, identity, etc) were saved inside TTree. A custom implementation of the `source_newgen.f` user routine was used to generate muons to evaluate an upper limit to the number of muons entering the BDX detector with different shielding configurations.

4.1.1 11 GeV Electron Beam

The results presented in this section are derived from multiple simulations conducted on the Jefferson Laboratory and CNAF computing farms. Both farms are robust and versatile computing environments featuring a diverse mix of cutting-edge and legacy hardware. The first one has approximately 20,000 nodes, while the latter has approximately 5,000 nodes. Both farms are designed to handle various computational tasks, from high-performance simulations to data-intensive analyses.

Both farms run on Alma Linux, a stable and secure operating system. They come pre-installed with several scientific computing software packages, like ROOT and Python. Additionally, users have the flexibility to install their own software within their personal environments.

The simulations performed to account for a total $\sim 5 \times 10^8$ primary electrons impinging on the Hall-A BD with momentum $p_{e^-} = 11$ GeV.

The spatial distribution on the yz-plane of the point where the muons were produced is shown in Figure 4.1 with the outline of the BD superimposed. This plot shows that muons are copiously produced in the first few meters of the BD while a smaller proportion is generated in the surrounding area. This pattern mirrors the muon beam behavior observed at SLAC, as referenced in section 1.1.2.

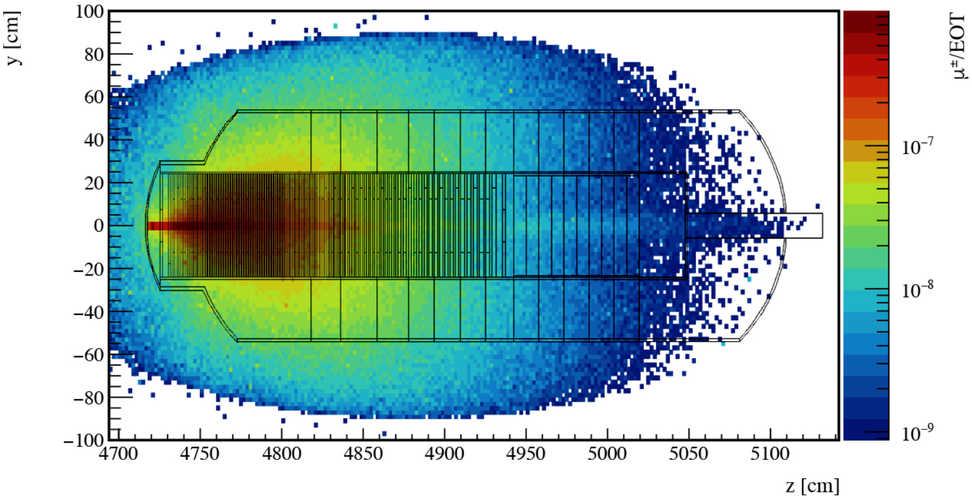

Figure 4.1: Muon production vertexes both in the vicinity of the BD and within the BD itself. The outline of the BD is shown in black over the plot.

The momentum spectrum of the muons coming out of the BD, sampled on the red oval surface of Figure 3.7, is shown in Figure 4.2. Muons from pair production processes are shown with a red line, while muons from hadron decays are shown with a black line. The blue line, instead, represents the overall spectra. In this plot, the x-axis is divided into logarithmic bins and shown in logarithmic scale to emphasize better muons coming from the decay-in-flight of π's and K's that dominates muon production below 2 GeV.

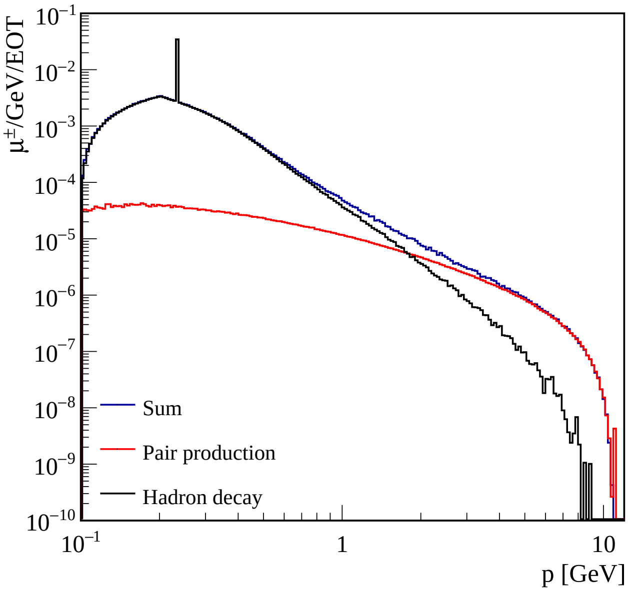

Figure 4.2: Momentum spectrum of muons at the boundary between the inner core of BD and the outer one with $p > 100$ MeV produced by 11 GeV electron beam. Pair production is shown in red, and hadron decays in black. The integrated spectra ratio between muons from hadron decay and pair production ~ 15. The peak at 235 MeV is due to the kaon decay-at-rest process $K \rightarrow \mu + \nu_{\mu}$.

Subsequently, the muon flux was sampled on a 1 m^2 surface centered around the beam-axis located 10 m downstream of the BD, and perpendicular to the primary e^--beam direction (corresponding to a smaller portion of the green thick line in Figure 3.7).

In the forward direction, the momentum distribution of the muons coming out from the concrete vault surrounding the BD is shown in Figure 4.3. Muons up to 6 GeV are presented, as beyond this threshold, the number of muons per EOT decreases by several orders of magnitude, reducing to an insufficient level for experimental use.

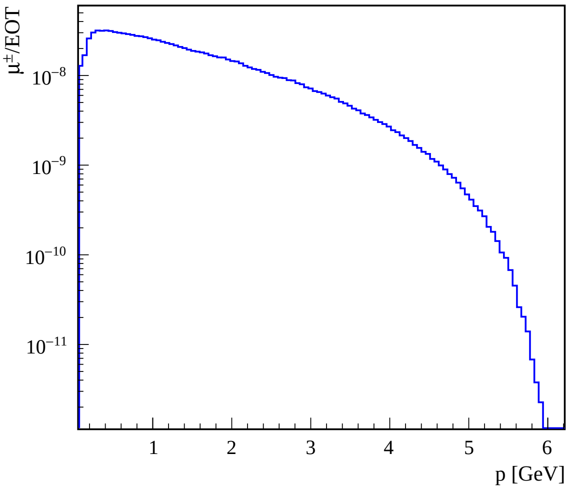

Figure 4.3: Muon momentum distribution produced by an 11 GeV electron beam interacting with the Hall-A BD sampled on a 1 m^2 flux detector downstream of the concrete vault enclosing the beam dump.

The resulting muon yield per EOT, integrated over $p_\mu > 100$ MeV, is $\sim 10^{-6}$ μ/EOT. Therefore, for a primary e$^-$-beam current of 50 μA the corresponding muon rate is $\sim 10^8$ μ/s. These results show the advantage of secondary muon beams produced at multi-GeV electron BD facilities when compared to the typical intensity of existing proton-beams-produced muon beams with similar energies (the Fermilab accelerator complex, for example, can deliver a muon beam of about 10^7 μ/s at the so-called *magic momentum* of about 3 GeV [103]).

Considering the muons sampled on the same flux detector, their spatial distribution (left) and correlation between their momentum and direction (right) are plotted in Figure 4.4. The left plot shows that ~50% of the muons cross the plane within an area of roughly 50 × 50 cm^2. The right plot shows that higher-energy muons are mostly produced in the forward direction.

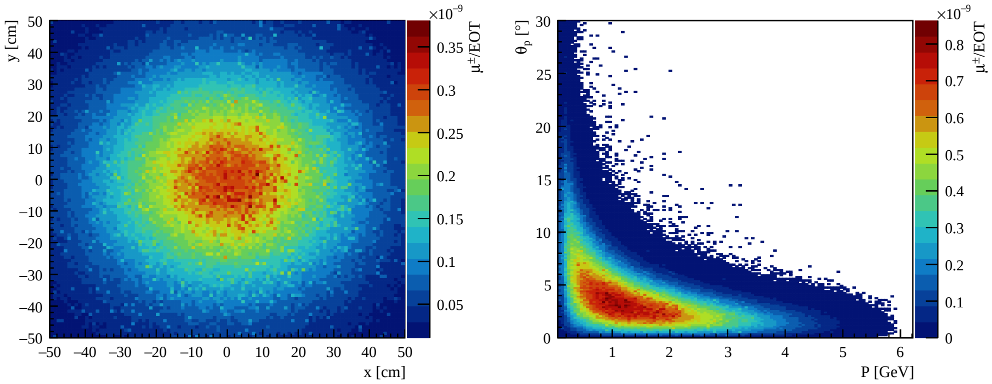

Figure 4.4: Left: muon spatial distribution produced by an 11 GeV electron beam interacting with the Hall-A BD sampled on a 1 m^2 flux detector downstream of the concrete vault enclosing the beam dump. Approximately 50% of all the muons cross the flux detector within an area of roughly 50 × 50 cm^2. Right: muon direction versus momentum. This plot shows that higher-energy muons are produced in the forward direction.

To determine the size of the muon beam at the end of the concrete downstream of the BD's vault, the spatial distribution was projected along x and y and subsequently fitted with a Gaussian distribution. These plots are shown in Figure 4.5. The sigma values for both projections derived from this fit are approximately 25 cm. The results of this section are summarised in Table 4.5.

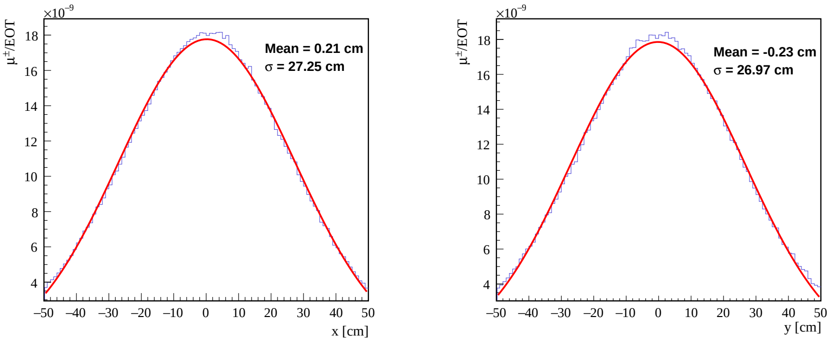

Figure 4.5: Projected muon spatial distribution along the x (right) and y (left) axis, produced by an 11 GeV electron beam interacting with the Hall-A BD sampled on a 1 m^2 flux detector downstream of the concrete vault enclosing the beam dump. The sigma values for both projections are approximately 25 cm.

BDX passive shielding design

A study was conducted to develop a passive shielding for the BDX detector to address the potential muon beam-on background that could lead to false positive signals. This study mirrors an earlier effort made during its proposal stage [98]. The earlier configuration is both prohibitively costly and overly complex to implement, so this study aims at finding new and cheaper solutions.

The first step in designing the shielding consisted of estimating the overall muon spectrum coming from the BD towards the chosen detector's location. Thus, muons were sampled on the red oval surface surrounding the BD in Figure 3.7, and their overall spectrum is presented in Figure 4.6. This spectrum, which shows values of p_μ up to 10.4 GeV, was obtained by performing multiple simulations with increasing energy cuts and subsequently merging the spectra with appropriate normalization. This method was effective in reducing the overall simulation time. Approximately 10^8 EOT were used to simulate the muons up to 9.75 GeV and approximately 2×10^{11} for the rest of the spectra.

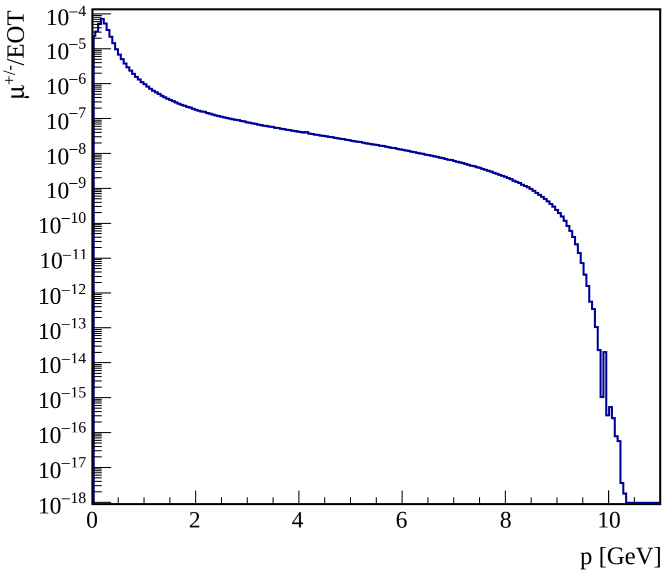

Figure 4.6: Muon momentum distribution produced by an 11 GeV electron beam interacting with the Hall-A BD. The fluctuations at the end of the spectra are a combination of two factors: relatively low statistics and high biasing factors.

Despite using the multiple-energy-cut technique to estimate the yield of higher-energy muons per EOT, the overall statistics at the spectrum's end remain relatively low. This suggests that either more extensive simulations are needed or an alternative method should be considered. Additionally, the results exhibit fluctuations near the 10 GeV threshold due to high biasing factors.

Given that the "brute force" approach of simulating an increasing number of particles is currently impractical due to the extensive simulation time required—potentially several months—which would monopolize computational resources, an alternative approach was considered. The studies discussed herein aim to determine an upper limit for the potential muon background arriving at the detector given a specific shielding configuration.

The following method was used to obtain an upper limit on the number of muons per year entering the detector. An electron beam is initially directed towards the BD to generate high-energy muons. This is achieved using the technique outlined in the previous paragraph. Then, muons are sampled around the dump and analyzed. After, a simulation is performed considering an 11 GeV muon beam originating from the end of the BD. The properties of this beam are inferred from the high-energy muons sampled in the first step. Finally, the results are normalized to the integrated value of the last filled bin of the spectra shown in Figure 4.6, which corresponds to a value of $10^{-18}\mu/\text{EOT}$. Both simulations utilized the same FLUKA options and energy cuts described in subsection 3.2.3. The simulation using a source muon beam did not utilize the "lead particle" biasing option. Table 4.1 summarise the muon-beam properties obtained using the described process.

Beam	
Primary particle	μ 50% $\overline{\mu}$ 50%
Momentum	11 GeV
Starting position	BD's end
Distribution	Gaussian $\sigma_x = \sigma_y = 0.8$ cm $\overline{x} = \overline{y} = 0$ cm
Beam divergence	5.7 mrad
Normalization factor	10^{-18}

Table 4.1: Muon beam properties used in the simulations.

Two shielding configurations have been explored using the defined 11 GeV muon beam. The first configuration involves a lead wall at the end of the concrete tunnel housing the BD, with additional lead placed in the forward direction right before the detector along the beam axis. The second configuration utilizes a several-meter-long lead wall in the forward direction before the detector. The side cross-sections of the two geometries inside the FLAIR geometry viewer are shown in Figure 4.7.

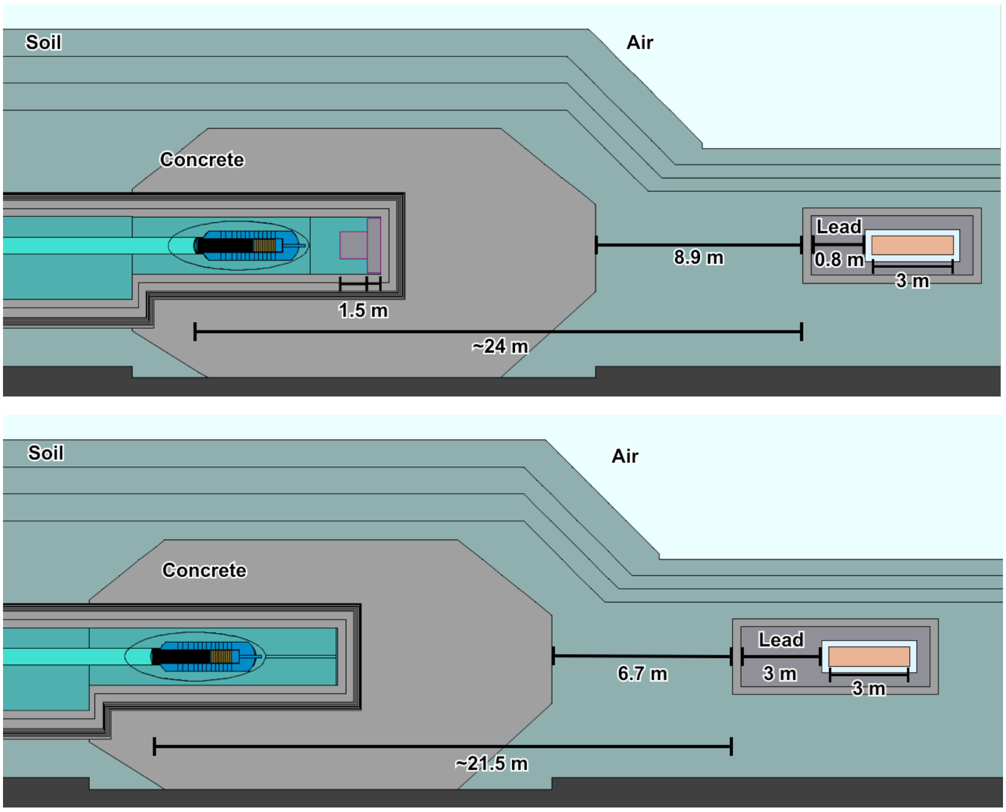

Figure 4.7: Side cross-section of the two shielding configurations from FLAIR geometry viewer. Top: Shielding configuration 1. This design considers a total length of 1.5 m of lead inside the BD's tunnel. The lead is arranged so that there is more lead near the beam-axis center to address the fact that higher-energy muons tend to be produced in the forward direction. Moreover, 0.8 m of lead are placed before the BDX's detector and 0.25 m on each side to attenuate the effect of muons coming from the side due to multiple scattering. Bottom: Shielding configuration 2. This design considers 3 m of lead right before the detector and 0.25 m on each side.

The first design offers the advantage of better mitigating the effects of muons produced at large angles, which could reach the BDX detector from its sides through multiple scattering and utilize less overall lead. However, constructing this structure within the BD tunnel could expose workers to high radiation levels. In Table 4.2, the main elements of this configuration are summarised.

Conf. 1	**Dimensions** $(x,y,z)[cm]$	**Material**
Detector	$70,70,300$	CsI
Air gap	$25,25,25$ around detector	Air
Shielding	Block 1: $50,50,100$ after BD Block 2: $100,100,50$ after Block 1 Block 3: $220,220,80$ before detector 50 cm all around	Lead
Housing walls	$25,25,25$ around shielding	Concrete

Table 4.2: Summary of the elements used in the first configuration of the shielding for the BDX experiment. Dimensions and materials are reported.

The second design, although significantly safer to construct, requires a more significant amount of lead. Additionally, it will need extensive dirt removal to accommodate it. Both factors will consequently increase the overall cost of the experiment. In Table 4.3, the main elements of this configuration are summarised.

Conf. 2	**Dimensions** $(x,y,z)[cm]$	**Material**
Detector	$70,70,300$	CsI
Air gap	$25,25,25$ around detector	Air
Shielding	$220,220,300$ before detector 50 cm all around	Lead
Housing walls	$25,25,25$ around shielding	Concrete

Table 4.3: Summary of the elements used in the second shielding configuration for the BDX experiment. Dimensions and materials are reported.

Over a year of beam time hitting the BD, equivalent to approximately 10^{22} EOT, the estimated number of muons entering the detector was calculated for both configurations. For the first configuration, approximately 230 $\mu/year$, while for the second configuration, roughly 170 $\mu/year$. In Table 4.4, the results are summarised.

	Flux $[\mu/year]$	**Lead** [t]
Conf. 1	230	215
Conf. 2	170	327

Table 4.4: Summary table of the total number of muon entering BDX's detector for each configuration.

Although some muons can reach the detector in both configurations, their effect can be mitigated using an active veto system. This system detects anti-coincidence in the signals, effectively identifying and excluding the unwanted muon hits. Doing so ensures that only the relevant data is recorded, thereby improving the accuracy and reliability of the experiment. The first estimate for such a system suggests that it can shield muons in the order of a few thousand.

Therefore, by integrating passive and active shielding for the muons, the BDX experiment can effectively minimize muon interference on the LDM signals while optimizing budgetary constraints, ensuring a more cost-effective implementation.

4.1.2 22 GeV Electron Beam

Because of the future CEBAF 22 GeV upgrade, similar simulations accounting for a total of $\sim 10^8$ EOT were performed assuming a 22 GeV primary electron beam. The resulting muon energy distribution at the end of the concrete vault around the BD, on a 1 m^2 surface (corresponding to a smaller portion of the green thick line in Figure 3.7) is shown in Figure 4.8. Muons from the 22 GeV electron beam are represented with a red line, while muons from the 11 GeV electron beam are represented with a blue line.

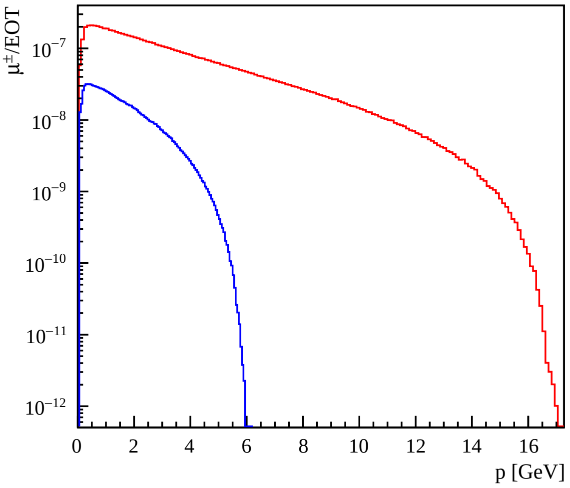

Figure 4.8: Muon momentum distributions produced by an 11 GeV (blue line) and 22 GeV (red line) CEBAF electron beam interacting with Hall-A BD.

The spectrum remains Bremsstrahlung-like, similar to the 11 GeV case, but it covers an extended energy range (up to ~16 GeV) with an almost ×8 yield. The spatial distribution shown in Figure 4.9 (left) results to be more forward-peaked with the majority of muons lying on a narrower $\sim 40 \times 40$ cm^2 area. Similarly, the plot of the correlation between direction and momentum shown in Figure 4.9 (right) remarks the fact that higher-energy muons are produced near the beam-axis.

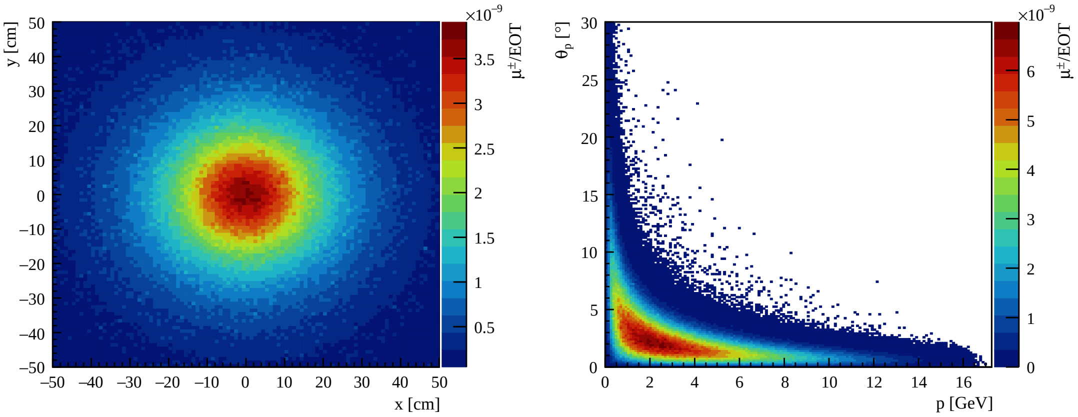

Figure 4.9: Left: muon spatial distribution produced by a 22 GeV electron beam interacting with the Hall-A BD sampled on a 1 m^2 flux detector downstream of the concrete vault enclosing the beam dump. Approximately 50% of all the muons cross the flux detector within an area of roughly 40 × 40 cm^2. Right: muon direction versus momentum. This plot shows that higher-energy muons are more forward-peaked compared to the 11 GeV case.

Similarly to the 11 GeV case, the muon spatial distribution was projected along the x and y-axis and fitted with a Gaussian function to estimate the muon beam size at the exit of the concrete vault. The plot in Figure 4.10 shows that the sigma values for both projections are approximately 20 cm.

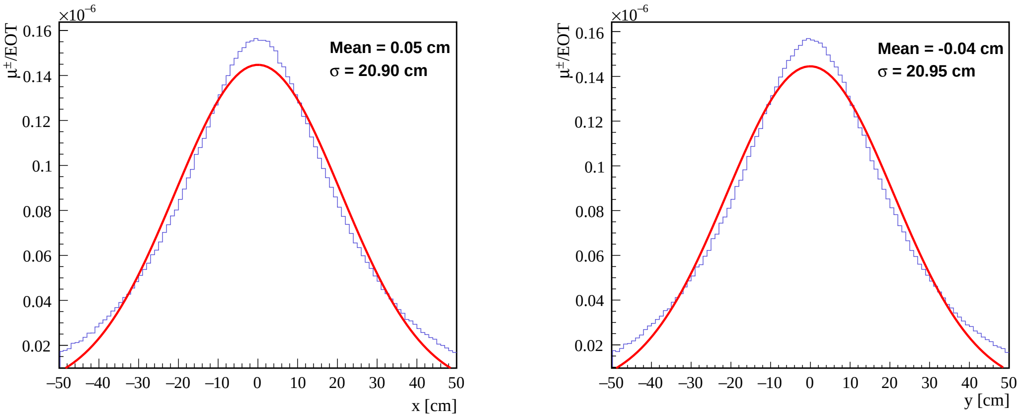

Figure 4.10: Projected muon spatial distribution along the x (right) and y (left) axis, produced by a 22 GeV electron beam interacting with the Hall-A BD sampled on a 1 m^2 flux detector downstream of the concrete vault enclosing the beam dump. The sigma values for both projections are approximately 20 cm

Finally, the main characteristics of muon beams produced by the interaction, respectively, of 11 GeV and 22 GeV CEBAF electron beam with the Hall-A BD are summarized in Table 4.5.

Beam energy	**Flux** ($\mu^{\pm}$/ **EOT**)		σ_x **(cm)**	σ_y **(cm)**
	100×100 **m**^{2}	25×25 **m**^{2}		
11 GeV	9.8×10^{-7}	1.5×10^{-7}	27.25	26.97
22 GeV	7.6×10^{-6}	1.9×10^{-6}	20.90	20.95

Table 4.5: Summary table of Hall-A secondary muon beam features.

In summary, the simulations for the 11 and 22 GeV cases demonstrated that the muon beam is intense and well-focused, even after traversing the BD's concrete vault. This indicates its suitability for experimental applications and suggests that its performance could be further enhanced by constructing additional facilities.

4.2 Secondary LDM beam

The following sections present the characteristics of a hypothetical dark scalar S beam produced respectively by the interaction of a primary 11 GeV and 22 GeV electron beam with the Hall-A BD. For the former, a realistic background evaluation was possible based on data collected at 10 GeV electron beam in the BDX-MINI experiment [104]. This provided a solid ground to realistically evaluate the expected sensitivity of an experiment (sBDX-MINI), which uses a reduced version of the BDX detector [92]. Results are reported in subsection 4.2.3. The experimental sensitivity was not evaluated in the 22 GeV electron beam case since a realistic background model was not available.

4.2.1 11 GeV electron beam

To characterize the hypothetical dark scalar beam, $\sim 10^9 - 10^{11}$ muons were simulated using the biasing procedure described in subsection 3.2.3. Simulations were performed assuming a fixed coupling constant $g_\mu = 3.87 \times 10^{-4}$ and m_S in the range 25 MeV - 210 MeV. A further bias factor of 10^7 was introduced in FLUKA simulations to keep the computational time reasonable.

Figure 4.11 shows results for the dark scalar beam obtained with an 11 GeV primary electron beam. The top panel shows the S spatial distribution on a sampling plane located 20 m downstream of the beam dump. The plot on the left was obtained assuming a dark scalar mass of m_S = 50 MeV, while the plot on the right refers to m_S = 180 MeV. The difference in the S beam spot size is due to the different fraction of energy transferred from the muon to the radiated S that increases for larger m_S (more energetic S corresponds to a smaller spatial spread).

The S energy spectrum is shown, for different m_S, on the top-left panel of Figure 4.12. The right column shows the S angular distribution with respect to the primary beam direction. All distributions are normalized to the number of S per EOT. The energy distribution for light scalar shows a peak at low energy since for heavier scalar the out-going S takes a larger fraction of the muon energy. The kinematic of the produced S strongly depends on its mass: heavy S are mostly produced in the forward direction, while lighter S have a wider angular distribution.

4.2.2 22 GeV electron beam

Simulations were performed using the same bias factor and coupling g_μ used for the 11 GeV electron beam case. The resulting beam spot size, energy, and angular distributions are shown in the bottom panels of Figure 4.11 and Figure 4.12, respectively. They show a behavior similar to the 11 GeV case, with a more focused dark beam spot that

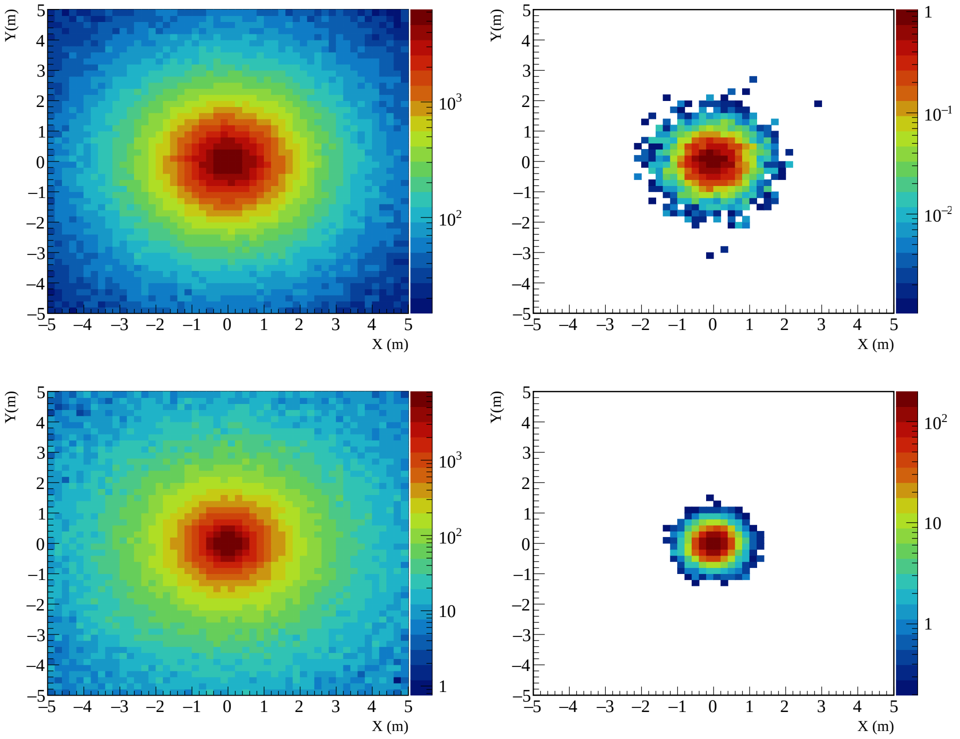

Figure 4.11: Spatial distributions of S sampled 20 m downstream of the beam dump. The top (bottom) row refers to an S beam generated by the 11 GeV (22 GeV) CEBAF electron beam. The beam spot size refers to m_S = 50 MeV (left) and m_S = 180 MeV (right).

covers an extended energy range. The S yield increases by a factor of 3-10, depending on the scalar mass.

Beam Energy (GeV)	m_S = 50 MeV		m_S = 180 MeV	
	S/EOT	σ (m)	S/EOT	σ (m)
11	5.27×10^{-15}	1.556	1.32×10^{-16}	0.488
22	1.90×10^{-14}	1.22	1.44×10^{-15}	0.304

Table 4.6: Summary of JLab scalar dark matter beam features.

Finally, Table 4.6 summarizes the expected S yield per EOT and beam spot size, sampled in a plane located 20 m downstream of the beam dump for an 11 and 22 GeV beam, and the two values of m_S.

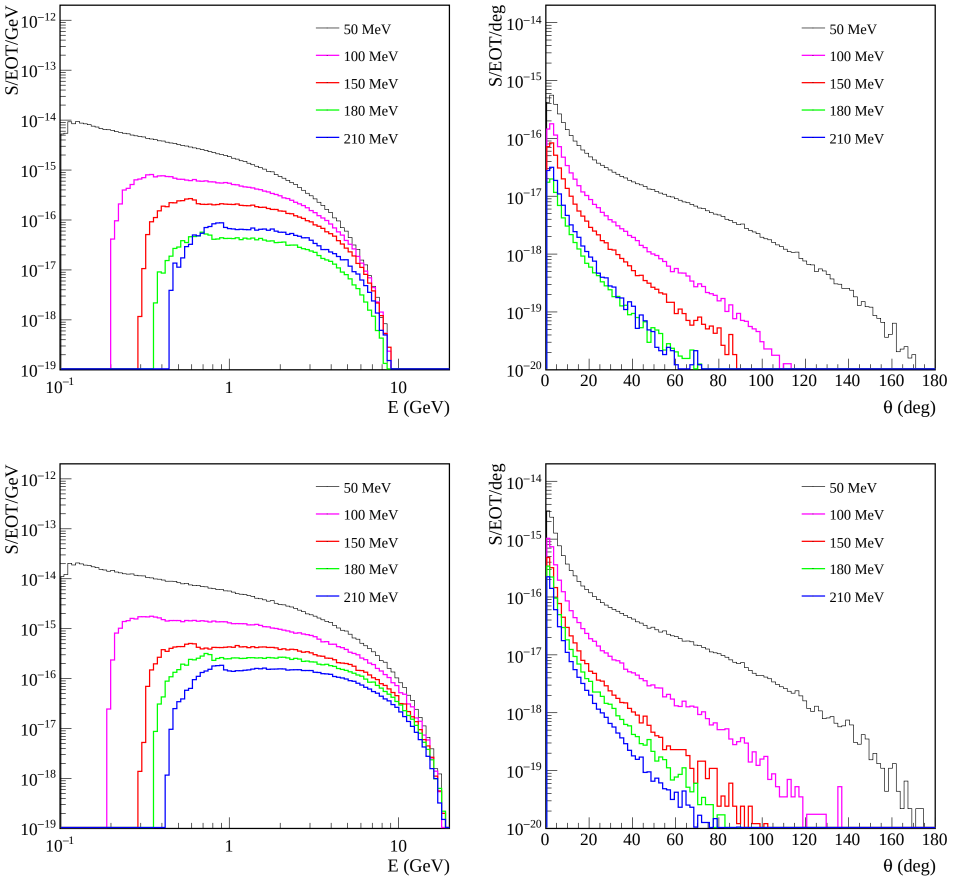

Figure 4.12: Energy (left) and angular (right) distributions of the dark scalar S for different masses. Results are shown for a primary 11 GeV electron beam (top) and 22 GeV (bottom).

4.2.3 Discovery potential of *s*BDX-MINI experiment

The two pipes already installed downstream of Hall-A BD could host a new experiment searching for the dark scalar particle S: *s*BDX-MINI. The same infrastructure was used for the BDX-MINI experiment [104]. In this section, the sensitivity of a BDX-MINI-like experiment searching for S in the visible decay mode ($S \to \gamma\gamma$) with both gammas detected was explored.

The sBDX-MINI would make use of CEBAF 11 GeV e$^-$ beam hitting the Hall-A BD running for about 1 yr with currents up to 75 μA (corresponding to an accumulated charge of 10^{22} EOT).

A detector with a layout similar to BDX-MINI, with an almost cylindrical electromagnetic calorimeter of radius 8 cm surrounded by a multi layer veto system was assumed. To compensate for the limited pipe size (10"), a 2 m vertical long detector, roughly corresponding to 4 BDX-MINI detectors stacked was assumed. So, with the current JLab setup, some muons produced by the 11 GeV beam interaction with the BD will reach the two pipes. The detector was assumed to be located in the farthest well to reduce this background.

To evaluate the 90% C.L. exclusion limit in case of a null result, the formula $S^{UP} = 2.3 + 1.4\sqrt{B}$ [98], where S^{UP} is the upper limit on the number of signal events and B is the total number of background events, was used. The expected background was conservatively estimated using BDX-MINI beam-on (at 10 GeV e- beam) and beam-off data [104] scaled for the volume of the *s*BDX-MINI detector. A background yield of $\sim 0.5 \times 10^{-12}$ μ/EOT is estimated requiring an energy threshold of 300 MeV. The upper limit on the number of signal events was then translated into an exclusion limit for the g_μ coupling constant. The exclusion limit, as a function of the S mass is shown in Figure 4.13. Although *s*BDX-MINI does not test unexplored regions in the g_μ vs. m_S parameter space, the sensitivity that could be achieved with such a limited-size detector suggests that a full version of the experiment (*s*BDX) would have a significant sensitivity to a dark scalar particle.

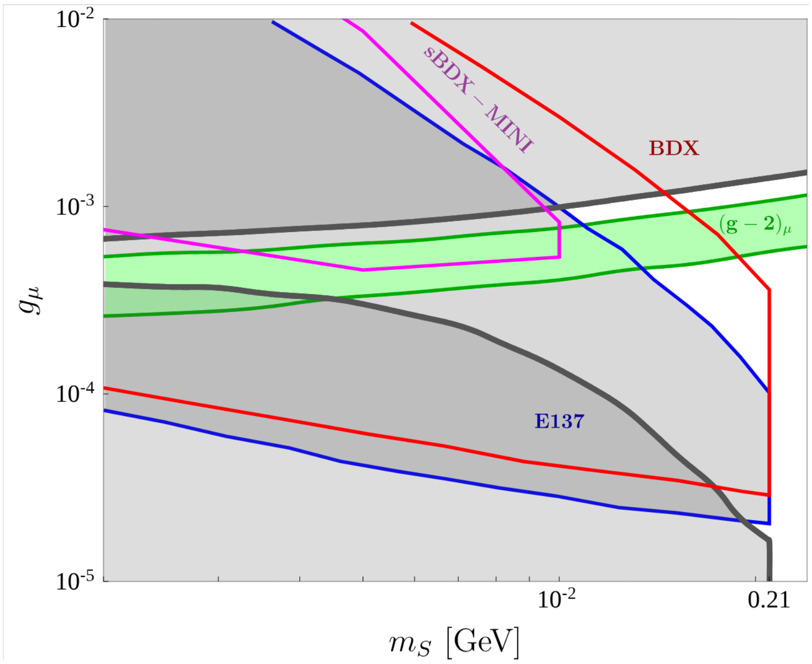

Figure 4.13: 90% C.L. projection of the exclusion limit of *s*BDX-MINI. E137 exclusion limit (blue) and projection for BDX (red) sensitivity [61] are also reported. The gray area represents already excluded regions. The green band depicts the parameter combinations that could explain the $(g-2)_\mu$ discrepancy. The sharp limit at ~ 0.21 GeV is related to the opening of $S \rightarrow \mu\mu$ competing decay channel.

Chapter 5

JLab's Hall-A Secondary Neutrino Beam

This chapter will explore the possibility of producing an intense beam of neutrinos using the CEBAF electron beam impinging on the Hall-A BD. Detailed results of Monte-Carlo simulation of neutrinos produced by the interaction of CEBAF 11 GeV e^-–beam with Hall-A BD are shown in subsection 5.1.1. While in subsection 5.1.2, results of Montecarlo simulations using a 22 GeV electron beam for the coming CEBAF upgrade will be presented. The on-axis and the off-axis fluxes will be presented. Then, in section 5.2, a study on a possible CEνNS experiment at JLab is discussed. Here, the beam-related neutron background is evaluated using different methodologies.

5.1 Hall-A Secondary Neutrino Beam

The interaction of the CEBAF electron beam and the Hall-A BD make the BD also an intense source of isotropically emitted neutrinos. Similarly to the one obtained from spallation sources, they present an energy spectrum depending on the decay that can be summarized as follows:

- $\pi^+ \to \mu^+ + \nu_\mu$, $E_\nu \sim 29.8$ MeV, almost monochromatic;
- $\mu^+ \to \overline{\nu}_\mu + \nu_e + e^+$, E_ν in the range 0 - 52.8 MeV;
- $K^+ \to \mu^+ + \nu_\mu$, $E_\nu \sim 236$ MeV, almost monochromatic.

Different biasing techniques and energy cuts were employed to achieve better statistics and faster convergence of the results for both 11 and 22 GeV cases. The simulation framework described in subsection 3.2.3 and the options listed in section 4.1 were used. Custom FLUKA user routines were utilized to export the results directly into ROOT files, in conjunction with `mgdraw.f` user routine to dump all particle properties into a TTree.

5.1.1 11 GeV electron beam

The results presented in this section are derived from multiple simulations conducted on both the Jefferson Laboratory and CNAF computing farms. The simulations account for a total $\sim 5 \times 10^8$ primary electrons impinging on the Hall-A BD with momentum $p_{e^-} = 11$ GeV.

Figure 5.1 presents the resulting neutrino energy spectrum showing the different neutrino species using multiple colors, sampled on the red surface around the dump in subsection 3.2.3. As anticipated, a peak around 29.8 MeV and another peak 236 MeV related to π and K DAR are visible over a smooth background due to the muon decay and DIF events. The peak at 70 MeV has been tracked back to pion decay in electron and electronic neutrino. As expected, it is suppressed by four orders of magnitude with respect to the dominant allowed decay $\pi^+ \to \mu^+ + \nu_\mu$.

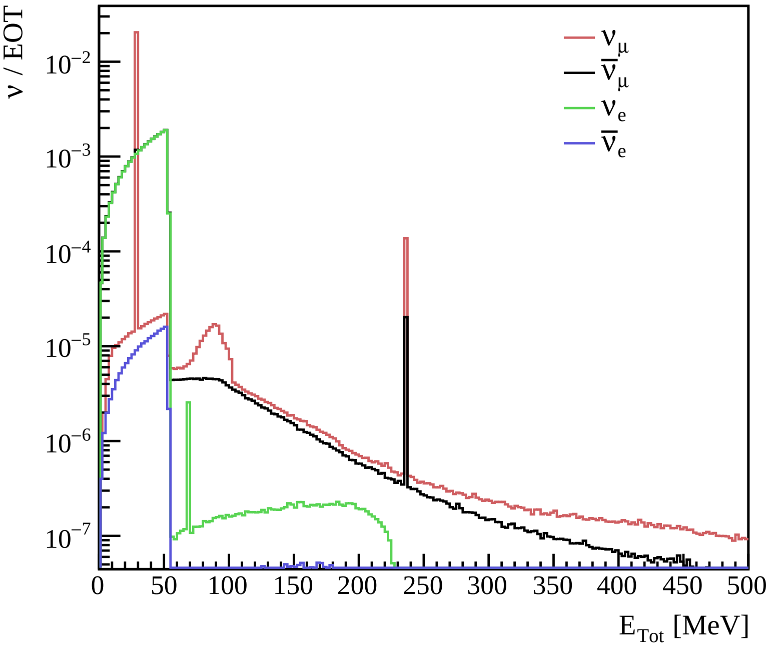

Figure 5.1: Neutrino energy spectrum produced by the interaction of the CEBAF 11 GeV e^- beam with the Hall-A BD. Each color corresponds to a different neutrino species, as the legend reports.

The characteristics of the neutrino flux produced along the primary electron beam direction (on-ìaxis) and perpendicular to it (off-axis) were studied. The on-axis flux was computed on a 1 m^2 flux detector located at the end of the concrete vault in the forward direction (green thick line in Figure 3.7). The off-axis flux was computed on a 1 m^2 flux detector located approximately 10 m above the dump at ground level (orange surface in Figure 3.7).

Results show that the off-axis ν energy spectrum (see Figure 5.2-left panel) is compatible with the spectrum of a DAR source. The overall neutrino flux in the energy range 0-100 MeV is $\sim 6.6 \times 10^{-5}$ ν/EOT, corresponding to 99% of the spectrum. Therefore, for an accumulated charge of 10^{22} EOT per year, an intense flux of $\sim 10^{18}$ ν, comparable to the integrated flux of the flagship DAR-neutrino facility SNS@Oak Ridge National Lab [105], is expected.

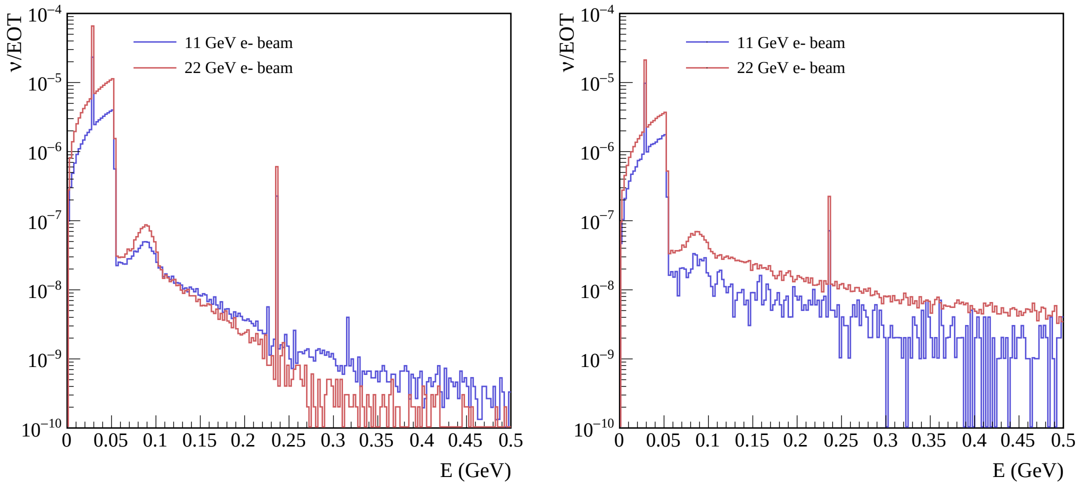

Figure 5.2: Energy distribution of off-axis (right) and on-axis (left) neutrinos produced by the interaction of 11 GeV (blue) and 22 GeV (red) CEBAF electron beams with the Hall-A BD.

Figure 5.2 right-panel shows the energy distribution of on–axis neutrinos. Even if the DAR contribution is dominant, a tiny but not negligible part of the spectrum shows energies greater than 100 MeV. The resulting on-axis neutrino flux in the energy range 0-500 MeV is $\sim 2.9 \times 10^{-5}$ ν/EOT, with the DAR part corresponding to ∼96% of the overall yield.

5.1.2 22 GeV electron beam

Similarly to the muon case, the neutrino flux produced by the interaction of a primary 22 GeV e^-–beam with Hall–A BD was evalueted. Figure 5.2 compares the on/off–axis neutrino energy distributions, produced by an 11 GeV and 22 GeV electron beam. They show a similar shape with a yield difference of about a factor of 2. More precisely, the results of simulations show an overall off-axis flux of $\sim 1.9 \times 10^{-4} \nu/$ EOT while an on-axis flux of $6.3 \times 10^{-5} \nu/$ EOT in the energy range 0-500 MeV. Table 5.1 summarise the neutrino fluxes characteristics.

Beam energy	**Off–axis flux** $(\nu/\,\mathrm{EOT})$	**On–axis flux** $(\nu/\,\mathrm{EOT})$
11 GeV	6.7×10^{-5}	2.9×10^{-5}
22 GeV	1.9×10^{-4}	6.3×10^{-5}

Table 5.1: Summary of JLab secondary neutrino beam features. Yields are obtained by integrating the neutrino flux in the energy range 0-500 MeV.

5.2 CEνNS at JLab

Based on the neutrino flux estimates from the simulations presented in section 5.1, the feasibility of conducting a CEνNS experiment at JLab will be explored. Within a year of beam operation, equivalent to 10^{22} EOT, the equivalent neutrino off-axis flux will be approximately $10^{18}\nu/year$ for the 11 GeV case, and $2\times10^{18}\nu/year$ for the 22 GeV case. Compared to similar proposed experiments at proton-beam facilities (for example, the νBDX-drift experiment at FNAL [106], the JLab neutrino flux is several orders of magnitude higher, making it an attractive option for this type of experiment.

When conducting a CEνNS experiment, it is essential to meticulously account for and to reduce background events that could mimic the signal events as much as possible. Charged particles, despite their ability to penetrate materials, are not a major concern as they can be identified and rejected. However, neutral particles, such as photons and neutrons from the neutrino source, as well as those due to cosmic background, must be effectively shielded to avoid generating signals that mimic CEνNS events.

The first step in designing such an experiment is selecting an optimal location for the detector that considers potential background noise. Placing the detector above ground allows the material between the detector and the background source to partially shield photons and neutrons. However, low-energy neutrons can travel significant distances, necessitating a precise shielding and veto design to minimize their impact on detected events. For this reason, several studies were performed to determine the background neutrons originating from the BD and cosmic rays.

5.2.1 Beam-related neutron background estimation techniques

Electrons impinging on the BD lose energy through bremsstrahlung creating showers of charged particles that can subsequently produce neutrons with a wide range of very complex physical processes [107]. FLUKA was chosen as the preferred tool to simulate these processes and evaluate the neutrons originating from the BD. The simulation framework described in subsection 3.2.3 was utilized alongside several biasing techniques. In such simulations, the conventional "brute force" method of incrementally simulating more primaries proved inefficient. This inefficiency arises from the significant absorption of neutrons during their propagation, necessitating the generation and propagation of many neutrons through the geometry to achieve the desired precision. However, this approach results in excessively long simulation times. Therefore, alternative methods were considered to reduce the overall time required to generate and propagate low-energy neutrons through the geometry to the point of interest.

The resampling method

The first method involved simulating $\sim 10^8$ primaries of an 11 GeV electron beam impacting the BD and sampling neutrons on a nearby surface, red oval surface of Figure 3.7. To significantly reduce simulation time, particles were stopped immediately after this step.

Next, the sampled neutrons were used with ROOT to create a multi-dimensional distribution of the phase-space parameters needed for the `source_newgen` user routine (detailed in subsection 2.3.4). These parameters include particle identity code, three-vector cosine directions, three-vector position, and three-vector momentum.

Using ROOT, a cumulative function of the multi-dimensional distribution was computed. Particles were then extracted and printed in a source file. This source file was fed into FLUKA to propagate the neutrons from the BD. This process was repeated for a large amount of FLUKA runs to accumulate higher statistics.

This entire procedure allows to bypass the simulation of electromagnetic cascades and focus solely on neutron propagation. The process was reiterated multiple times, each time sampling neutrons at increasing distances from the BD until sufficient statistics were gathered at the points of interest. In Figure 5.3, a schematic diagram represents this method.

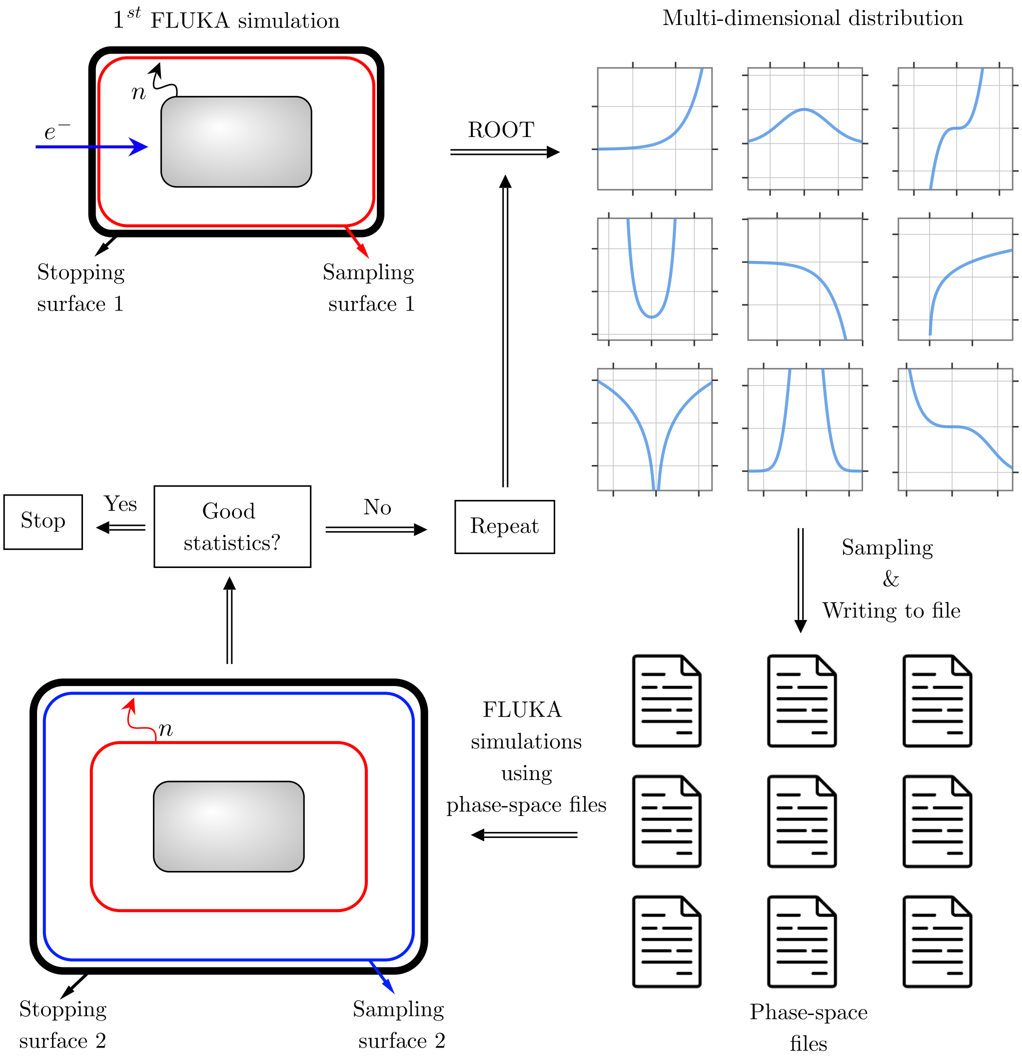

Figure 5.3: Diagram illustrating the resampling method to enhance neutron statistics at long distances from the BD. *1. Upper Left Corner*: The electron beam interacts with the BD, and neutrons are sampled on the red surface. *2. Upper Right Corner*: A multi-dimensional distribution of the sampled neutrons is created using ROOT. *3. Lower Right Corner*: The multi-dimensional distribution is sampled to obtain neutron parameters for use as a source. *4. Lower Left Corner*: The re-sampled neutrons are propagated from the red surface to the blue surface, where they are sampled. If the desired statistics are achieved at this point, the process stops. Otherwise, it repeats from the second step.

Resampling with machine learning

Machine learning involves using algorithms and statistical models to enable computers to perform tasks without explicit instructions. These models can identify patterns and make predictions or decisions by training on data.

The resampling method was also performed using machine learning techniques. Instead of using the ROOT framework to create a multi-dimensional distribution from which to extract the new source particle parameters, the distribution was fed to a learning network known as a "normalizing flow", great at modeling complex conditional densities [108, 109]. This network was implemented using the `PyTorch` library and the `nflows` package. The code for creating the normalizing flow involves defining a series of transformations, including Masked Affine Autoregressive Transforms and Reverse Permutations, which are combined into a Composite Transform. The base distribution is a Conditional Diagonal Normal distribution, conditioned on the context provided by the data. The network was then trained to produce the source particle parameters when requested.

Initially in ROOT file format, the data was fed to the network leveraging the pyROOT interface, allowing seamless integration between ROOT and Python. The advantages of this method lie in its speed and memory efficiency, as it leverages GPU cores instead of CPU ones. This results in faster computations and better handling of large datasets. The procedure of extracting the particle's parameters from the trained network is much faster than the resampling method described in the previous section, enabling a faster pipeline for the simulation. In Figure 5.4, it is possible to see the plots of the various parameters needed for the simulation fed to the network (blue line) and the newly extracted ones (red line).

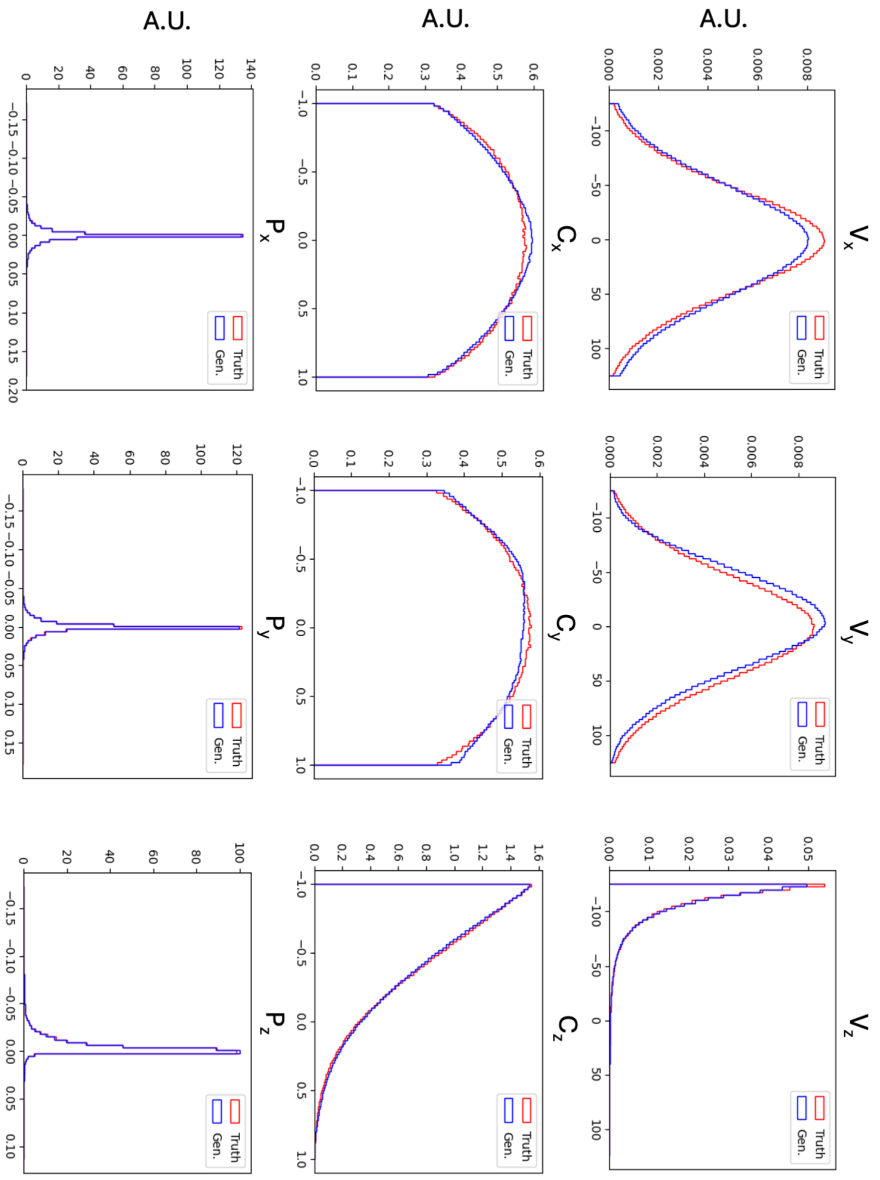

Figure 5.4: Parameters needed for the simulation fed to the network (red line) and the newly extracted ones (blue line).

The biasing attenuation compensation method

This method creates a custom implementation of the surface-splitting biasing technique. This was achieved by modifying the `usimbs.f` routine to compensate for the neutron attenuation in specific materials and directions.

The first step of this process required the simulation and propagation of a sufficient number of neutrons from the electron beam striking the BD within the concrete. Then, neutrons were sampled on several 1 m^2 surfaces on top of the dump every 0.5 m and their integrated flux was calculated in terms of neutrons per EOT. Next, the logarithmic of the fluxes at each surface was calculated and plotted against the position of the surface on the y-axis and fitted with a linear function to obtain the attenuation factor i. This procedure was performed for neutrons with kinetic energy above and below 20 MeV to obtain the appropriate attenuation factor for each case.

After, the `usimbs.f` routine was implemented in such a way as to act only on neutrons inside the concrete and moving in the positive y direction. The impact on simulation time was minimized by restricting the particles and direction to which the bias was applied. Then, the multiplication factor of the neutrons moving inside the concrete was set equal to:

$$f = k_1 e^{i*k_2}$$

Optimal values for k_1 and k_2, in terms of neutron multiplication versus computing time, were determined through trial and error to be between 1.2–1.5 and 2–5, respectively, depending on the material (for example, for neutrons moving inside lead $k_1 = 1.5$ and $k_2 = 5$ were used). The multiplication factor f was adjusted based on the neutrons' kinetic energy, with different values set for energies above and below 20 MeV, according to the determined attenuation factors i.

Finally, the simulation was rerun with the new biasing settings, confirming that the statistics at the point of interest were significantly higher without substantially increasing the simulation time. The entire process was then repeated to account for the attenuation of neutrons within the dirt above the concrete and lead before reaching the detector.

5.2.2 Beam-related neutron background estimation results

Having established the methodologies to estimate the neutron background originating from the BD, studies were conducted to determine the optimal position for the detector on the hill above the BD. This was done by evaluating the neutron background and neutrino flux ratio.

The neutrino and neutron fluxes were sampled on adjacent 1 m^2 surfaces atop the hill above the BD. Figure 5.5 illustrates the ratio of neutron to neutrino flux at various positions on the hill for neutrons with kinetic energy below 10 MeV without any form of shielding. The x-axis origin of the plot aligns with the starting point of the dump.

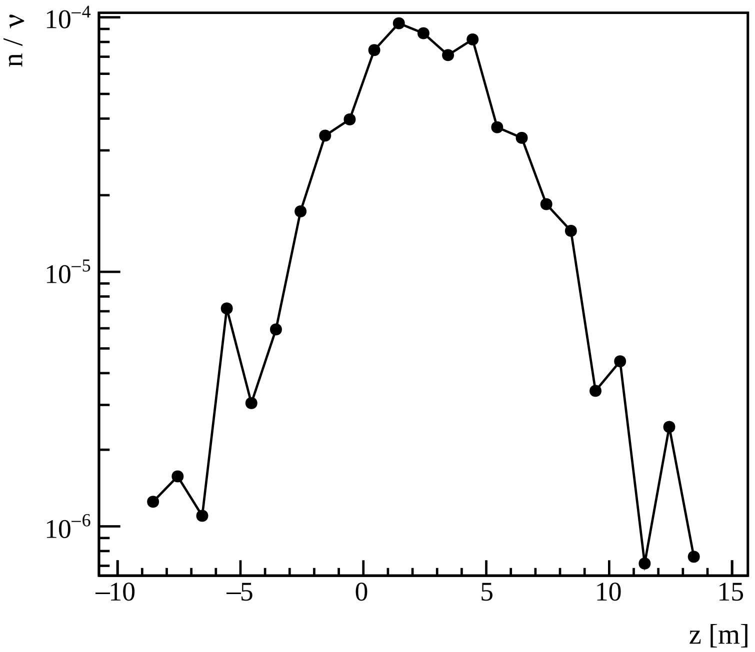

Figure 5.5: Ratio of neutron to neutrino flux sampled on 1 m^2 surfaces on the ground above the BD, moving from left to right across the hill. These surfaces are aligned with the center of the BD along the x-axis, while the plot's origin aligns with the starting position of the dump. As one moves to the sides of the hill, the ratio decreases, indicating a reduction in neutron flux.

From Figure 5.5, the optimal positions for the detector above the BD can be identified, with the most favorable locations being those most distant from the reference frame's origin. These positions maximize the material between the detector and the neutron source. Subsequent studies will focus on the position marked with a red dot and represented by the blue tick in Figure 3.7 as the best location for the detector.

After identifying the optimal location for the detector, the study shifted focus to designing passive shielding against background neutrons originating from the BD. Various configurations were tested using previously described techniques. As shown in Figure 5.6, a quantitative comparison of all shielding configurations was conducted. Initially, no shielding was used to measure the neutron flux at the detector location (S1), serving as a baseline for subsequent studies aimed at reducing neutron flux. Two configurations were tested to evaluate the effectiveness of combining lead and water in reducing the overall neutron flux. The first configuration (S2) involved a 1-meter thick layer of lead and a 1-meter thick layer of water covering the entire hill. The second configuration (S3) tested two 1-meter thick layers of lead and one 1-meter thick layer of water covering the whole hill. Although these configurations are not practical due to the large amount of material required, they provided valuable insights into the materials needed to reduce neutron background.

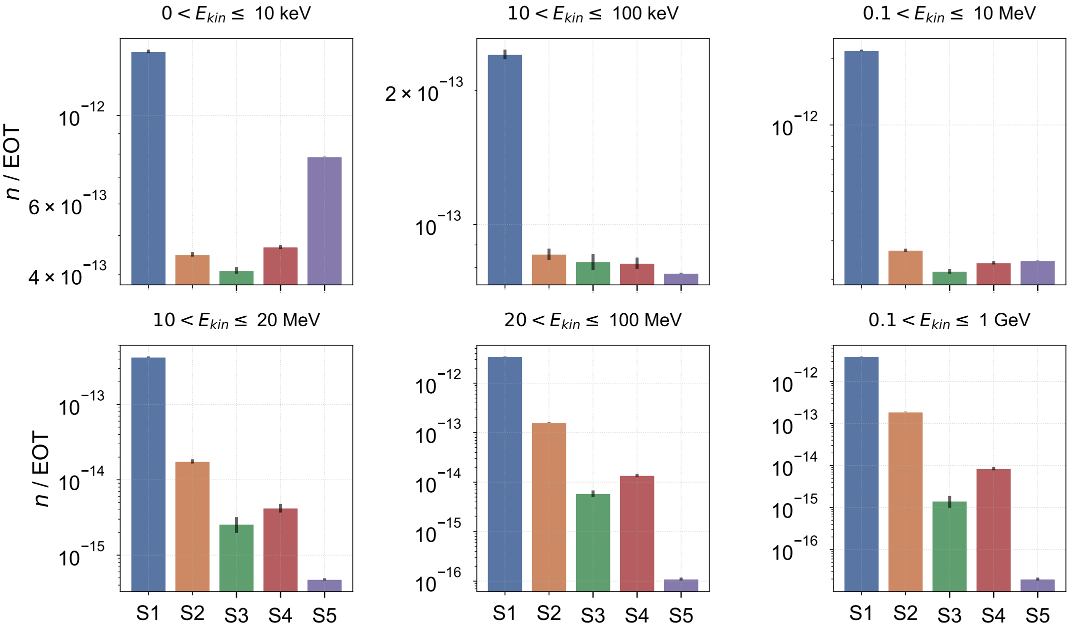

Figure 5.6: Comparison of neutron flux across different shielding configurations, represented by different colored bars, in various energy ranges. The figure reports the flux for the following configurations: no shielding (S1); a layer of lead and a layer of water, each 1 meter thick, covering the entire hill (S2); two layers of lead and one layer of water, each 1 meter thick, covering the entire hill (S3); three square layers, each measuring 4 × 4 meters and 1 meter thick, consisting of two layers of lead and one of water, placed directly above ground with the detector on top (S4). The most effective configuration (S5) features a similar setup with three layers of lead, where two layers are embedded in the ground, and the third layer is above ground level with the detector on top.

A more realistic configuration involved three square layers, each measuring 4×4 meters and 1 meter thick, consisting of two layers of lead and one of water. These layers were placed directly on the ground, with the detector positioned on top (S4). The most effective configuration, however, featured a similar setup with three layers of lead. In this arrangement, two layers were embedded in the ground, while the third layer was above ground with the detector on top (S5). The layers were arranged in a stair-step configuration to maximize the material between the BD and the detector. The S5 setup, illustrated in Figure 5.7, was the most effective at reducing neutrons in the range of interest, specifically between 0.1 and 10 MeV.

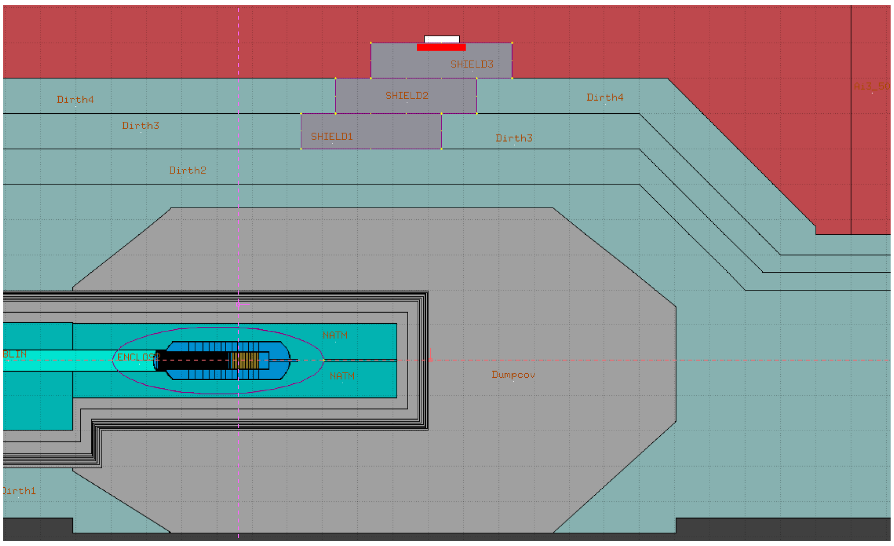

Figure 5.7: Side cross-section (to scale) of shielding configuration S5. The shielding consists of three layers of lead, each 1 meter thick, designed to protect the detector from neutrons originating from the BD. Two of these lead layers are embedded in the ground, while the third layer is positioned above ground. The detector, depicted as a white box, is on top of the above-ground lead layer. Neutrons are sampled at the red surface.

5.2.3 Cosmic rays related background

The Earth is continuously bombarded by high-energy particles known as cosmic rays. These particles are composed of roughly 89% protons, 10% helium ions, and 1% heavier nuclei, with energies reaching up to 1000 GeV. When these primary particles collide with air molecules, they often cause spallation, breaking into smaller nucleons. The neutrons produced by these cosmic rays can be detected on the ground, covering a wide energy range from thermal levels to several GeV. Neutrons penetrate deeper into our atmosphere compared to most electromagnetic components. As they travel, they interact with atmospheric nuclei, releasing additional particles.

For this reason, a detector placed on the ground also needs to be shielded against cosmic neutrons. Several studies were performed to find the best shielding configuration to lower the number of non-removable hits inside the detector (i.e., the hits that cannot be distinguished from CEνNS events) due to cosmic rays. These studies used GEANT4 because the detection and veto system pipelines were more straightforward to implement.

The final configuration, illustrated schematically in Figure 5.8, includes the shielding from beam-related neutrons as well as the one coming from cosmic rays. It consists of 5 cm of lead around the detector, 6 cm of scintillating veto surrounding the lead, 55 cm of lead placed above it, and an additional 5 cm of lead on the ground. This setup reduces the number of neutrons reaching the detector to 1.7×10^5 cosmic neutron hits per year and 2×10^4 beam-related neutron hits per year.

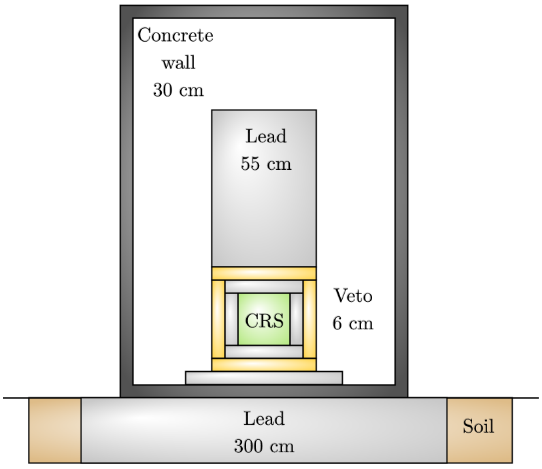

Figure 5.8: Final shielding configuration (not to scale) against beam-related and cosmic neutrons. The shielding consists of a 30 cm concrete wall (dark grey), 55 cm of lead above the detector (light grey), 5 cm of lead around the detector (grey), 6 cm of scintillating veto surrounding the lead (yellow), another 5 cm of lead below the veto, and 300 cm of lead below the concrete wall on the hill above the BD (brown). The crystals, either of CsI or PbWO, detecting the CEνNS events are labeled as "CRS" (green).

5.2.4 Physics sensitivity

Given the neutrino flux as a function of energy, it is possible to estimate the yield for a given target based on the minimum detectable recoil energy T_A. Two detector configurations were considered: one in which the detector is made of CsI crystals of density 4.51 g/cm^3, and one in which the doctors is made of $PbWO_4$ crystals of the density of 8.28 g/cm^3. The yield was calculated for a minimum detectable recoil energy $T_A = 5$ keV for both cases.

Figure 5.9 present the expected number of CEνNS events for the two configuration considered. Using CsI, the number of expected events in the detector is approximately 10^3 while using $PbWO_4$ crystals circa 10^4. While using $PbWO_4$ crystals yield an order of magnitude more events, the light output for these crystals is a whole order of magnitude less, thus rendering the detection process much more difficult.

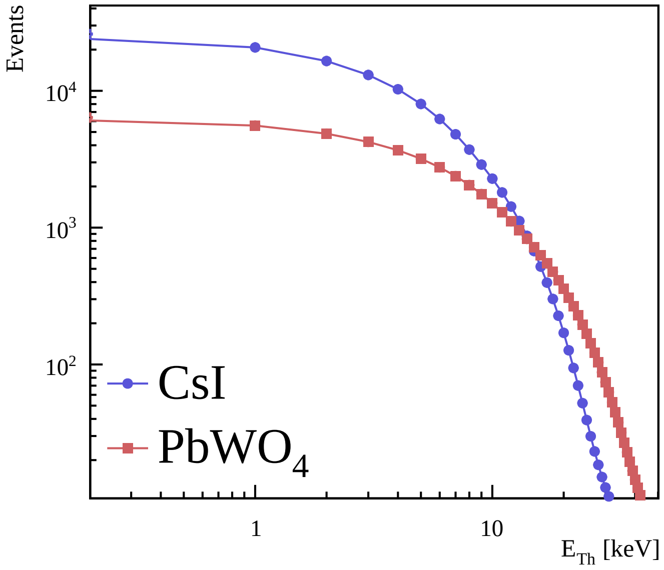

Figure 5.9: Yield of CEνNS events for a 1 m^3 detector made of CsI (blue) and $PbWO_4$ (red) crystals.

By analyzing the number of CEνNS events, it is possible to estimate the physics reach for extracting quantities such as the Weinberg angle. According to the method described in [106], the uncertainty in the extracted sine of the Weinberg angle is expected to be three times smaller with a CsI calorimeter and four times smaller with a PbWO4 calorimeter compared to the COHERENT results. Figure 5.10 shows the comparison of the sine of the Weinberg angle across several experiments. The νBDX estimation for a detector made of CsI crystals is highlighted in green.

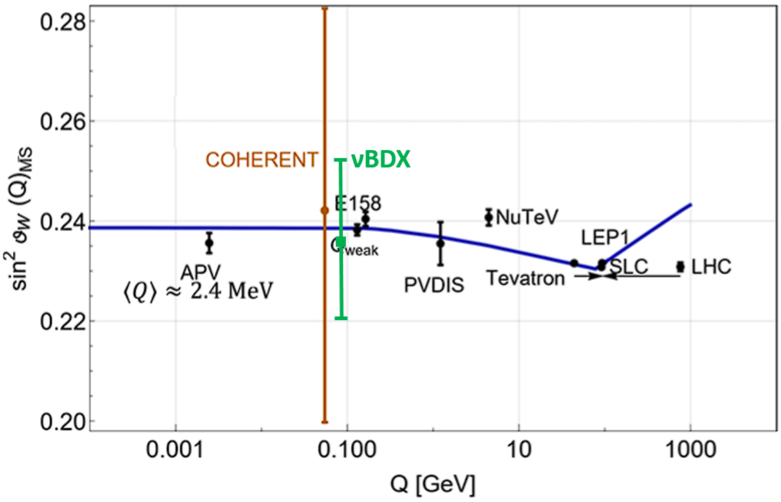

Figure 5.10: Comparison of the sine of the Weinberg angle across several experiments. The νBDX estimation for a detector made of CsI crystals is highlighted in green.

Chapter 6

JLab Hall-D Secondary Muon Beam

The CPS, originally designed to produce a photon beam, is capable of producing an intense muon beam. Research on the CPS muon beam has focused on two main areas: its characterization, described in section 6.1, and the feasibility of performing a missing momentum experiment, described in section 6.2. For the latter, the research involved a study on the resolution of the missing momentum using a minimal setup consisting of two dipoles to measure the momentum before and after the target and a simplified tracking algorithm explained in detail in Appendix A. Moreover, a study has been conducted to find a real magnet similar to those utilized in the simulations.

6.1 Secondary muon beam at the KLF-CPS facility

The processes that lead to the production of muons are similar to those described in subsection 1.1.2. Here, electrons are bent inside the CPS producing photons that subsequently either photoproduce pions and kaons that decay in muons or photoproduce a pair of anti-muon–muon. Radiated muons are strongly peaked in the forward direction with energy comparable to the primary beam energy and are emitted at small angles, while muons produced via decay-in-flight of photo-produced π's and K's show a lower energy spectrum and are emitted at larger angles.

Biasing techniques and *ad hoc* cuts were employed to improve simulation time and statistics:

- Mean free path biasing to enhance by 10^5 the production of high-energy muons in the dump.
- Mean free path biasing to enhance by 10^2 the photon-induced hadronic reactions.
- The "leading particle bias" was activated for electromagnetic processes.
- Importance-sampling by splitting was implemented.

- Particle transport threshold was fixed to 100 MeV for all particles.

Muons were sampled across several surfaces across the geometry using the `mgdraw.f` user routine as described in subsection 2.3.4. A custom implementation of the `source_newgen.f` user routine was used to generate muons for the conceptual tracking study.

The results presented in this section are based on several simulations performed on the Jefferson Laboratory computing farm. The simulations account for a total simulated $\sim 2 \times 10^8$ primary electrons sent inside the CPS with momentum $p_{e^-} = 12$ GeV.

The spatial distribution of the production vertexes of all the muons generated by the CPS along the yz-plane is shown in Figure 6.1, this plot represents the area enclosed by the yellow box in Figure 3.11. The plot reveals that the muons are produced in a few centimeters inside the CPS, precisely where the electron beam is deflected to generate photons.

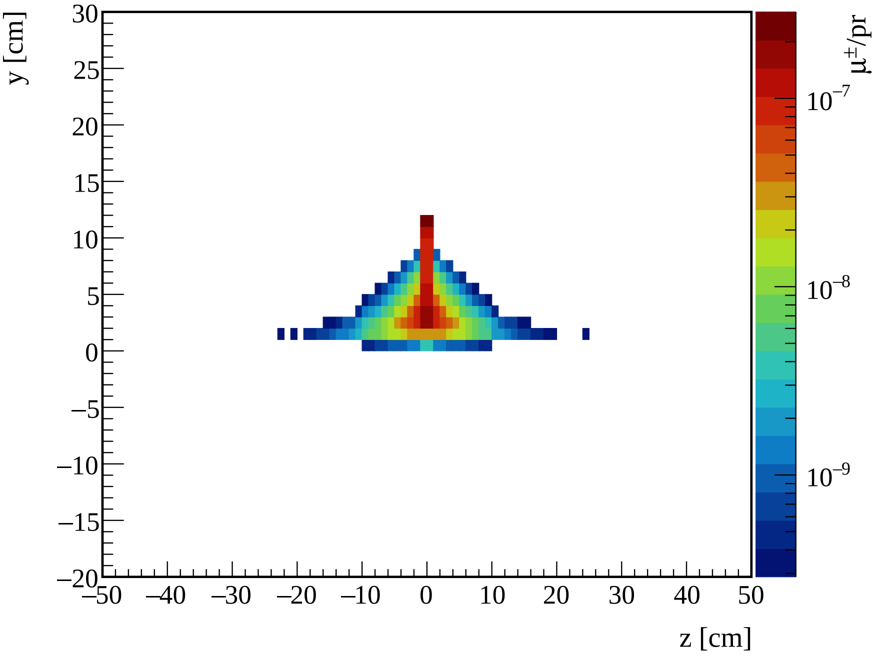

Figure 6.1: Muon production vertex inside the CPS.

The momentum spectrum of the muons produced by the CPS, as shown in Figure 6.2, is very similar to the one presented section 4.1. A red line represents the muons from pair production processes, while a blue line shows those from hadron decays. The black line represents the overall spectra. The x-axis is divided into logarithmic bins and displayed in logarithmic scale to emphasize the muons coming from the decay of π's and K's, which dominate muon production below 2 GeV. Here, unlike the Hall-A secondary muons, many high-energy muons are produced by hadron decays.

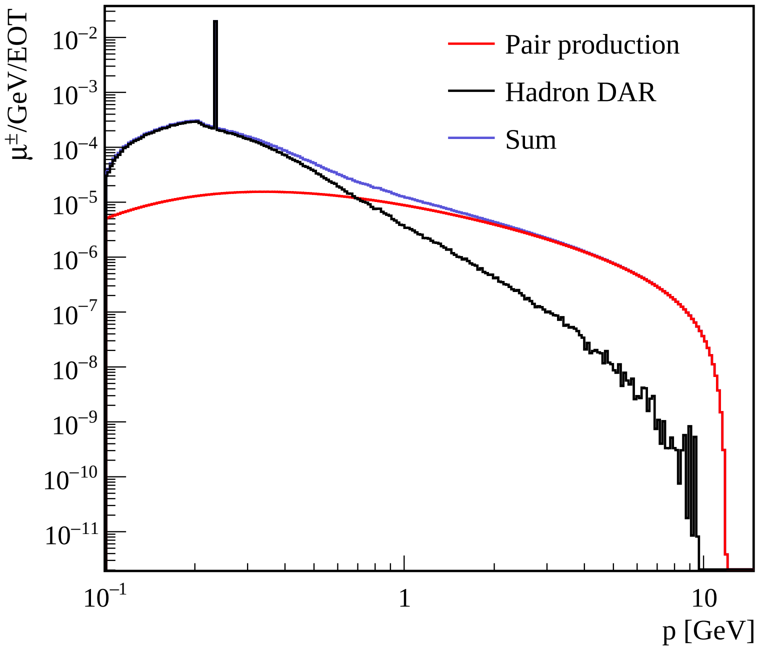

Figure 6.2: Momentum spectrum of muons produced by CPS with $p > 100$ MeV. Pair production is shown in red, and hadron decays in blue, while the sum of the two contribution is represented with a black line. The integrated blue and red spectra ratio is ~ 19. The peak at 235 MeV is due to the kaon decay-at-rest process $K \to \mu + \nu_\mu$.

The muon flux was sampled at the exit of the CPS on a 1 m^2 surface centered around the beam-axis and perpendicular to the primary e^--beam direction, corresponding to the green thick line in Figure 3.11. The momentum distribution of the muons at the exit of the CPS is presented in Figure 6.3.

The resulting muon yield per EOT at the exit of the CPS, integrated over $p_\mu > 100$ MeV, is 4×10^{-6} μ/EOT. Therefore, for the proposed e^-–beam current of 2.7 μA [101] the corresponding muon rate is 6.75×10^7 μ/s.

The muon spatial distribution on the same flux detector and the muon momentum versus their direction (θ angle) are plotted respectively in Figure 6.4 left and right images. Most muons cross the plane near the beam-axis and most of them, ~50%, are contained in an area of roughly 10×10 cm^2. Moreover, higher-energy muons are produced in the forward direction, as shown in Figure 6.4 (right).

To determine the size of the muon beam at the exit of the CPS, the distribution presented in Figure 6.3 (left) was projected along the x and y-axes and subsequently fitted with a Gaussian distribution. These plots are shown in Figure 6.5. The sigma values for the fits of both projections are approximately ~ 8 cm.

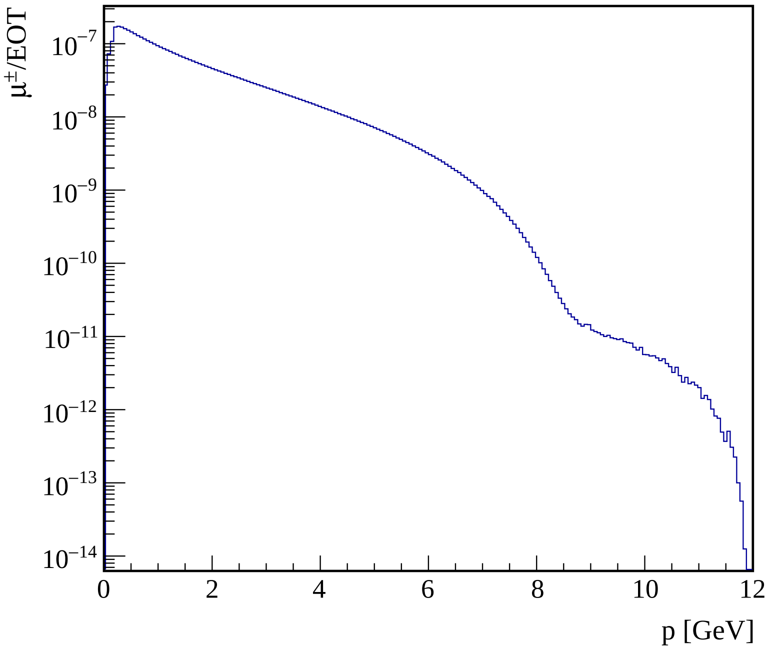

Figure 6.3: Momentum spectra of muons at the exit of the CPS, sampled on the green thick line of Figure 3.11.

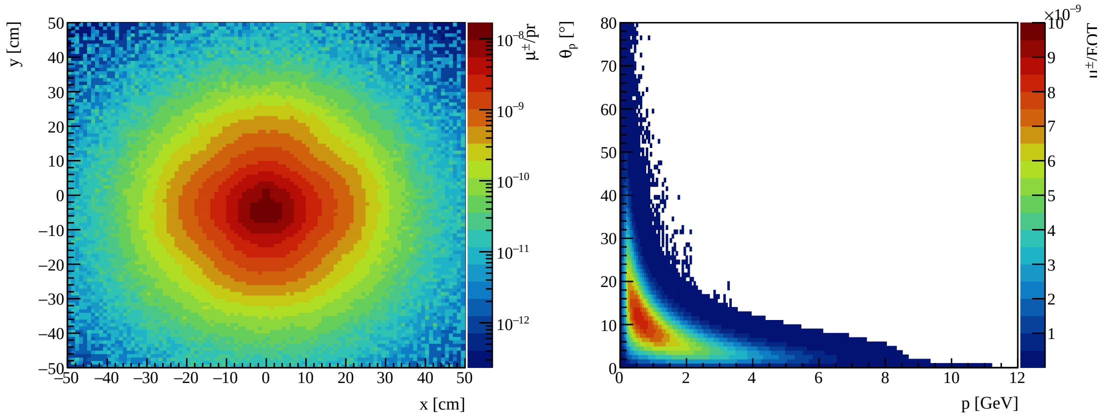

Figure 6.4: Right: muon spatial distribution produced by a 12 GeV electron beam interacting with the CPS sampled on a 1 m^2 flux detector at the exit of the CPS, green surface in Figure 3.10. Left: muon direction versus momentum. This plot shows that higher-energy muons are produced in the forward direction.

The muon spectra and spatial distribution on the "Target" flux detector of subsection 3.3.2 are presented in Figure 6.6 respectively left and right plots. In the left plot, the momentum of the muons goes up to 8 GeV, with 90% of them having a momentum $0.5 < p_\mu < 4$

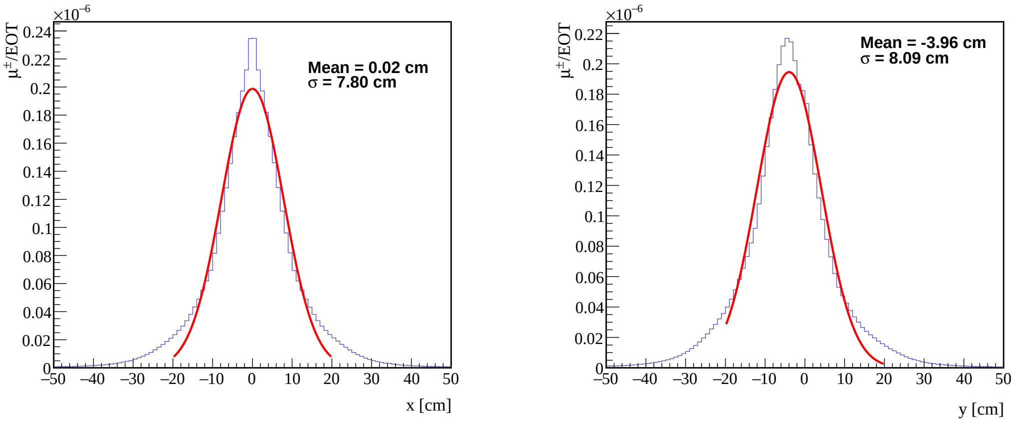

Figure 6.5: Projected muon spatial distribution along the X (right) and Y (left) axis, produced by a 12 GeV electron beam interacting with the Hall-D CPS. The flux is sampled on a 1 m^2 flux detector at the exit of the CPS. The sigma values for both projections are approximately $\sim$ 8 cm.

GeV. Moreover, with the current configuration, muons will arrive mostly in the upper part of the target, suggesting that further optimizations can be made. The integrated flux of all the muons that arrive on the target amounts to $\sim 10^{-11}$; therefore, the corresponding muon rate is $\sim 1.68 \times 10^2 \mu/\mathrm{s}$. In Table 6.1, the main characteristics of the CPS muon beam are summarised.

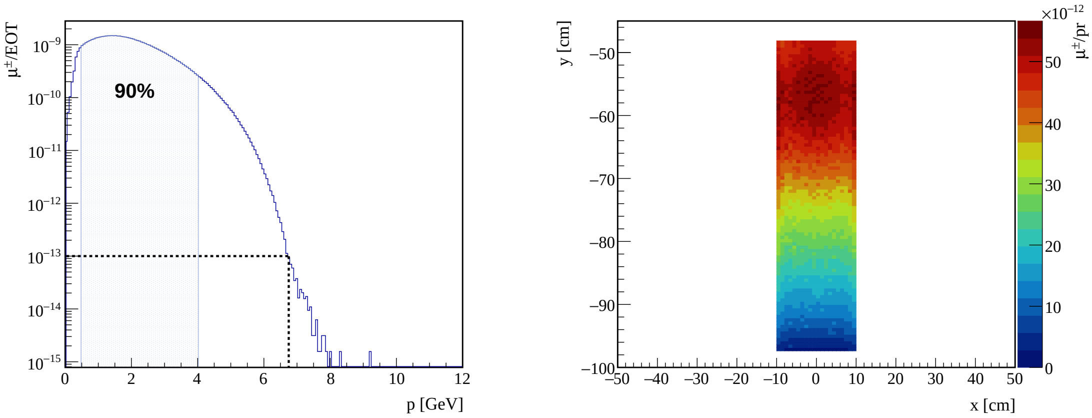

Figure 6.6: Right: spectra of the muons arriving on the target. The highlighted blue area under the plot represents approximately $\sim$ 90% of muons. The black dashed line indicates the maximum achievable energy with the proposed electron current of 2.7 μA. Left: spatial distribution of the muons arriving on the target. Most muons are concentrated on the upper part of the target.

Location	**Flux** μ/s	σ_x **(cm)**	σ_y **(cm)**
CPS's exit	6.75×10^7	7.80	8.09
Target	1.68×10^2		

Table 6.1: Summary table of the CPS muon beam.

6.2 Missing momentum experiment

This section introduces a study investigating the feasibility of a missing momentum experiment designed to search for dark matter. The idea of this experiment stems from the proposed M3 experiment at FermiLab, described in section 1.1.1. The primary objective of this study is to develop a method for accurately measuring the momentum of the muon both pre and post-interaction with the target, with a strong emphasis on minimizing the associated errors.

The first step in the tracking of the muons consisted of a custom implementation of FLUKA's `mgdraw.f` and `source_newgen.f` subroutines, allowing them to assign a unique ID to each particle, enabling the user to distinguish them perfectly. So, in this first step of the study, a realistic interpretation of a tracking detector has not yet been implemented. Next, the CPS geometry provided by the CPS collaboration was modified. Two dipoles with a magnetic field of 2 T (with opposite sign) along the x-axis with a length of 50 cm were added below the photon beam-line. Then, two tracking planes before the entrance and one at the end of each dipole were introduced into the geometry to measure the position of the muons as they crossed these planes. This setup allows momentum reconstruction using the points at which the muons cross these tracking planes and the dipole's magnetic field.

The study presented is meant only to establish a lower limit on the resolution of the missing momentum. For this reason, a very simple tracking algorithm was used under the following conditions:

- There is no dead time between hits on the flux detectors, ensuring perfect identification of a particle across all tracking planes – thus, the need to use a unique identifier for each particle.
- The magnetic field of the dipoles does have not any imperfections and is precisely 2 T inside its bore
- The tracking planes at the beginning of each dipole are separated by 20 cm
- The flux detector has a resolution of 75 µ m on the x and y position and 250 µ m on the z position. This was achieved by smearing the positions on the tracking planes

with a Gaussian function centered on the measured point and with a sigma equal to the chosen tracking plane precision.

- There is a cut on incoming particles $1 < p_\mu < 4$ GeV; every particle outside this boundary is discarded.
- The tracking algorithm considers a linear path on the xz plane and a perfect arc on the yz plane.
- The scattering on the target removes a random quantity of energy between 0–100%

A comprehensive mathematical description can be found in Appendix A.

Figure 6.7 shows the relative error on both the scattering before hitting the target (BS), with a black line, and after the scattering on the target (AS), with a red line. This plot was obtained comparing the reconstructed momentum (reco) with the one obtained from the simulation (sim). The error on the momentum using the devised algorithm is $< 10\%$ for muons with $1 < p_\mu < 4$. The error associated with the muon's energy increases as the momentum does. This is because higher momenta result in smaller displacements within the dipoles. Consequently, the arc reconstruction in the yz-plane worsens, leading to less accurate momentum measurements.

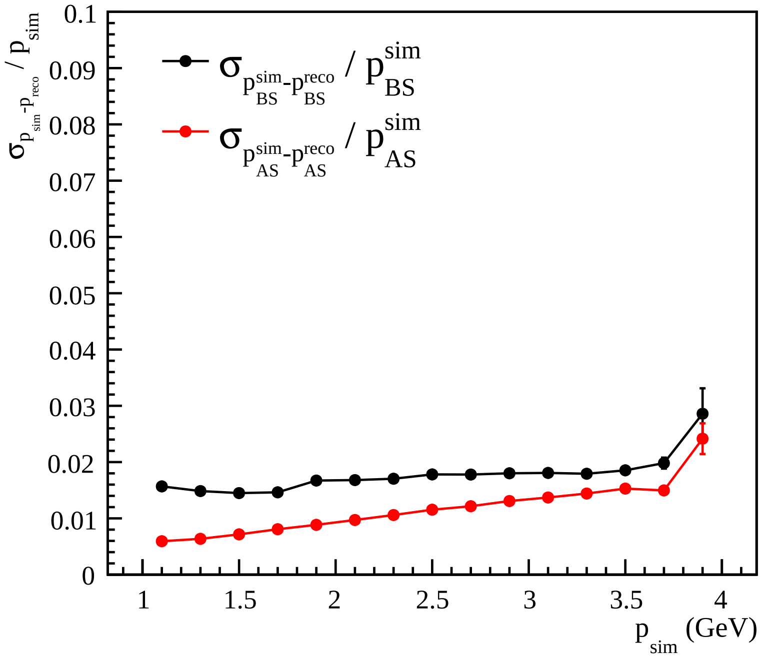

Figure 6.7: Relative error on the reconstructed momentum before (BS) and after the scattering (AS) on the target with respect to the simulated muon momentum.

The pull of the reconstruction was studied to validate the precision of the reconstruction algorithm. The pull is a quantity used to measure the deviation from the real value, which in this context is the muon momentum derived from the simulation and regarded as the expected value. The pull quantifies how far from this quantity the reconstruction had to "pull" the parameters while finding the momentum. Ideally, a healthy situation is indicated by a pull with a mean close to 0 and a standard deviation close to 1. If these conditions are not met, further examination is required.

In Figure 6.8, the pull plots for the momentum reconstruction, both before (left) and after (right) the scattering, are depicted. For both plots, the means and standard deviations are approximately 0 and 1, respectively, which suggests that the employed reconstruction algorithm is functioning effectively.

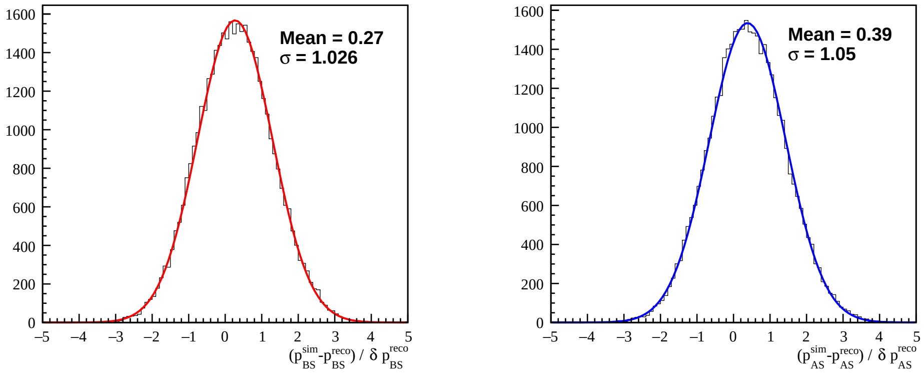

Figure 6.8: Histograms of the pulls for the momentum reconstruction before (left) and after (right) the scattering with the target. Both plots show a mean of 0 and a standard deviation of 1.

The study then focused on the error associated with the missing momentum, i.e., the difference between the momentum before and after the scattering with the target, denoted as $Q = p_{BS} - p_{AS}$. Figure 6.9 (left) presents the plot of the relative error on the missing momentum as a function of the simulated muon momentum. For muons with momentum $1 < p_{\mu} < 4$, the error in the momentum algorithm is less than 20%. The resolution worsens at higher energies. The associated pull plot is presented in Figure 6.9 (right). As before, this plot shows the goodness of the algorithm, with a mean and a standard deviation close to 0 and 1, respectively.

The study shows the feasibility of a missing momentum experiment using the CPS muon beam. However, the magnets utilized in the simulations were perfect dipoles. For this reason, a study was conducted to find a realistic solution to implement.

Starting from the studies in [110], it was possible to design an electromagnet compatible with the spaces in the Tagger Hall. The magnet built at CERN was based on the cable used for the links, encapsulated in an aluminum guide. The cable comprises 18 superconducting strands of 1 mm diameter wrapped around a copper core. The one presented in this study carries 6 kA at 20 K with a field above 1 T, here the field on the cable is of the order of 1 T, so it will be possible to make two windings of 40 turns each with a current of 5 kA.

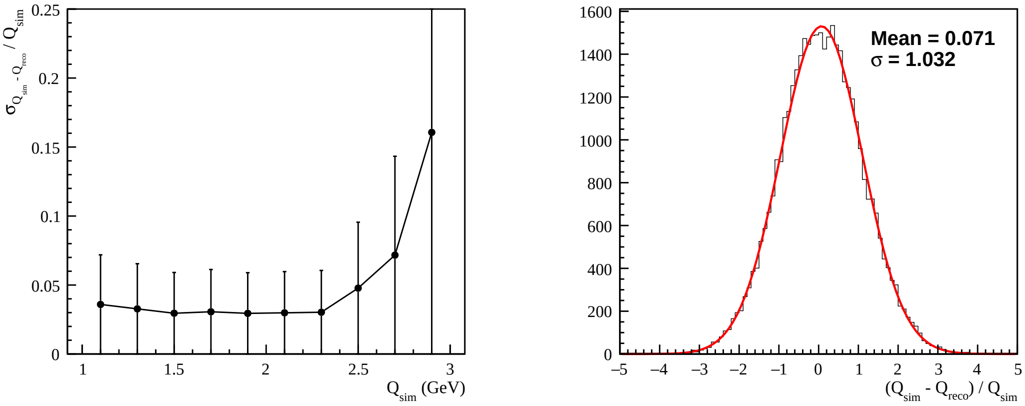

Figure 6.9: Right: relative error on the missing momentum. Left: histogram of the pull on the missing momentum.

In Figure 6.10, a possible magnet configuration is presented. The field at the center is $\sim 1.95T$ with a current of 400 kA for each coil.

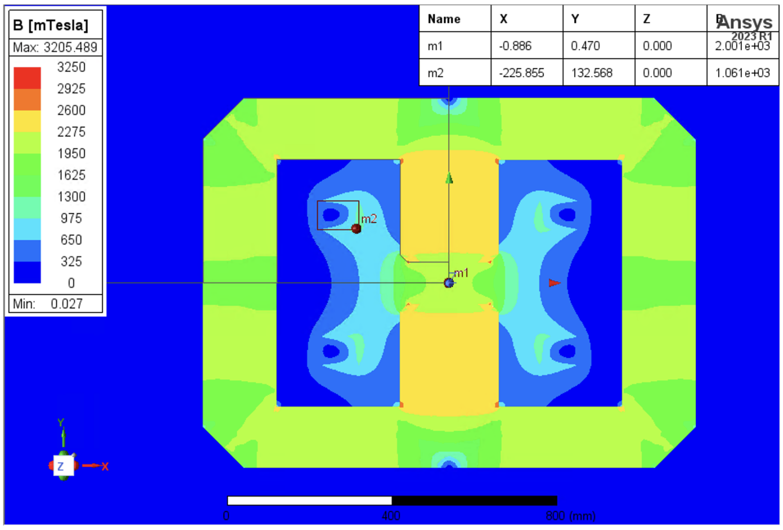

Name	X	Y	Z	B
m1	-0.886	0.470	0.000	2.001e+03
m2	-225.855	132.568	0.000	1.061e+03

Figure 6.10: Magnet design scheme consisting of two windings of 40 turns, each with a current of 5 kA. The field at the center is $\sim 1.95T$ with a current of 400 kA for each coil.

Using this configuration, experiments like the one presented in this section will be possible. However, further optimizations could reduce the space occupied by the magnets and increase the experiment's efficiency.

Conclusion

This thesis focused on the characterization of secondary beams at Jefferson Laboratory through Monte Carlo simulations. The interaction of the CEBAF electron beam and Hall-A's BD produces a high-intensity muon, neutrino, and a hypothetical LDM beam.

The secondary muon beam at Jefferson Lab's Hall-A is characterized by lower-energy muons produced primarily through hadron decays and higher-energy muons generated via photoproduction. The muons were sampled in the forward direction at the exit of the BD's concrete vault; the estimated fluxes are normalized considering a year of beam operation. The muon beam spectrum resembles the typical bremsstrahlung radiation one and is partially forward-focused. The estimated muon flux considering a 100×100 cm^2 area around the beam axis is about 9.8×10^{15} μ/year at 11 GeV and 7.6×10^{16} μ/year at 22 GeV. However, the simulations show that most muons are concentrated around the beam axis. For the 11 GeV case, the majority of the flux is concentrated in a smaller area of 25×25 cm^2 and is estimated at 1.5×10^{15} μ/year, while for the 22 GeV case is concentrated in an even smaller area of 20×20 cm^2 and is estimated at 1.9×10^{16} μ/year at 22 GeV.

Finally, in the context of the secondary muon beam, a study was conducted to explore new, cost-effective solutions for muon shielding in the BDX experiment. Two shielding configurations were evaluated: the first involving approximately 215 tons of lead, and the second around 327 tons. Simulations were performed to determine an upper limit on the number of muons reaching the BDX detector location annually. The first configuration is estimated to allow around 230 μ/year to reach the detector, while the second configuration reduces this number to approximately 170 μ/year . Each shielding configuration has its pros and cons. The first configuration, while requiring less material and minimal excavation near the detector site, poses the downside of exposing workers to higher radiation levels during construction. On the other hand, the second configuration, though more effective at reducing the number of muons reaching the detector, necessitates significant ground excavation to install the shielding, thus increasing the overall construction costs.

The yield for a hypothetical dark scalar S produced in the process $\mu + \mathrm{N} \to \mu + \mathrm{N} + S$ was calculated for the 11 GeV and 22 GeV cases. The calculations were done for two different scalar masses $m_S = 50$ MeV ($m_S = 180$ MeV). At 11 GeV, the yield was 5.27×10^{-15} S/EOT (1.32×10^{-16} S/EOT) with a beam spot size of $\sigma = 1.556$ m ($\sigma = 0.488$ m).

At 22 GeV, the yield was 1.90×10^{-14} S/EOT (1.44×10^{-15} S/EOT) with a beam spot size of $\sigma = 1.220$ m ($\sigma = 0.304$ m).

These results demonstrated that the Hall-A secondary muon beam possesses favorable characteristics, making it suitable for various experimental applications thanks to its broader energy spectrum. The high-intensity, forward-focused muon flux could be used to measure the proton radius [111], contributing to new measurements for the proton radius puzzle. Additionally, it could be used for experiments such as muon spin rotation to probe the magnetic properties of materials [112], as well as muon-to-electron conversion experiments, contributing to searches for charged lepton flavor violation [113]. Furthermore, the Hall-A muon beam could support dark photon searches where intense muon beams are necessary to probe rare processes.

The secondary neutrino beam at Jefferson Lab's Hall-A consists of low-energy neutrinos $\mathcal{O}(MeV)$ produced predominantly by decays-at-rest and high-energy neutrinos originating from decays-in-flight. The neutrino flux is isotropic, and the estimated flux above ground, normalized for one year of beam operation, is approximately $6.7 \times 10^{17} \nu/\mathrm{year}$ at 11 GeV and $1.9 \times 10^{18} \nu/\mathrm{year}$ at 22 GeV. The neutron background at the optimal position for CEνNS detection is minimized by a stepwise arrangement of lead blocks in a $4 \times 3 \times 4(x, y, z)$ meter pattern. This configuration provides an attenuation of around $O(10^4)$, effectively reducing neutrons in the range $0 - 10$ MeV.

The final section of this thesis focused on characterizing the secondary muon beam produced by the interaction of the CEBAF electron beam with the proposed Hall-D CPS. The resulting muon beam exhibits similar properties to that of Hall-A, and could be used for a muon missing momentum experiment aimed at detecting dark matter, similar to the proposed M3 experiment at Fermilab [41].

In this study, a beamline setup compatible with the spatial constraints of Hall-D's Tagger Hall was explored. This setup features a 1-meter-long, 2-Tesla dipole magnet designed to bend the muon beam downward to a region where two additional dipoles and a target are located. Monte Carlo simulations using FLUKA estimated the muon flux at the target to be approximately $1.68 \times 10^2 \mu/s$. The two 1-meter-long, 2-Tesla dipole magnets are positioned before and after the target, allowing for the measurement of the muon momentum both before and after interacting with the target, supported by multiple tracking planes. A proof-of-concept algorithm was also developed to estimate a lower bound on the missing momentum resolution, which was found to be on the order of $\mathcal{O}(10\%)$. Finally, a preliminary study was conducted to assess the feasibility of constructing magnets similar to those used in the simulation, with initial results indicating that such magnets could be readily manufactured.

Future work will involve further optimization of the BDX experiment's shielding and a deeper exploration of the potential applications of secondary beams. This includes devising detailed experiments using the muon beams from Hall-A and Hall-D and optimizing the proposed missing momentum experiment that utilizes the muon beam at Hall-D.

Appendix A

Reconstruction algorithm

The following section will detail the reconstruction algorithm employed for tracking the muons generated by the CPS. This pertains to the missing momentum experiment, discussed in section 6.2.

The algorithm was developed in Python, utilizing the pyROOT interface and several native Python libraries such as `pandas` and `numpy`. The data from the simulations is initially read from ROOT files and then converted into pandas `DataFrames` for more straightforward code implementation. ROOT is used for reading the simulation data, while `pandas` and `numpy` are employed for the needed calculations. Finally, the `uncertainties` library was used to propagate errors through all the calculations automatically.

Consider the schematic representation in Figure A.1, which shows one of the dipoles and its three tracking planes with all the information needed to perform a simple momentum measurement. When a muon approaches and enters the dipole, it hits the three planes T_1, T_2, T_3 at three distinct points P_1, P_2, P_3:

$$\begin{aligned} P_1 &= (x_1, y_1, z_1) \\ P_2 &= (x_2, y_2, z_2) \\ P_3 &= (x_3, y_3, z_3) \end{aligned}$$

From these three points, it is possible to reconstruct the momentum of the muon that traversed the dipole. Let's assume that the muon travels exactly an arc of circumference inside the dipole due to the deviation given by the magnetic field. The circumference described by the points P_2 and P_3 can be found by solving a system of three equations for the circumference parameters. The first two equations are given by the condition that the circumference must pass from P_2 and P_3. The third one is given from the fact that the muon in P_2 must be tangent to the equation.

The easiest way to solve this problem is to consider a new origin system where the origin

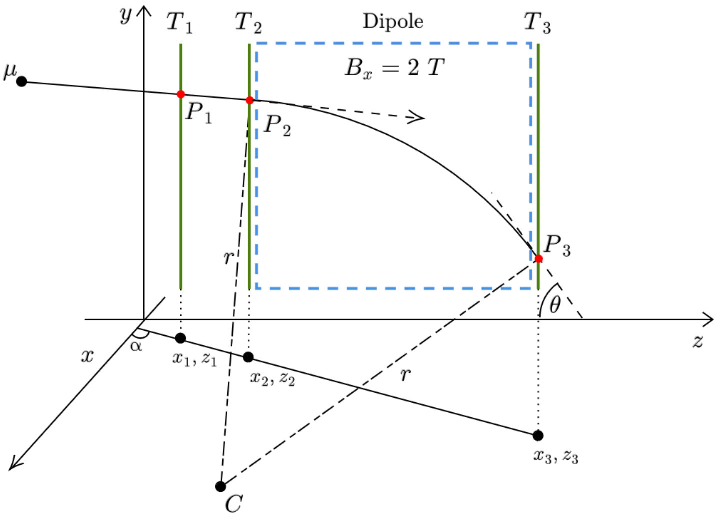

Figure A.1: Schematic representation of the geometry implemented in FLUKA to track muons.

$O' \equiv P_2$ and the z-axis lie on the line $\overline{P_1P_2}$. In this new reference frame, the radius r and the center's coordinates y'_C and z'_C of the circumference described by the arc between P_2 and P_3 on the $y'z'$-plane, can be easily demonstrated to be:

$$r = \left| \frac{-{y'_3}^2 - {z'_3}^2}{2y'_3} \right|$$

$$y'_C = \frac{{y'_3}^2 + {z'_3}^2}{2y'_3}$$

$$z'_C = 0$$

Then, by applying the reverse transformation to the circumference center coordinates, the momentum transversal component $p_\perp$ is found as:

$$p_\perp = eB_x r$$

Where e is the elementary charge, B_x is the magnitude of the magnetic field along the x-axis. The components of the momentum in the yz plane can be found by calculating the angle θ between the line tangent to the circumference on P_3 and the z-axis:

$$\begin{aligned} p_y &= p_\perp \sin\theta \\ p_z &= p_\perp \cos\theta \end{aligned}$$

The momentum component on the x-axis is found by fitting a line between P_1, P_2 and P_3 on the xs-plane and finding its slope α:

$$p_x = p_\perp \alpha$$

The algorithm is implemented in python and presented in section B.3.

Appendix B

Simulation codes

B.1 Custom event saving

The Fortran code presented in this section is part of a custom FLUKA subroutine implementation called `MGDRAW`. It is used in FLUKA to record and save custom events such as particle interactions, boundary crossings, and particle generation. It contains several entry points that handle different aspects of particle tracking and event recording. It is used with a custom ROOT library linked to the FLUKA executable to save the events in the ROOT file format.

The main subroutine initializes the necessary variables and logical flags. The entry point `BXDRAW` monitors when particles cross from one region to another, such as between "ENCLOS1" and "NATM". When this boundary crossing occurs, the subroutine records particle properties like position, energy, and momentum using the `treefill` function.

The `ENDRAW` entry is triggered when particles interact in a predefined region called "TARGET". It captures particle details such as energy, position, and momentum, storing them through the `depfill` function.

Another entry point, `SODRAW`, is responsible for sampling source particles. This functionality allows the subroutine to save initial properties like the position, total kinetic energy, and momentum of source particles via `sourcefill` function.

The `USDRAW` entry tracks general events when certain conditions are met, saving information about particles, such as the interaction point and the mother particle's total energy. A key feature of this entry is its ability to handle muons produced through photoproduction or decay processes within a specific range of regions (122 to 667, representing the dump volume). The subroutine distinguishes between "decay-at-rest" and "decay-in-flight" scenarios. For muons generated by photoproduction or decay, the function `usdfill` is used to store relevant data like energy, momentum, and track position.

Overall, MGDRAW provides a flexible framework for tracking and saving custom particle events in FLUKA simulations, allowing for detailed analysis, particularly of muon behavior and particle interactions within specific regions.

FLUKA user routine: mgdraw.f

```
SUBROUTINE MGDRAW ( ICODE, MREG )

[...]

CHARACTER*8 INREG
CHARACTER*8 OUTREG

double precision :: pID

INTEGER :: SURFID
INTEGER :: REGIONID

LOGICAL LFCOPE
SAVE LFCOPE
DATA LFCOPE / .FALSE. /

RETURN

ENTRY BXDRAW ( ICODE, MREG, NEWREG, XSCO, YSCO, ZSCO )

CALL GEOR2N (MREG, INREG, IERR)
CALL GEOR2N (NEWREG, OUTREG, IERR)

!sample selected particles
IF((JTRACK.eq.10).or.(JTRACK.eq.11)) THEN

!at the boundary crossing between 2 regions
IF((INREG.eq."ENCLOS1").and.(OUTREG.eq."NATM")) THEN
        SURFID = 1
        CALL treefill (NCASE,
&               SURFID,JTRACK,ETRACK,PTRACK,
&               XSCO, YSCO, ZSCO,
&               CXTRCK, CYTRCK, CZTRCK,
&               WTRACK, WSCRNG,
&               ISPUSR(1),ISPUSR(2),
&               SPAUSR(1),SPAUSR(2),SPAUSR(3),SPAUSR(4),
&               pID)

END IF
END IF

RETURN
*
ENTRY EEDRAW ( ICODE )
RETURN
*
ENTRY ENDRAW ( ICODE, MREG, RULL, XSCO, YSCO, ZSCO )
IF(REGION.eq."TARGET")THEN
        REGIONID = 1
        CALL depfill(NCASE,
&                  REGIONID,ICODE,JTRACK,ETRACK,PTRACK,
&                  XSCO, YSCO, ZSCO,
&                  PTRACK*CXTRCK, PTRACK*CYTRCK, PTRACK*CZTRCK,
&                  CXTRCK, CYTRCK, CZTRCK,
&                  WTRACK, WSCRNG,
```

```
&                  ISPUSR(1),ISPUSR(2),
&                  SPAUSR(2),SPAUSR(3),SPAUSR(4),SPAUSR(5),
&                  pID)
    END IF

RETURN
*
ENTRY SODRAW

!sample source particles
!to activate this remember to put userdump what(4)=4
CALL sourcefill ( NCASE, ILOFLK(NPFLKA),
&                  TKEFLK(NPFLKA), PMOFLK(NPFLKA),
&                  XFLK(NPFLKA), YFLK(NPFLKA), ZFLK(NPFLKA),
&                  TXFLK(NPFLKA), TYFLK(NPFLKA), TZFLK(NPFLKA),
&                  WTFLK(NPFLKA)
&                )

RETURN

ENTRY USDRAW ( ICODE, MREG, XSCO, YSCO, ZSCO )

!sample particles when certain events happen
!to activate this remember to put userdump what(5)=1

!this to generic save the mother particle and production vertex,  work for everything except special cases handled below
ISPUSR(1) = JTRACK      !mother particle ID
ISPUSR(2) = ICODE       !process code

SPAUSR(1) = ETRACK      !mother particle total energy

SPAUSR(2) = XSCO        !interaction point
SPAUSR(3) = YSCO
SPAUSR(4) = ZSCO


! Everytime in the selected region, there is a muon in the secondary produced, then:
! if the decay of something produces the muon, then it saves it through the secondary stack
! if the muon is photoproduced, it checks if the number of secondaries produced is less than 1, and it saves it through Fluka stack

! In this case, it is better to use the region number instead of the name
! In this geometry, we are interested in muons produced in the beam-dump
! Their number ranges from WINDOWS n122 to TANKTAIL n667

!here to restrict for photoproduced muons only
IF ((ICODE.EQ.237).AND.(NPFLKA.GT.0)) THEN
        DO I=NPFLKA-1,NPFLKA
            !double check to restrict for muons only
            IF((ILOFLK(I).eq.10).or.(ILOFLK(I).eq.11)) THEN
                    !here to selected a range of regions (the dump volume)
                    IF((MREG.ge.122).and.(MREG.le.667)) THEN
                    CALL usdfill(NCASE, MREG, ICODE, ILOFLK(I),
&                                TKEFLK(I), PMOFLK(I),
&                                XSCO, YSCO, ZSCO,
&                                TXFLK(I), TYFLK(I), TZFLK(I), WTFLK(I),
&                                JTRACK, ETRACK)
                    END IF
            END IF
```

```
        END DO
ELSE IF (ICODE.EQ.102) THEN !select particles produced by decays
        AX=ZERZER
        AY=ZERZER
        AZ=ZERZER

        DO n=1, NP
!                 set custom icode for that dacay-at-rest or decay-in-flight
            IF(ABS(AX).LT.ANGLGB.AND.ABS(AY).LT.ANGLGB.AND.ABS(AZ).LT.ANGLGB) THEN
                    ISPUSR(2) = 1021                !decay-at-rest
            ELSE
                    ISPUSR(2) = 1020                !decay-in-flight
            END IF

            !here to restrict for muons only
            IF ((KPART(n).eq.10).or.(KPART(n).eq.11)) THEN
                    !here to selected a range of regions (the dump volume)
                    IF((MREG.ge.122).and.(MREG.le.667)) THEN
                    CALL usdfill(NCASE, MREG, ISPUSR(2), KPART(n),
&                               TKI(n), PLR(n), XSCO, YSCO, ZSCO,
&                               CXR(n), CYR(n), CZR(n), WEI(n),
&                               JTRACK, ETRACK)
                    END IF
            END IF


        END DO
END IF


RETURN
END
```

B.2 Custom bias

The Fortran code presented in this section is used in FLUKA for custom biasing on neutrons. It defines a subroutine `USIMBS` that adjusts the simulation biasing factor (`FIMP`) based on material properties, neutron energy, and direction.

The subroutine applies biasing only when neutrons interact with specific materials: concrete, soil, and lead. The biasing factor is adjusted using attenuation coefficients (`attenuation_b20`, `attenuation_a20`) that depend on the material and the neutron's energy (`EKIN`). The biasing is applied only to neutrons traveling upwards, using the variable `CYTRCK`, which refers to the neutron's vertical cosine direction. The biasing factor is multiplied by 1.2D0 to speed up result convergence, increasing the number of neutrons in the simulation.

FLUKA user routine: usimbs.f

```fortran
SUBROUTINE USIMBS ( MREG, NEWREG, FIMP )
[...]
save step_saved

! coordinate of the point toward which direct the biasing
data x_target, y_target, z_target /0.d0, 850.d0, 4830.d0/

!attenuation coefficients
data attenuation_b20 /0.003070d0/
data attenuation_a20 /0.00051d0/

double precision :: EKIN

FIMP   = ONEONE

if ( JTRACK .eq. 8 ) then
        ! calculate the kinetic energy of the neutrons
        EKIN = ETRACK - 0.939565378d0
        ! retrieve the material ID
        IMAT = MEDFLK(MREG,1)

        ! apply usimbs only inside concrete, soil and lead
        if ((MATNAM(IMAT).eq."Concrete") .or. (MATNAM(IMAT).eq."Soil") .or.
        ↪   (MATNAM(IMAT).eq."LEAD")) then
            ! compensate the attenuation in lead
            if (EKIN.le.20.d0) then
                    if (MATNAM(IMAT) .eq. "LEAD") then
                        FIMP = FIMP * exp(step_saved*attenuation_b20*5)
                    else
                        FIMP = FIMP * exp(step_saved*attenuation_a20)
                    end if
            else if (EKIN.lt.20.d0) then
                    if (MATNAM(IMAT) .eq. "LEAD") then
                        FIMP = FIMP * exp(step_saved*attenuation_b20*5)
                    else
                        FIMP = FIMP * exp(step_saved*attenuation_a20)
                    end if

            [...]

```

```
            end if

        !increase the number of neutron to speed up results convergence
        FIMP = 1.2D0 * FIMP

        ! apply the biasing only for neutrons going upwards
        FIMP = FIMP ** CYTRCK

        else
            return
        endif

endif
RETURN

ENTRY USIMST ( MREG, STEP )
*
IF ( STEP .GT. ONEONE ) STEP = HLFHLF * STEP
RETURN

! save the length of the step in order to use it for biasing
step_saved = STEP
END
```

B.3 Reconstruction code

Reconstruction algorithm

```
import numpy as np
import uncertainties as un
import uncertainties.umath as unm
from uncertainties import ufloat
from utils.rotate_point import rotate_point_un
from scipy.stats import linregress
from scipy.odr import ODR, Model, Data, RealData

def rotate_point_un(p, origin=(0, 0), angle=0):
    R = np.array([[unm.cos(angle), -unm.sin(angle)],
                  [unm.sin(angle),  unm.cos(angle)]])

    - = np.atleast_2d(origin)
    p = np.atleast_2d(p)

    return np.squeeze((R @ (p.T-o.T) + o.T).T)

def reconstruct_p_un(P1, P2, P3, errors, field):
    x_1 = ufloat(P1[0], errors[0])
    y_1 = ufloat(P1[1], errors[1])
    z_1 = ufloat(P1[2], errors[2])

    x_2 = ufloat(P2[0], errors[0])
    y_2 = ufloat(P2[1], errors[1])
    z_2 = ufloat(P2[2], errors[2])

    x_3 = ufloat(P3[0], errors[0])
    y_3 = ufloat(P3[1], errors[1])
    z_3 = ufloat(P3[2], errors[2])

    #Find the slope of the line between the first 2 points
    m = (y_1 - y_2) / (z_1 - z_2)

    #Convert the slope to angle (this is the angle between the hit on the second tracker
    ↪  and the z axis)
    alpha_2 = unm.atan(m)

    #Rotate the point P3 to the new reference system O'y'z'
    #where z' is on the line between P1 and P2 and y' is perpendicular
    pointp = rotate_point_un([(y_3, z_3)], origin=(y_2, z_2), angle=alpha_2)

    #Traslate these point to get the coordinates in the new reference frame
    yp_3 = pointp[0] - y_2
    zp_3 = pointp[1] - z_2

    #Find the radius of the circle, no other transformation is needed because it is
    ↪  invariant between RS
    r = unm.fabs((- yp_3**2 - zp_3**2) / (2 * yp_3))

    #Find the center of the circle
    yp_c = (yp_3**2 + zp_3**2) / (2 * yp_3)
    zp_c = 0
    #because our reference system is along the line between P1 and P2

    #Rotoslate back the center to the orginal reference frame
    pointc = rotate_point_un([(yp_c, zp_c)], origin=(y_2, z_2), angle=-alpha_2)
```

```
    y_c = pointc[0] + y_2
    z_c = pointc[1] + z_2

    #Find the line between the center of the circle and the third point
    m_2 = (y_c - y_3) / (z_c - z_3)
    m_2_perp = -1 / m_2

    #Find the angle the perpendicular line makes with the z axis
    alpha_3 = unm.atan(m_2_perp)

    #reconstruct the px component
    xs = [x_1.n, x_2.n, x_3.n]
    zs = [z_1.n, z_2.n, z_3.n]

    xse = [x_1.s, x_2.s, x_3.s]
    zse = [z_1.s, z_2.s, z_3.s]

    data = RealData(zs, xs, zse, xse)
    model = Model(func)

    odr = ODR(data, model, [0.,0.])
    odr.set_job(fit_type=2)
    result = odr.run()

    slope_n = result.beta[0]
    slope_e = result.sd_beta[0]
    slope   = ufloat(slope_n, slope_e)

    if field > 0:
        particle_sign = +1
    elif field < 0:
        particle_sign = -1

    #Find the transverse momentum and convert it to GeV
    pt = particle_sign * 1.602176634e-19 * field * r / (5.36e-19)

    #find the projection of pt along y and z
    px = pt * slope
    py = pt * unm.sin(alpha_3)
    pz = pt * unm.cos(alpha_3)

    return px,py,pz
```

B.4 Fluka output to ROOT

The following C++ code integrates with FLUKA to save simulation data using ROOT trees, allowing for detailed event recording and analysis. The code defines several functions that interact with FLUKA to store information about different types of particle events, such as source particles, boundary-crossing events, deposition events, and user-defined events. It uses ROOT to create and manage .root files and trees for storing simulation data.

FLUKA output to ROOT

```cpp
#include <stdio.h>
#include <iostream>
#include <TTree.h>
#include <TFile.h>


#ifndef WIN32
#define myusrini myusrini_
#else
#define myusrini MYUSRINI
#endif

static TFile *RootFile  = 0;

static TTree *Source    = 0;
static TTree *Events    = 0;
static TTree *DepEvents = 0;
static TTree *USDEvents = 0;

static TTree *SimulationSummary = 0;

bool first1 = true;
[...]

double EKin_src;
[...]


int    NCase_vnt;
[...]

int    NCase_dep;
[...]

int    NCase_usd;
[...]

extern "C" {
    void myusrini (){
    printf("Executing MYUSRINI\n");
    RootFile  = new TFile("dump.root","recreate");
    Source    = new TTree("Source", "Particles");
    Events    = new TTree("Events", "Particles");
    DepEvents = new TTree("DepEvents", "Particles");
    USDEvents = new TTree("USDEvents", "Particles");
    SimulationSummary = new TTree("RunSummary", "RunSummary");
```

```

    Source->SetAutoSave(0);
    Events->SetAutoSave(0);
    DepEvents->SetAutoSave(0);
    USDEvents->SetAutoSave(0);
    SimulationSummary->SetAutoSave(0);

    }
}

#ifndef WIN32
#define sourcefill sourcefill_
#else
#define sourcefill SOURCEFILL
#endif

extern "C" {
    void sourcefill(Int_t &NCase, Int_t &ParticleID,
                Double_t &EKin, Double_t &P,
                Double_t &Vx, Double_t &Vy, Double_t &Vz,
                Double_t &Cx, Double_t &Cy, Double_t &Cz,
                Double_t &Weight
                ){

    NCase_src      = NCase;
    [...]

    if(first1){
        Source->Branch("NCase",       &NCase_src);
        [...]

        first1 = false;
    }


    Source->Fill();
    }
}

#ifndef WIN32
#define treefill treefill_
#else
#define treefill TREEFILL
#endif

extern "C" {
    void treefill(Int_t &NCase, Int_t &SurfaceID, Int_t &ParticleID,
                Double_t &ETot, Double_t &P, Double_t &Vx, Double_t &Vy, Double_t &Vz,
                Double_t &Cx, Double_t &Cy, Double_t &Cz,
                Double_t &Weight1, Double_t &Weight2,
                Int_t &MotherID, Int_t &ProcessID,
                Double_t &MotherETot, Double_t &MotherVx, Double_t &MotherVy, Double_t
                 ↪  &MotherVz,
                Double_t &UniqueID
                ){

    NCase_vnt      = NCase;
    [...]


    if(first2){
```

```
        Events->Branch("NCase",       &NCase_vnt);
        [...]


        first2 = false;
    }

    Events->Fill();
    }
}

#ifndef WIN32
#define depfill depfill_
#else
#define depfill DEPFILL
#endif

extern "C" {
    void depfill(Int_t &NCase, Int_t &RegionID, Int_t &ICode, Int_t &ParticleID,
                Double_t &ETot, Double_t &P, Double_t &Vx, Double_t &Vy, Double_t &Vz,
                Double_t &Cx, Double_t &Cy, Double_t &Cz,
                Double_t &Weight1, Double_t &Weight2,
                Int_t &MotherID, Int_t &ProcessID,
                Double_t &MotherETot, Double_t &MotherVx, Double_t &MotherVy, Double_t
                ↪   &MotherVz
                ){

    NCase_dep       = NCase;
    [...]

    if(first3){
        DepEvents->Branch("NCase",      &NCase_dep);
        [...]

        first3 = false;
    }


    DepEvents->Fill();
    }
}

#ifndef WIN32
#define usdfill usdfill_
#else
#define usdfill USDFILL
#endif

extern "C" {
    void usdfill(Int_t &NCase, Int_t &RegionID, Int_t &ICode, Int_t &ParticleID,
                Double_t &EKin, Double_t &P, Double_t &Vx, Double_t &Vy, Double_t &Vz,
                Double_t &Cx, Double_t &Cy, Double_t &Cz,
                Double_t &Weight,
                Int_t &MotherID,
                Double_t &MotherETot
                ){

    NCase_usd       = NCase;
    [...]

    if(first4){
```

```
        USDEvents->Branch("NCase",      &NCase_usd);
        [...]

        first4 = false;
    }


    USDEvents->Fill();
    }
}




#ifndef WIN32
#define fileclose fileclose_
#else
#define fileclose FILECLOSE
#endif

extern "C" {
    void fileclose(Int_t &TotEvent, Double_t &AvgTime, Double_t &TotTime){

    SimulationSummary->Branch("TotEvents",&TotEvent);
    SimulationSummary->Branch("AvgTime",  &AvgTime);
    SimulationSummary->Branch("TotTime",  &TotTime);
    SimulationSummary->Fill();

    SimulationSummary->Write();
    Source->Write();
    Events->Write();
    DepEvents->Write();
    USDEvents->Write();

    RootFile->Close();
    }
}
```

Bibliography

[1] Verena Walbrecht and Giulia Neri. “Experiments with Pion-Beam”. In: *PoS* Bormio2014 (2014), p. 010. DOI: `10.22323/1.212.0010` (cit. on p. 5).

[2] H. Ohnishi, F. Sakuma, and T. Takahashi. “Hadron Physics at J-PARC”. In: *Progress in Particle and Nuclear Physics* 113 (2020), p. 103773. ISSN: 0146-6410. DOI: `https://doi.org/10.1016/j.ppnp.2020.103773` (cit. on p. 5).

[3] Jana Rieger. “The FAIR Phase-0 Hyperon Program at HADES”. In: *EPJ Web Conf.* 291 (2024), p. 05005. DOI: `10.1051/epjconf/202429105005` (cit. on p. 5).

[4] Ciepał, Izabela. “Studies of Time-like Electromagnetic Structure of Baryons with HADES”. In: *EPJ Web Conf.* 291 (2024), p. 01011. DOI: `10.1051/epjconf/202429101011` (cit. on p. 5).

[5] Strakovsky, Igor I. “K-Long Facility for JLab and its Scientific Potential”. In: *EPJ Web Conf.* 130 (2016), p. 06005. DOI: `10.1051/epjconf/201613006005` (cit. on p. 6).

[6] Taku Yamanaka and for the KOTO Collaboration. “The J-PARC KOTO experiment”. In: *Progress of Theoretical and Experimental Physics* 2012.1 (Dec. 2012), 02B006. ISSN: 2050-3911. DOI: `10.1093/ptep/pts057` (cit. on p. 6).

[7] P. Checchia. “Review of possible applications of cosmic muon tomography”. In: *Journal of Instrumentation* 11.12 (2016), p. C12072. DOI: `10.1088/1748-0221/11/12/C12072` (cit. on p. 6).

[8] Adrian D. Hillier et al. “Muon spin spectroscopy”. In: *Nature Reviews Methods Primers* 2.1 (2022), p. 4. ISSN: 2662-8449. DOI: `10.1038/s43586-021-00089-0` (cit. on p. 6).

[9] Manuela Boscolo, Delahaye jean-pierre, and Mark Palmer. “The Future Prospects of Muon Colliders and Neutrino Factories”. In: *Reviews of Accelerator Science and Technology* 10 (Aug. 2019), pp. 189–214. DOI: `10.1142/S179362681930010X` (cit. on p. 6).

[10] M. Sajjad Athar and S. K. Singh. “Neutrinos and their interactions”. In: *The European Physical Journal Special Topics* 230.24 (2021), pp. 4215–4220. ISSN: 1951-6401. DOI: `10.1140/epjs/s11734-021-00302-x` (cit. on p. 6).

[11] Hiroshi Nunokawa, Stephen Parke, and José W.F. Valle. “CP violation and neutrino oscillations”. In: *Progress in Particle and Nuclear Physics* 60.2 (2008). ISSN: 0146-6410. DOI: `10.1016/j.ppnp.2007.10.001` (cit. on p. 6).

[12] Srubabati Goswami and Newton Nath. “Determination of CP violation in the lepton sector”. In: *AIP Conference Proceedings* 2109.1 (June 2019), p. 110004. ISSN: 0094-243X. DOI: `10.1063/1.5110143` (cit. on p. 6).

[13] Andrew R. Liddle. *An introduction to modern cosmology*. Wiley, 2003 (cit. on pp. 6, 17).

[14] Rupert Coy et al. “Domain of thermal dark matter candidates”. In: *Phys. Rev. D* 104.5 (2021), p. 055021. DOI: `10.1103/PhysRevD.104.055021` (cit. on pp. 6, 17).

[15] G. W. Bennett et al. “Measurement of the negative muon anomalous magnetic moment to 0.7 ppm”. In: *Phys. Rev. Lett.* 92 (2004), p. 161802. DOI: `10.1103/PhysRevLett.92.161802` (cit. on pp. 6, 17).

[16] B. Abi et al. “Measurement of the Positive Muon Anomalous Magnetic Moment to 0.46 ppm”. In: *Phys. Rev. Lett.* 126.14 (2021), p. 141801. DOI: `10.1103/PhysRevLett.126.141801` (cit. on pp. 6, 17).

[17] J Drees and HE Montgomery. “Muon scattering”. In: *Annual Review of Nuclear and Particle Science* 33.1 (1983), pp. 383–452 (cit. on p. 6).

[18] L.J. Schultz et al. “Image reconstruction and material Z discrimination via cosmic ray muon radiography”. In: *Nuclear Instruments and Methods in Physics Research Section A: Accelerators, Spectrometers, Detectors and Associated Equipment* 519.3 (2004), pp. 687–694. ISSN: 0168-9002. DOI: `https://doi.org/10.1016/j.nima.2003.11.035` (cit. on p. 7).

[19] K. Nagamine et al. “Probing magnetism in human blood by muon spin relaxation”. In: *Physica B: Condensed Matter* 374-375 (2006). Proceedings of the Tenth International Conference on Muon Spin Rotation, Relaxation and Resonance, pp. 444–447. ISSN: 0921-4526. DOI: `https://doi.org/10.1016/j.physb.2005.11.128` (cit. on p. 7).

[20] Sergey S Kurennoy, Andrew J Jason, and Haruo Miyadera. “Large-acceptance linac for accelerating l9w-energy muons”. In: (Jan. 2010) (cit. on p. 7).

[21] D. P. Aguillard et al. *Measurement of the Positive Muon Anomalous Magnetic Moment to 0.20 ppm*. 2023. DOI: `https://doi.org/10.48550/arXiv.2308.06230` (cit. on p. 7).

[22] A. Yaouanc and P.D. de Réotier. *Muon Spin Rotation, Relaxation, and Resonance: Applications to Condensed Matter*. International Series of Monographs on Physics. OUP Oxford, 2011. ISBN: 9780199596478 (cit. on p. 7).

[23] Subhendu Das, Sridhar Tripathy, et al. "Muography for Inspection of Civil Structures". In: *Instruments* 6.4 (2022). ISSN: 2410-390X. DOI: `10.3390/instruments6040077` (cit. on p. 7).

[24] *μSR Beamlines at TRIUMF*. `https://cmms.triumf.ca/equip/muSRbeamlines.html`. July 2023 (cit. on p. 7).

[25] Daniela Kiselev. *PSI Muon Facilities*. `https://indico.cern.ch/event/1016248/contributions/4282379/attachments/2215080/3749805/Muoncollider_CERN24.3.2021.pdf`. 2023 (cit. on p. 7).

[26] Y. Miyake et al. "J-PARC muon source, MUSE". In: *NIM A* 600.1 (2009), pp. 22–24. ISSN: 0168-9002. DOI: `https://doi.org/10.1016/j.nima.2008.11.016` (cit. on p. 7).

[27] *ISIS muon source*. `https://www.isis.stfc.ac.uk/Pages/Muons.aspx`. July 2023 (cit. on p. 7).

[28] S. Ganguly. "Muon Campus at Fermilab". In: (Aug. 2022). DOI: `https://doi.org/10.48550/arXiv.2208.02889` (cit. on p. 7).

[29] *M2 beam line*. `https://sba.web.cern.ch/sba/BeamsAndAreas/M2/M2_presentation.html`. CERN, July 2023 (cit. on p. 7).

[30] Travis J. Williams et al. "SEEMS: A Single Event Effects and Muon Spectroscopy facility at the Spallation Neutron Source". In: *Review of Scientific Instruments* 94.3 (Mar. 2023), p. 033908. ISSN: 0034-6748. DOI: `10.1063/5.0135721` (cit. on p. 7).

[31] Young Jin Kim. "Current status of experimental facilities at RAON". In: *NIM B* 463 (2020), pp. 408–414. ISSN: 0168-583X. DOI: `https://doi.org/10.1016/j.nimb.2019.04.041` (cit. on p. 7).

[32] Cong Chen, Yu Bao, and Nikolaos Vassilopoulos. "Design of the surface muon beamline of MELODY". In: *J. Phys. Conf. Ser.* 2462.1 (2023), p. 012027. DOI: `10.1088/1742-6596/2462/1/012027` (cit. on p. 7).

[33] N. Doble et al. "The upgraded muon beam at the SPS". In: *Nuclear Instruments and Methods in Physics Research Section A: Accelerators, Spectrometers, Detectors and Associated Equipment* 343.2 (1994), pp. 351–362. ISSN: 0168-9002. DOI: `https://doi.org/10.1016/0168-9002(94)90212-7` (cit. on p. 9).

[34] G Abbiendi. *Letter of Intent: the MUonE project*. Tech. rep. The collaboration has not yet a structure, therefore the names above are for the moment an indication of contacts. Geneva: CERN, 2019 (cit. on p. 9).

[35] Sergei Gninenko. *Proposal for an experiment to search for dark sector particles weakly coupled to muon at the SPS*. Tech. rep. Geneva: CERN, 2019. DOI: 10.17181/CERN.LEK5.04J3 (cit. on p. 9).

[36] B Adams et al. *COMPASS++/AMBER: Proposal for Measurements at the M2 beam line of the CERN SPS Phase-1: 2022-2024*. Tech. rep. The collaboration has not yet constituted itself, thus instead of a Spokesperson currently the nominated Contact Person is acting in place. Geneva: CERN, 2019 (cit. on p. 9).

[37] B. Adams et al. *A New QCD facility at the M2 beam line of the CERN SPS: COMPASS++/AMBER*. Tech. rep. No spokesperson determined yet. Geneva: CERN, 2019 (cit. on p. 9).

[38] S. Ganguly. *Muon Campus at Fermilab*. 2022 (cit. on p. 9).

[39] Stratakis Diktys. *Muon Beams at Fermilab*. Presentation. 2021 (cit. on p. 9).

[40] *Muon g-2 (Website)*. URL: https://muon-g-2.fnal.gov/ (visited on 08/26/2024) (cit. on p. 10).

[41] Yonatan Kahn et al. "M3: a new muon missing momentum experiment to probe (g - 2)µand dark matter at Fermilab". In: *Journal of High Energy Physics* 2018.9 (2018). ISSN: 1029-8479. DOI: 10.1007/jhep09(2018)153 (cit. on pp. 10, 44, 92).

[42] J. Cox et al. "A high energy, small phase-space volume muon beam". In: *Nuclear Instruments and Methods* 69.1 (1969), pp. 77–88. ISSN: 0029-554X. DOI: https://doi.org/10.1016/0029-554X(69)90575-8 (cit. on pp. 11, 14, 47).

[43] Yung-Su Tsai. "Pair production and bremsstrahlung of charged leptons". In: *Rev. Mod. Phys.* 46 (4 1974), pp. 815–851. DOI: 10.1103/RevModPhys.46.815 (cit. on pp. 12, 13).

[44] Wolfgang Pauli. "Pauli letter collection: letter to Lise Meitner". Typed copy (cit. on p. 14).

[45] C. L. Cowan et al. "Detection of the Free Neutrino: a Confirmation". In: *Science* 124.3212 (1956), pp. 103–104. DOI: 10.1126/science.124.3212.103 (cit. on p. 15).

[46] C Athanassopoulos et al. "The liquid scintillator neutrino detector and LAMPF neutrino source". In: *NIM A* 388.1 (1997), pp. 149–172. ISSN: 0168-9002. DOI: https://doi.org/10.1016/S0168-9002(96)01155-2 (cit. on p. 15).

[47] A. A. Aguilar-Arevalo et al. "Neutrino flux prediction at MiniBooNE". In: *Phys. Rev. D* 79 (7 2009), p. 072002. DOI: 10.1103/PhysRevD.79.072002 (cit. on p. 15).

[48] D. Akimov et al. “First Measurement of Coherent Elastic Neutrino-Nucleus Scattering on Argon”. In: *Phys. Rev. Lett.* 126 (1 2021), p. 012002. DOI: `10.1103/PhysRevLett.126.012002` (cit. on p. 15).

[49] Sabya Sachi Chatterjee et al. “Constraining nonstandard interactions with coherent elastic neutrino-nucleus scattering at the European Spallation Source”. In: *Phys. Rev. D* 107 (5 2023), p. 055019. DOI: `10.1103/PhysRevD.107.055019` (cit. on p. 15).

[50] P. S. Barbeau, Yu. Efremenko, and K. Scholberg. *COHERENT at the Spallation Neutron Source*. 2021 (cit. on pp. 16, 17).

[51] Daniel Z. Freedman. “Coherent effects of a weak neutral current”. In: *Phys. Rev. D* 9 (5 1974), pp. 1389–1392. DOI: `10.1103/PhysRevD.9.1389` (cit. on p. 16).

[52] S. J. Brice et al. “A method for measuring coherent elastic neutrino-nucleus scattering at a far off-axis high-energy neutrino beam target”. In: *Physical Review D* 89.7 (Apr. 2014). ISSN: 1550-2368. DOI: `10.1103/physrevd.89.072004` (cit. on p. 17).

[53] Gianfranco Bertone and Dan Hooper. “History of dark matter”. In: *Rev. Mod. Phys.* 90 (4 2018), p. 045002. DOI: `10.1103/RevModPhys.90.045002` (cit. on p. 17).

[54] Marco Battaglieri et al. “US Cosmic Visions: New Ideas in Dark Matter 2017: Community Report”. In: *U.S. Cosmic Visions: New Ideas in Dark Matter*. July 2017. DOI: `https://doi.org/10.48550/arXiv.1707.04591` (cit. on p. 17).

[55] Gordan Krnjaic. “Probing Light Thermal Dark-Matter With a Higgs Portal Mediator”. In: *Phys. Rev. D* 94.7 (2016), p. 073009. DOI: `10.1103/PhysRevD.94.073009` (cit. on p. 17).

[56] Marco Fabbrichesi, Emidio Gabrielli, and Gaia Lanfranchi. *The Physics of the Dark Photon - A Primer*. Springer International Publishing, 2020. ISBN: 978-3-030-62518-4 (cit. on p. 17).

[57] Alessandra Filippi and Marzio De Napoli. “Searching in the dark: the hunt for the dark photon”. In: (2020). DOI: `https://doi.org/10.1016/j.revip.2020.100042` (cit. on p. 17).

[58] C. Antel et al. “Feebly Interacting Particles: FIPs 2022 workshop report”. In: *Eur. Phys. J. C* 83 (2023), p. 1122. DOI: `10.1140/epjc/s10052-023-12168-5` (cit. on p. 18).

[59] C. Patrignani. “Review of Particle Physics”. In: *Chinese Physics C* 40.10 (2016), p. 100001. DOI: `10.1088/1674-1137/40/10/100001` (cit. on p. 18).

[60] Chien-Yi Chen, Maxim Pospelov, and Yi-Ming Zhong. "Muon Beam Experiments to Probe the Dark Sector". In: *Phys. Rev. D* 95.11 (2017), p. 115005. DOI: 10.1103/PhysRevD.95.115005 (cit. on pp. 18, 40, 41).

[61] L. Marsicano et al. "Probing Leptophilic Dark Sectors at Electron Beam-Dump Facilities". In: *Phys. Rev. D* 98.11 (2018), p. 115022. DOI: 10.1103/PhysRevD.98.115022 (cit. on pp. 18, 40, 64).

[62] Alireza Haghighat. *Monte Carlo Methods for Particle Transport*. July 2020. ISBN: 9780429198397. DOI: 10.1201/9780429198397 (cit. on p. 19).

[63] John Hey, Tibor Neugebauer, and Carmen Pasca. "Georges-Louis Leclerc de Buffon's 'Essays on Moral Arithmetic'". In: Aug. 2010, pp. 245–282. ISBN: 978-3-642-13982-6. DOI: 10.1007/978-3-642-13983-3_15 (cit. on p. 19).

[64] FLUKA.CERN. *Introduction to the Monte Carlo simulation of radiation transport*. University Lecture. 2022 (cit. on p. 20).

[65] Los Alamos National Laboratory. *MCNP Website*. 2024. URL: https://mcnp.lanl.gov/ (visited on 06/05/2024) (cit. on p. 22).

[66] Joel Aaron Kulesza et al. *MCNP® Code Version 6.3.0 Theory & User Manual*. Tech. rep. LA-UR-22-30006, Rev. 1. Los Alamos, NM, USA: Los Alamos National Laboratory, 2022. DOI: 10.2172/1889957 (cit. on p. 22).

[67] Japan Atomic Energy Agency. *PHITS Website*. 2007. URL: https://phits.jaea.go.jp/ (visited on 06/05/2024) (cit. on p. 22).

[68] Tatsuhiko Sato et al. "Recent improvements of the particle and heavy ion transport code system – PHITS version 3.33". In: *Journal of Nuclear Science and Technology* 61.1 (2024), pp. 127–135. DOI: 10.1080/00223131.2023.2275736 (cit. on p. 22).

[69] Tatsuhiko Sato et al. "Overview of particle and heavy ion transport code system PHITS". In: *Annals of Nuclear Energy* 82 (2015). Joint International Conference on Supercomputing in Nuclear Applications and Monte Carlo 2013, SNA + MC 2013. Pluri- and Trans-disciplinarity, Towards New Modeling and Numerical Simulation Paradigms, pp. 110–115. ISSN: 0306-4549. DOI: https://doi.org/10.1016/j.anucene.2014.08.023 (cit. on p. 22).

[70] I Kawrakow et al. *EGSnrc toolkit for Monte Carlo simulation of ionizing radiation transport*. doi:10.4224/40001303 [release v2023]. 2000 (cit. on p. 22).

[71] CERN. *FLUKA CERN Website*. URL: https://fluka.cern/ (visited on 06/06/2024) (cit. on p. 23).

[72] C. Ahdida et al. "New Capabilities of the FLUKA Multi-Purpose Code". In: *Frontiers in Physics* 9 (2022). ISSN: 2296-424X. DOI: 10.3389/fphy.2021.788253 (cit. on p. 23).

[73] Giuseppe Battistoni et al. "Overview of the FLUKA code". In: *Annals of Nuclear Energy* 82 (2015). Joint International Conference on Supercomputing in Nuclear Applications and Monte Carlo 2013, SNA + MC 2013. Pluri- and Trans-disciplinarity, Towards New Modeling and Numerical Simulation Paradigms, pp. 10–18. ISSN: 0306-4549. DOI: `https://doi.org/10.1016/j.anucene.2014.11.007` (cit. on p. 23).

[74] Vasilis Vlachoudis. "FLAIR: A POWERFUL BUT USER FRIENDLY GRAPHICAL INTERFACE FOR FLUKA". In: Apr. 2009 (cit. on p. 24).

[75] Guido Van Rossum and Fred L. Drake. *Python 3 Reference Manual*. Scotts Valley, CA: CreateSpace, 2009. ISBN: 1441412697 (cit. on p. 24).

[76] Thomas Williams, Colin Kelley, and many others. *Gnuplot 4.6: an interactive plotting program*. `http://gnuplot.sourceforge.net/`. 2013 (cit. on p. 24).

[77] CERN. *FLUKA CERN Manual*. URL: `https://flukafiles.web.cern.ch/manual/index.html` (visited on 06/06/2024) (cit. on p. 25).

[78] *ROOT File (ROOT CERN)*. URL: `https://root.cern/manual/root_files/` (visited on 06/10/2024) (cit. on p. 29).

[79] *TChain Class - ROOT File (ROOT CERN)*. URL: `https://root.cern.ch/doc/master/classTChain.html` (visited on 06/11/2024) (cit. on p. 29).

[80] *USRINI (FLUKA User routine)*. URL: `https://flukafiles.web.cern.ch/manual/chapters/user_routines/user_routines/usrini.html` (visited on 07/05/2024) (cit. on p. 29).

[81] *USROUT (FLUKA User routine)*. URL: `https://flukafiles.web.cern.ch/manual/chapters/user_routines/user_routines/usrout.html` (visited on 07/05/2024) (cit. on p. 29).

[82] *TTree Class - ROOT File (ROOT CERN)*. URL: `https://root.cern.ch/doc/master/classTTree.html` (visited on 06/11/2024) (cit. on p. 29).

[83] *MGDRAW (FLUKA User routine)*. URL: `https://flukafiles.web.cern.ch/manual/chapters/user_routines/user_routines/mgdraw.html` (visited on 06/10/2024) (cit. on p. 29).

[84] *SOURCE_NEWGEN (FLUKA User routine)*. URL: `https://flukafiles.web.cern.ch/manual/chapters/user_routines/user_routines/source_newgen.html` (visited on 07/05/2024) (cit. on p. 29).

[85] *MAGFLD (FLUKA User routine)*. URL: `https://flukafiles.web.cern.ch/manual/chapters/user_routines/user_routines/magfld.html` (visited on 07/05/2024) (cit. on p. 29).

[86] *USIMBS (FLUKA User routine)*. URL: https://flukafiles.web.cern.ch/manual/chapters/user_routines/user_routines/usimbs.html (visited on 07/05/2024) (cit. on p. 29).

[87] LLC Jefferson Science Associates. *JLAB Website*. URL: https://www.jlab.org/ (visited on 06/06/2024) (cit. on p. 31).

[88] J. Arrington et al. “Physics with CEBAF at 12 GeV and future opportunities”. In: *Progress in Particle and Nuclear Physics* 127 (2022), p. 103985. ISSN: 0146-6410. DOI: https://doi.org/10.1016/j.ppnp.2022.103985 (cit. on p. 32).

[89] A. Accardi et al. *Strong Interaction Physics at the Luminosity Frontier with 22 GeV Electrons at Jefferson Lab*. 2023. DOI: https://doi.org/10.48550/arXiv.2306.09360 (cit. on p. 32).

[90] A. Accardi et al. *Strong Interaction Physics at the Luminosity Frontier with 22 GeV Electrons at Jefferson Lab*. 2023 (cit. on p. 34).

[91] J. Alcorn et al. “Basic instrumentation for Hall A at Jefferson Lab”. In: *Nuclear Instruments and Methods in Physics Research Section A: Accelerators, Spectrometers, Detectors and Associated Equipment* 522.3 (2004), pp. 294–346. ISSN: 0168-9002. DOI: https://doi.org/10.1016/j.nima.2003.11.415 (cit. on p. 35).

[92] M. Battaglieri et al. *Dark matter search in a Beam-Dump eXperiment (BDX) at Jefferson Lab*. 2016. URL: https://ui.adsabs.harvard.edu/abs/2016arXiv160701390B (cit. on pp. 36, 61).

[93] Luca Marsicano. *The Beam-Dump eXperiment*. Mar. 2021. URL: http://hdl.handle.net/11567/1001409 (cit. on p. 36).

[94] M. Kharashvili. *JLAB-TN-16-048*. Tech. rep. 2016 (cit. on p. 38).

[95] *FLUKA CERN Manual - DEFAULTS*. URL: https://flukafiles.web.cern.ch/manual/chapters/description_input/description_options/defaults.html (visited on 06/21/2024) (cit. on p. 38).

[96] *FLUKA CERN Manual - PART-THRes*. URL: https://flukafiles.web.cern.ch/manual/chapters/description_input/description_options/part-thr.html (visited on 06/21/2024) (cit. on p. 39).

[97] M. Ungaro et al. “The CLAS12 Geant4 simulation”. In: *NIM A* 959 (2020), p. 163422. ISSN: 0168-9002. DOI: https://doi.org/10.1016/j.nima.2020.163422 (cit. on p. 40).

[98] M. Battaglieri et al. *Dark matter search in a Beam-Dump eXperiment (BDX) at Jefferson Lab – 2018 update to PR12-16-001*. 2019. DOI: https://doi.org/10.48550/arXiv.1712.01518 (cit. on pp. 40, 53, 64).

[99] *The LUND format - GEMC*. URL: https://gemc.jlab.org/gemc/html/documentation/generator/lund.html (visited on 09/11/2024) (cit. on p. 40).

[100] S. Adhikari et al. “The GlueX beamline and detector”. In: *Nuclear Instruments and Methods in Physics Research Section A: Accelerators, Spectrometers, Detectors and Associated Equipment* 987 (2021), p. 164807. ISSN: 0168-9002. DOI: https://doi.org/10.1016/j.nima.2020.164807 (cit. on p. 42).

[101] D. Day et al. “A conceptual design study of a Compact Photon Source (CPS) for Jefferson Lab”. In: *Nuclear Instruments and Methods in Physics Research Section A: Accelerators, Spectrometers, Detectors and Associated Equipment* 957 (2020), p. 163429. ISSN: 0168-9002. DOI: https://doi.org/10.1016/j.nima.2020.163429 (cit. on pp. 43, 83).

[102] Igor Strakovsky et al. *Conceptual Design of Beryllium Target for the KLF Project*. 2020 (cit. on p. 43).

[103] Chapelain, Antoine. “The Muon g-2 experiment at Fermilab”. In: *EPJ Web Conf.* 137 (2017), p. 08001. DOI: 10.1051/epjconf/201713708001 (cit. on p. 51).

[104] M. Battaglieri et al. “The BDX-MINI detector for Light Dark Matter search at JLab”. In: *Eur. Phys. J. C* 81.2 (2021), p. 164. DOI: 10.1140/epjc/s10052-021-08957-5 (cit. on pp. 61, 63, 64).

[105] D. Akimov and et al. “Simulating the neutrino flux from the Spallation Neutron Source for the COHERENT experiment”. In: *Phys. Rev. D* 106 (3 2022), p. 032003. DOI: 10.1103/PhysRevD.106.032003 (cit. on p. 67).

[106] D. Aristizabal Sierra et al. “Coherent elastic neutrino-nucleus scattering with the nuDRIFT directional detector at next generation neutrino facilities”. In: *Physical Review D* 104.3 (Aug. 2021). ISSN: 2470-0029. DOI: 10.1103/physrevd.104.033004 (cit. on pp. 68, 79).

[107] Francisco J. Bermejo and Fernando Sordo. “Chapter 2 - Neutron Sources”. In: *Neutron Scattering – Fundamentals*. Ed. by Felix Fernandez-Alonso and David L. Price. Vol. 44. Experimental Methods in the Physical Sciences. Academic Press, 2013, pp. 137–243. DOI: https://doi.org/10.1016/B978-0-12-398374-9.00002-4 (cit. on p. 68).

[108] George Papamakarios et al. *Normalizing Flows for Probabilistic Modeling and Inference*. 2021 (cit. on p. 71).

[109] Ivan Kobyzev, Simon J.D. Prince, and Marcus A. Brubaker. “Normalizing Flows: An Introduction and Review of Current Methods”. In: *IEEE Transactions on Pattern Analysis and Machine Intelligence* 43.11 (Nov. 2021), pp. 3964–3979. ISSN: 1939-3539. DOI: 10.1109/tpami.2020.2992934 (cit. on p. 71).

[110] A. Devred et al. “Proof-of-Principle of an Energy-Efficient, Iron-Dominated Electromagnet for Physics Experiments”. In: *IEEE Transactions on Applied Superconductivity* PP (Aug. 2024), pp. 1–7. DOI: `10.1109/TASC.2024.3355872` (cit. on p. 89).

[111] Johannes Bernhard et al. “Studies for new experiments at the CERN M2 beamline within “physics beyond colliders”: AMBER/COMPASS++, NA64μ, MuonE”. In: *AIP Conf. Proc.* 2249.1 (2020). Ed. by Curtis Meye and Reinhard A. Schumacher, p. 030035. DOI: `10.1063/5.0008957` (cit. on p. 92).

[112] Tobias Junginger et al. “SRF material research using muon spin rotation and beta-detected nuclear magnetic resonance”. In: *Frontiers in Electronic Materials* 4 (2024). ISSN: 2673-9895. DOI: `10.3389/femat.2024.1346235` (cit. on p. 92).

[113] L. Bartoszek et al. *Mu2e Technical Design Report*. 2015 (cit. on p. 92).